SPECTROSCOPIC INVESTIGATION OF A NOVEL TRAUMATIC BRAIN INJURY BIOMARKER AND ANALYSIS OF NEUROMETABOLIC CHANGES IN YOUTH AMERICAN FOOTBALL ATHLETES

A Dissertation

Submitted to the Faculty

of

Purdue University

by

Nicole L. Vike

In Partial Fulfillment of the

Requirements for the Degree

of

Doctor of Philosophy

August 2019

Purdue University

West Lafayette, Indiana

THE PURDUE UNIVERSITY GRADUATE SCHOOL
STATEMENT OF DISSERTATION APPROVAL

Dr. Thomas Talavage, Co-Chair

School of Electrical and Computer Engineering, Weldon School of Biomedical Engineering

Dr. Riyi Shi, Co-Chair

School of Veterinary Medicine, Weldon School of Biomedical Engineering

Dr. Joseph Rispoli

Weldon School of Biomedical Engineering, School of Electrical and Computer Engineering

Dr. Eric Nauman

School of Veterinary Medicine, School of Mechanical Engineering

Approved by:

Dr. Laurie Jaeger

Head of the Graduate Program

I would first like to dedicate this dissertation to my amazing friends (Kevin Mitchell Jr., Cynthia Alvarado, Katherine Wehde, Stefan Irby, Liesl Krause, Stephen Miloro, Alexa Clarisse, Erim Demirel, Melanie Venderley, MacKenzie Tweardy, Goutham Sankaran, Sonia Petty, Jennifer Frisinger, Hannah Miller, Meghan Phillips, Christine Doyle, Rachel Peterson, Joshua Hunter, and David Vo) and family (Kari and Marc Vike, Kevin and Debra Mitchell, Brittney Mitchell, The Gestelands, and The Johnsons) - I could not have accomplished what I have without their unconditional love and support.

A special dedication to Robert Gesteland (1930-2018), my great uncle and a true inspiration in the field of neuroscience.

I also dedicate this work to my devoted colleagues (Sumra Bari, Pratik Kashyap, Ikbeom Jang, Taylor Lee, Xin Li, Xianglun Mao, and Yukai Zou). Without their assistance and commitment, this work would not be possible.

ACKNOWLEDGMENTS

First, I would like to acknowledge my committee members for their exceptional guidance and expertise throughout the duration of my PhD. I would also like to acknowledge Dr. Gregory Tamer Jr. for his assistance with both 3T and 7T MRI imaging. Thirdly, I acknowledge the Purdue NMR Facility, specifically Dr. John Harwood and Dr. Huaping Mo, for their expertise in NMR experimentation. I would also like to acknowledge Kelsey Hopkins, Dr. Luis Solorio, and Jonathan Tang for their pivotal collaboration efforts on the DWI (Hopkins and Solorio) and acrolein projects (Tang). Lastly, I acknowledge my colleagues whose inputs were instrumental in experimental design, processing, and/or reporting (Sumra Bari, Taylor Lee, Yukai Zou, Xin Li).

TABLE OF CONTENTS

Page

Page

Page

LIST OF TABLES

Table Page

LIST OF FIGURES

Figure Page

Figure Page

Figure Page

Figure Page

SYMBOLS

B_0 static magnetic field

ω Larmor frequency

T Tesla

mm millimeter

ms millisecond

kHz kiloHertz

MHz megaHertz

1^H proton

13^C carbon-13

M molar

mM millimolar

w/v weight per volume

ABSTRACT

Vike, Nicole L. Ph.D., Purdue University, August 2019. Spectroscopic Investigation of a Novel Traumatic Brain Injury Biomarker and Analysis of Neurometabolic Changes in Youth American Football Athletes. Major Professor: Thomas M. Talavage.

Recent advances in Magnetic Resonance Imaging (MRI), a noninvasive imaging technique, have spurred the exploration of poorly understood physiological phenomena *in vivo*. Applications of MRI vary greatly, from anatomical evaluation to complex functional analysis. The body of this dissertation presents four applications of MRI: 1) investigation of a novel traumatic brain injury (TBI) biomarker, 2) analysis of position-specific head acceleration events on neurometabolic profiles in high school football athletes, 3) the first reporting of neurometabolic changes in middle school football athletes, and 4) a novel application of diffusion-weighted imaging (DWI) to characterize implantable drug-delivery depots (Appendix A).

Magnetic resonance spectroscopy (MRS) is an MRI method used to evaluate the metabolic profiles of tissues. Certain brain metabolites (N-acetyl aspartate, *myo*-inositol, choline, creatine, and glutamate/glutamine) offer unique information regarding brain homeostasis following TBI. When coupled with additional metrics, such as head acceleration events recorded during collision-sport participation, the mechanisms of neurophysiological changes can be further elucidated. Here, player position-specific neurometabolic changes were evaluated in high school and middle school football athletes. Striking differences were noted between linemen and non-linemen as well as high school and middle school athletes.

However, in most clinical cases of TBI, information regarding head acceleration events is unknown and baseline scans are not available. Therefore, it is critical to evaluate candidate biomarkers which increase solely in response to injury. Acrolein,

a toxic reactive oxygen species, has been shown to increase following injury to the central nervous system in animal models. Hence, acrolein is a prime TBI biomarker candidate and has been investigated using nuclear magnetic resonance and MRS at 7 Tesla.

Applications of MRI are not limited to the brain, or even tissues. Studies have reported that up to 50% of patients fail to take their medications correctly - resulting in disease progression and medication waste. *In situ* forming implants (ISFIs) offer an alternative to oral dosage regimens but have not been validated *in vivo*. Using DWI, ISFIs can be characterized noninvasively and their design can be refined, ultimately improving patient outcomes.

Taken together, MRI is powerful tool that can be used to investigate a wide range of physiological questions. Chapters 2-4 will emphasize efforts to improve TBI diagnostics and better understand neurometabolic changes in youth football athletes. Appendix A offers insights into the DWI-guided characterization of *in situ* forming implants.

1. INTRODUCTION

Magnetic Resonance Imaging (MRI) is a safe and noninvasive medical diagnostic tool with vast applications in scientific research. MRI methods can range from anatomical investigation to complex analysis of white matter tracts in the brain. The most common MRI research methodologies include diffusion-tensor and diffusion-weighted imaging (DWI), functional and resting-state imaging, perfusion imaging, magnetic resonance spectroscopy (MRS), and T_1 and T_2 anatomical imaging. These methods can be applied to investigate various diseases and injuries, such as epilepsy, Alzheimer's disease, breast cancer, knee fractures, and traumatic brain injuries (TBIs). After complex analysis, each method can provide unique structural or functional information regarding the anatomy of interest (e.g. white matter integrity or brain activity, respectively).

The presented work focuses on novel applications of MRS and DWI. Magnetic resonance spectroscopy can be applied to study the metabolic profiles of tissues. For example, changes in brain metabolic profiles can be analyzed over a season of American football to study the potential effects of contact sport participation on neurometabolic homeostasis in youth athletes. Additionally, MRS can be used to investigate novel biomarkers of TBI, such as acrolein, which have potential to improve TBI diagnosis, rehabilitation effectiveness, and recovery. Diffusion-weighted imaging is useful for quantifying the directionality of water diffusion in a region(s) of interest. For example, DWI can be used to noninvasively assess the temporal diffusivity of *in situ* forming implants (ISFIs) - small injectable drug delivery depots. Proper analysis of diffusivity can lead to improved ISFI design, and ultimately enhanced treatment efficacy. In the remaining introductory chapter, the aforementioned MRI methods, MRS and DWI, will be discussed in detail. Introductions to acrolein, sports-related

TBI (in high school and middle school football athletes), and ISFIs will be detailed in their corresponding sections.

1.1 MRI Basics and Magnetic Resonance Spectroscopy

Magnetic Resonance Spectroscopy (MRS) is a Magnetic Resonance Imaging (MRI) method used to obtain metabolic profiles of tissues noninvasively. The fundamental physics underlying the MRS methodology is related to Nuclear Magnetic Resonance (NMR), an analytical chemistry tool. The major difference between the two methods corresponds to the object of interest. MRS is most commonly used for *in vivo* body imaging, while NMR is used to investigate chemical solutions. Here, the basic physics underlying MRI and MRS will be discussed in detail.

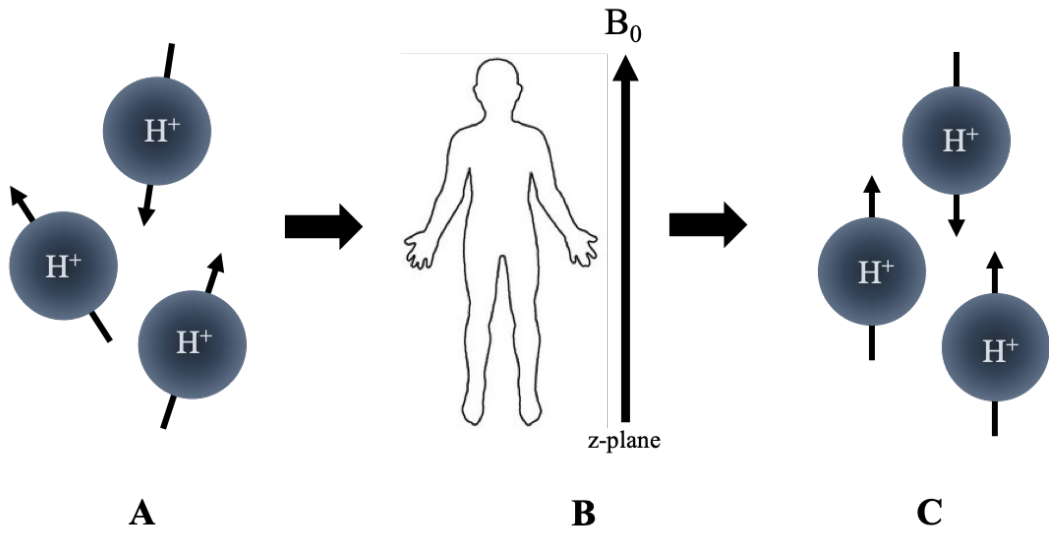

Fig. 1.1. Alignment of proton spins in the magnetic field, B_0. (A) Randomly oriented proton spins without an applied B_0. (B) The subject is placed in the uniform magnetic field. (C) Proton spins align and precess about the direction (z-plane) of the magnetic field (B_0) - either parallel or antiparallel.

1.1.1 Magnetization and Relaxation

First, it is important to understand the fundamental physics underlying MRI. MRI relies on a static magnetic field (B_0), a radiofrequency (RF) field (B_1), and a gradient system with gradients in three directions (G_x, G_y, and G_z). The object (or subject) of interest is placed in the bore of the MRI machine and the static magnetic field (B_0) forces proton spins to align in the direction of B_0 (Figure 1.1). In this orientation, the spins have a net magnetization of zero, represented by M_0. The spins precess about B_0 at a specific frequency, called the Larmor frequency, or ω [1]. Once the spins are uniformly aligned, an RF pulse is applied which tips the spins transverse to B_0. RF pulses are transmitted via RF coils which can both transmit and receive signal. The resulting net magnetization is now in the transverse plane, and is referred to as M_xy (Figure 1.2).

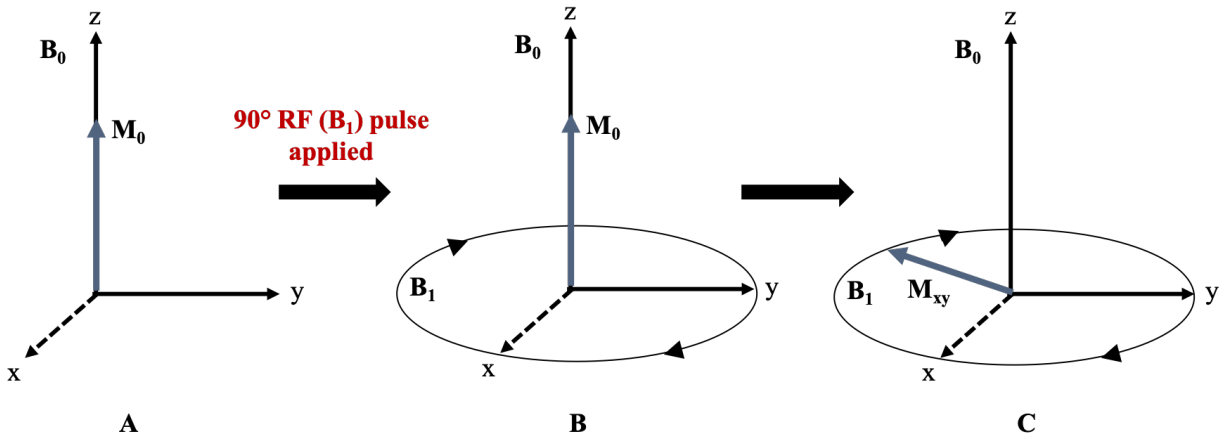

Fig. 1.2. Application of the RF pulse. (A) spins are aligned in the direction of B_0 and precess about the z-axis at the Larmor frequency (ω). The net magnetization = M_0 (B) A 90° RF pulse is applied in the xy-plane. (C) The spins tip 90° into the xy-plane and have a net magnetization of M_{xy}.

The spins precess about the xy-plane and eventually relax back to the z-plane in a process called relaxation. The frequency of this event is received by a receive coil

and is referred to as the spin echo, or echo for short (this becomes important in the design of pulse sequences, Section 1.1.4). Two types of relaxation occur: transverse (T_2) and longitudinal (T_1) [2, 3]. Transverse relaxation (T_2) refers to spins which dephase in the xy-plane, perpendicular to B_0 (Figure 1.3B). As the spins continue to dephase in the xy-plane, M_{xy} will eventually equal zero. Longitudinal relaxation (T_1) refers to spins which recover to the z-plane, or the plane parallel to B_0 (Figure 1.3A). As the spins undergo T_1 relaxation, M_z will eventually equal M_0. T_1 and T_2 can be expressed in equation form (Equations 1.1 and 1.2, respectively) [2, 4].

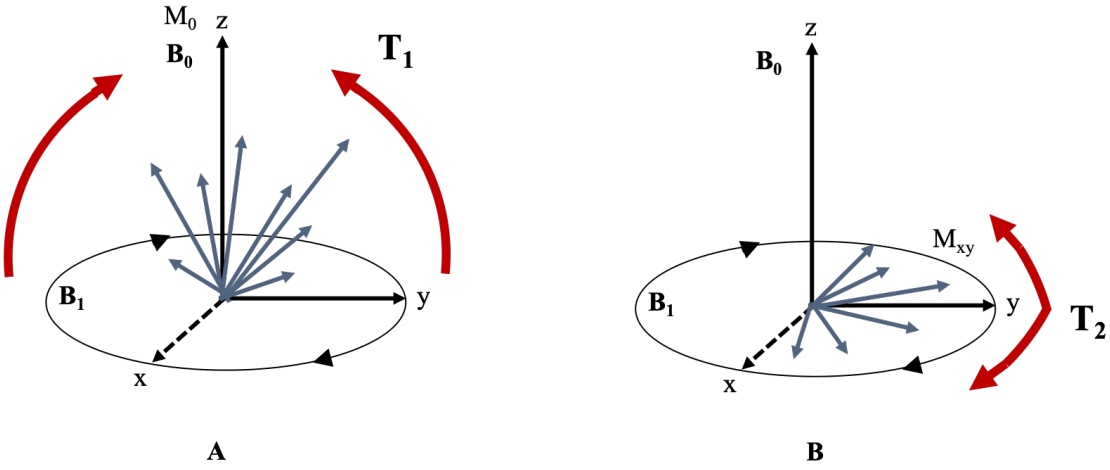

Fig. 1.3. A visual representation of T_1 and T_2 relaxation. (A) T_1 relaxation is defined by the recovery of spins from the xy-plane to the z-plane following a 90° RF pulse; overtime, $M_z = M_0$ (B) T_2 relaxation is defined by the dephasing of spins in the xy-plane where eventually, $M_{xy} = 0$.

$$M_z = M_0(1 - e^{-t/T_1}) \tag{1.1}$$

$$M_{xy} = M_0(e^{-t/T_2}) \tag{1.2}$$

1.1.2 Chemical Shift

In spectroscopic imaging, the precession of spins is extremely important and is referred to as resonance. Not all proton nuclei resonate at the same frequency. In fact, precession depends on the local magnetic field experienced by a given nucleus at the atomic level; this depends on the environment in which the nucleus exists [5, 6]. Specifically, resonance frequency changes because the electron cloud of each nuclei induces a magnetic field on the proton which opposes the direction of B_0. This effect is slightly different for each nuclei resulting in different rates of precession [5]. The difference in nuclear precession, or resonant frequencies, is called chemical shift which ultimately dictates the location of peaks on a spectrum. Chemical shift is typically measured in units of parts-per-million (ppm) [4]. Spectral quantification will be discussed further in subsection 1.1.6.

1.1.3 Gradients

Gradient coils (G_x, G_y, and G_z) are used for spatial localization [7, 8]. These coils emit a B-field that is weaker than B_0, but which exists along a gradient of RF strengths. That is, every position in the body experiences a slightly different gradient field along the x, y, and z planes. Using this feature, it is possible to localize a specific region of interest [7]. G_z is used to select a specific slice of interest along the z-axis, therefore termed slice selection [4]. G_x is applied to give a specific location along the x-axis, also referred to as the frequency encoding direction. Finally, the G_y gradient is applied to select a region along the y-axis, also called the phase encoding direction. Figure 1.4 displays the directions of the gradients in each plane. Radiofrequency and gradient pulses can be applied at different times and in different combinations to obtain the information from a desired region of interest. The result of these combinations is called a pulse sequence [9]. There are two terms which are critical for designing a pulse sequence: echo time (TE) and relaxation time (TR) [10]. TE refers to the time from the center of the first RF pulse and the middle of the echo (recall

from the discussion of relaxation times). TR refers to the total length of a repeated pulse sequence.

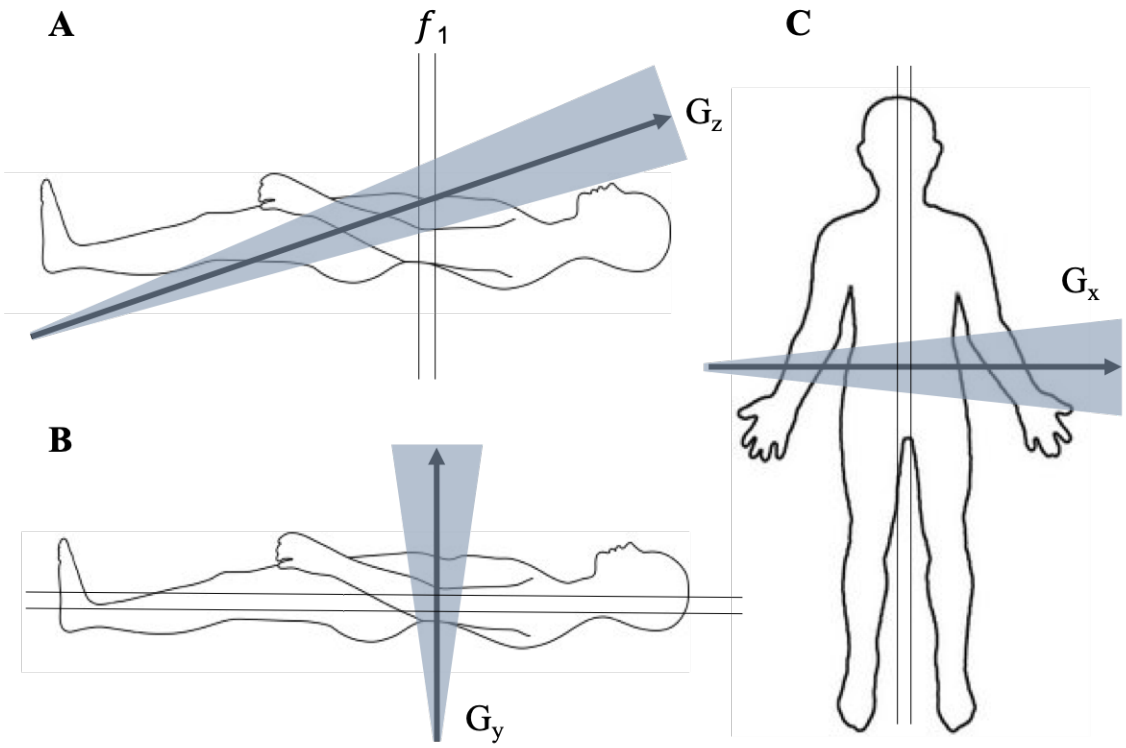

Fig. 1.4. Spatial localization with gradient coils. (A) Slice selection in the z-plane. (B) Frequency encoding in the x-plane. (C) Phase encoding in the y-plane.

1.1.4 MRS Pulse Sequence

Pulse sequences can be engineered in many ways but here, the focus is MRS pulse sequence design. MRS differs slightly from normal MRI methodologies since the information of interest is chemical, not spatial or anatomical. Because of this, the spin echo is sampled without the gradient readout as to obtain frequency information, not spatial information [11]. The most commonly used MRS pulse sequence for 1.5 T and 3.0 T ^{1}H MRI systems is Point RESOlved Spectroscopy (PRESS) [12, 13]. This method uses three slice-selective RF gradient pulses (90°-180°-180°) to localize a 3D

geometry, or voxel (Figure 1.5). The 90°-180°-180° schema refers to the sequence of degrees to which the RF pulses tip the spins (i.e. a 90° pulse would tip spins from the z-plane to the transverse, xy-plane). The echo of interest is the last echo (PRESS echo), which contains signal from the localized voxel of interest. Following signal acquisition, the echo must be transformed from the time domain to the frequency domain in a process called Fourier Transformation (FT) [14].

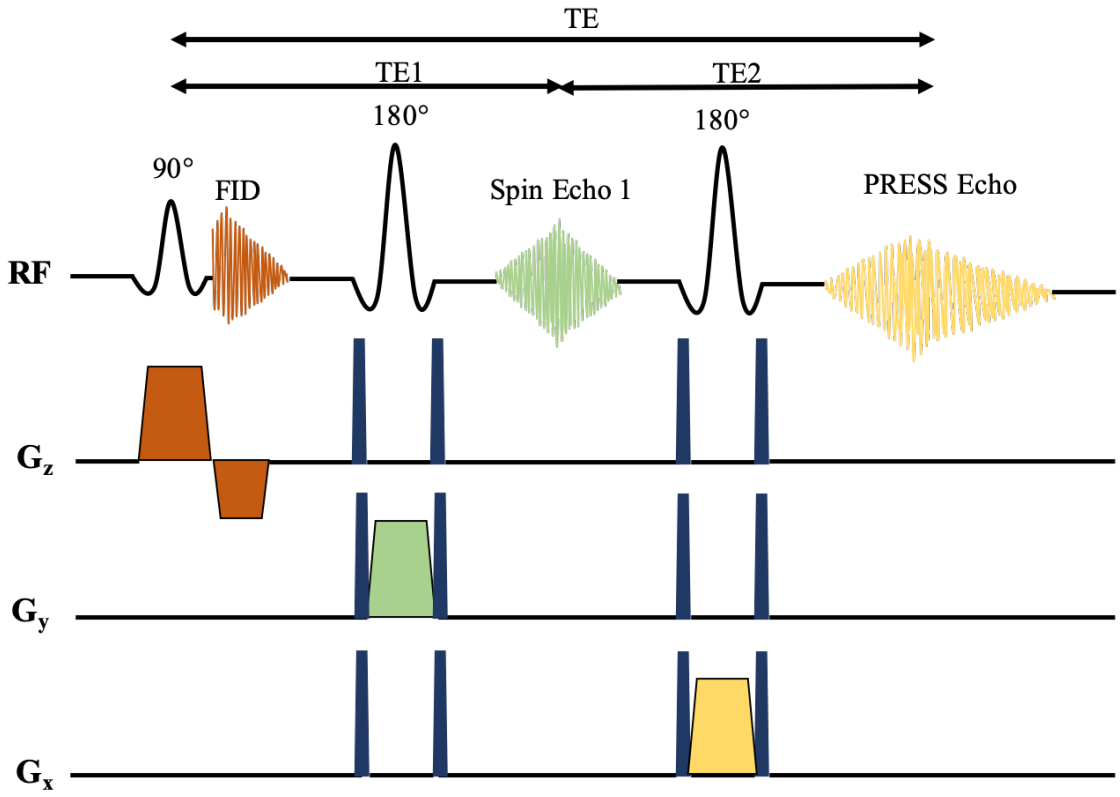

Fig. 1.5. PRESS pulse sequence. First a 90° RF pulse is applied in the z-direction, followed by a short refocusing pulse. The dark blue pulses are referred to as crusher gradients which are required to remove spurious signals coming from the regions outside the 3D region of interest. Next, a 180° RF pulse is applied using the G_y. Finally, a second 180° pulse is applied in the x-direction. The combination of pulses in all three directions results in a 3D volume, or voxel, at a specific region of interest.

1.1.5 Fourier Transformation

This process is necessary for the analysis of spectroscopic data. The equation for FT is show in equation 1.3 where S(ω) represents the Fourier transformed frequency domain, s(t) is the signal from the time domain, and the complex $e^{-i\omega t}$ includes information on the frequency, amplitude, and phase of the signal in the time domain [4, 15]. A graphical representation of FT is shown in Figure 1.6. The next step in spectroscopic imaging is data processing and spectral analysis.

$$S(\omega) = \int_{-\infty}^{\infty} s(t)e^{-i\omega t}dt \tag{1.3}$$

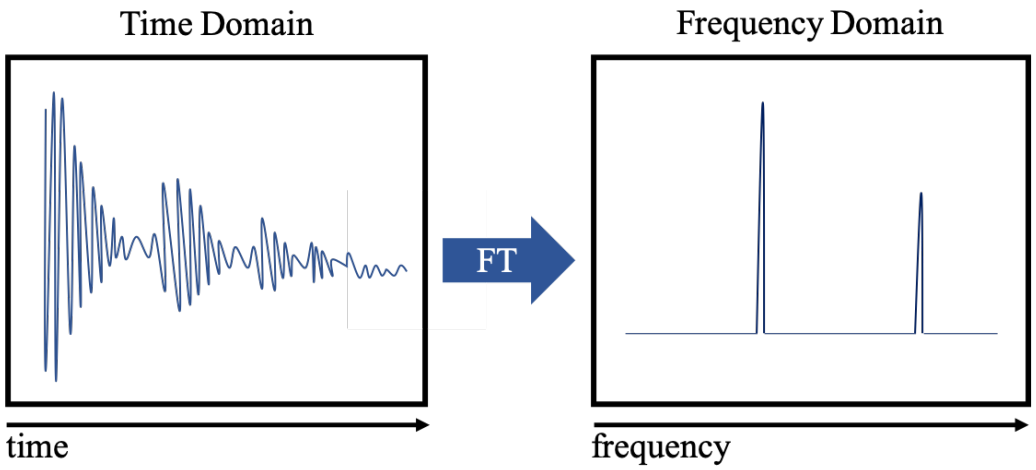

Fig. 1.6. A typical Fourier transformation from the time domain s(t) to the frequency domain S(ω).

1.1.6 Spectral Analysis and Metabolite Quantification

After the data have been transformed, the peaks can be integrated and quantified. This is typically performed by taking the area under each peak of interest. However, the area under the peak does *not* represent the absolute concentration of the chemical/metabolite of interest. Instead, it is an indirect measure that can be affected

by many factors including chemical T_1 and T_2, B_0 and B_1 field inhomogeneities, and varying TE and TR [16]. To date, no methods exist to determine the true concentration of a chemical species using MRS. However, approaches do exist to provide relative concentrations using external or internal references. One example is the use of basis sets which provides prior knowledge of tissue-specific metabolic concentrations; this improves the accuracy of spectral fitting [17]. A second approach is to use an internal reference, such as water, or another stable metabolite, such as creatine [17–20]. In this way, the relative concentration of the peak of interest can be quantified in relation to a known tissue concentration. Additionally, more novel quantitative approaches have been proposed which account for the T_1 and T_2 of both the metabolite of interest and water, as well as the TR, TE, number of protons, and, in the case of brain tissue, the percentage of grey matter, white matter, and cerebrospinal fluid [21, 22].

1.1.7 Localizing and Shimming the Region of Interest

MRS is a powerful tool which can be used to noninvasively investigate the metabolic profile in a tissue of interest. However, complexities exist to achieve an adequate signal-to-noise ratio (SNR) and proper steps must be taken when acquiring data. First, it is critical to center the tissue (or object) of interest both in the coil and the bore of the magnet. This ensures that signal will be obtained from the region of interest (ROI), and not outside regions. After this step, a localizer sequence is run to orient the user to the anatomy. The resulting image can be used to improve the centering of the ROI before continuing the scanning protocol. To achieve better anatomical resolution, a multislice localizer sequence can be completed. This process is similar to the standard localizer sequence, but more image slices are obtained. This provides the user with higher resolution images of the anatomy of interest, ensuring proper voxel placement. Next, it is critical to conduct shimming on the region of interest. Shimming is a process by which B_0 is made more homogeneous in the ROI via small gradient adjustments [23, 24]. A homogeneous B_0 helps to eliminate noise in the

baseline of the spectrum, thereby improving SNR. Prior to PRESS, a localized shim protocol is completed for the region of interest. To conduct a shimming procedure, a voxel is placed in the ROI using images from the multislice localizer scan. Shimming should first be conducted on a volume larger than the ROI, followed by shimming on a volume the exact size of the ROI (typically between 3.0 mm^3 for animal brain scanning and 20 mm^3 for human brain scanning). The output of this protocol is a report of spectral line width (LW) - an indicator of good shimming procedure. The smaller the LW, the better the shim, and the better the resulting SNR. Typically, LWs less than eight are acceptable and LWs less that five are desired. An example of proper shim and ROI voxel placement can be seen in Fig. 1.7.

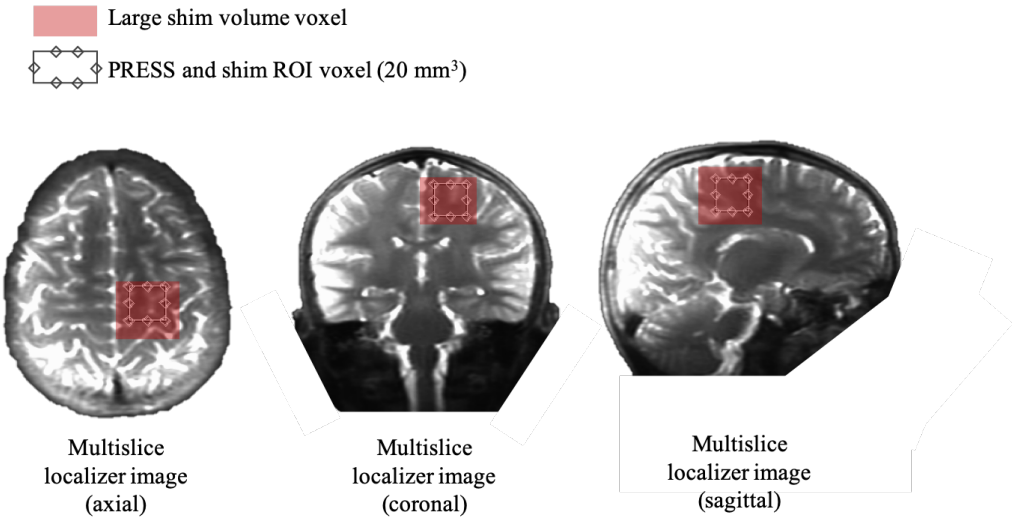

Fig. 1.7. Proper shim and PRESS voxel placement. The region in red corresponds to an example of a larger shim voxel placement. The region inside the red box corresponds to the ROI and indicates where the smaller shim voxel and PRESS voxel would be placed. The location and size of the smaller shim voxel and the PRESS voxel should be identical.

1.1.8 Water and Outer Volume Suppression

Additional methods can be applied to further improve SNR; these include water suppression, fat suppression, and outer volume suppression. The most abundant molecule in any biological specimen is water. In the human brain, water constitutes 73% of the tissue volume [25]. If water is not suppressed during MRS acquisition, there will be no other detectable peaks due to the fact that water exists at concentrations 10,000 times higher than other brain metabolites [26]. Therefore, a critical component of most MRS methods is adequate water suppression. Two commonly used water suppression methods exist: CHemical Shift Selective saturation (CHESS) and, a CHESS variant, VAriable Power radiofrequency pulses with Optimized Relaxation delays (VAPOR). These sequences are run prior to the MRS sequence and function by saturating the water signal with selective pulses tuned to the resonant frequency of water [27, 28] (Fig. 1.8).

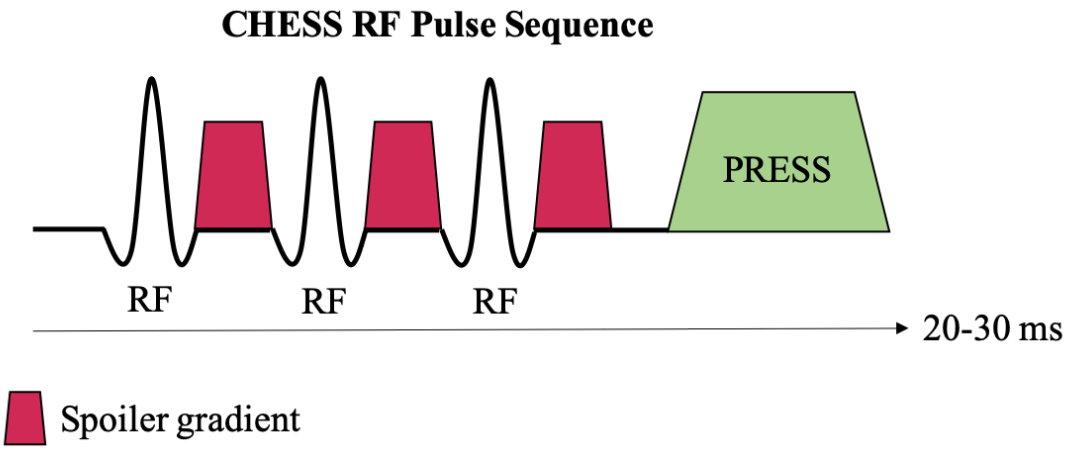

Fig. 1.8. A typical CHESS water suppression sequence run prior to the MRS sequence. CHESS consists of three water saturating pulses designed to minimize the water signal.

VAPOR is a specialized CHESS sequence which has been optimized with eight presaturation pulses, typically interleaved with outer volume suppression (OVS) [29]. Outer volume suppression, sometimes referred to as fat suppression, is commonly

used to suppress any and all signals from tissues surrounding the ROI [30, 31]. This prevents unwanted resonances, such fat, from bleeding into the spectrum and causing spectral broadening or distortion. For brain MRS, OVS bands are typically placed around the ROI. In the case of whole-brain imaging, this would look similar to what is depicted in Figure 1.9. For single-voxel MRS, OVS is not critical unless the ROI is near the skull. However, for Magnetic Resonance Spectroscopic Imaging (MRSI), a method for obtaining whole-brain spectra, OVS becomes critically important.

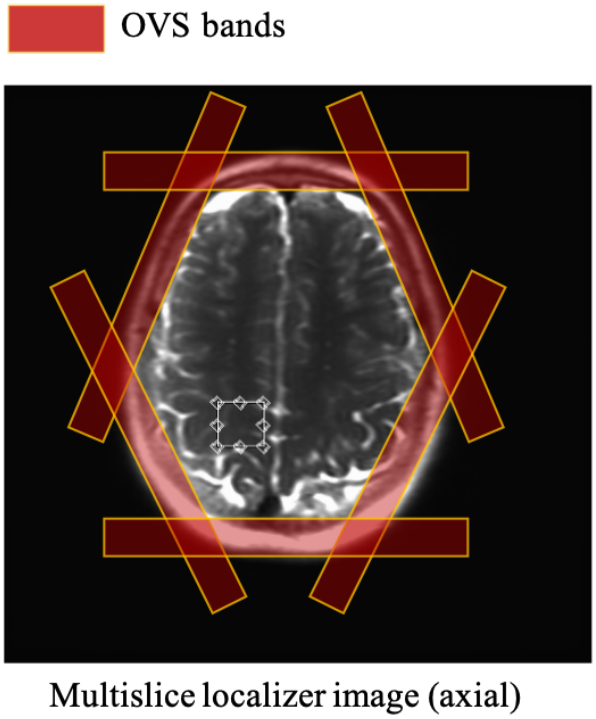

Fig. 1.9. An example of outer volume suppression band placement. Typically, OVS bands are placed outside the ROI at boundaries where fat could contaminate the signal.

1.1.9 MRS Applications

The noninvasive nature of MRI, combined with the quantitative metabolic profiling capabilities of MRS, provide a unique opportunity for novel research applications.

MRS has been applied in numerous fields of research, including psychiatry, oncology, and neuropathology, to answer critical questions. Levels of NAA were lower in patients with Schizophrenia which could indicate decreased neuronal density [32]. In studies of brain tumors, elevated levels of lactate and myo-inositol have been found which could be indicative of anaerobic glycolysis [33]. Traumatic brain injuries (TBIs) are increasingly common and can lead to significant long-term morbidity. Unfortunately, TBI is difficult to diagnose, treat, and prevent. Recent efforts have been made to 1) explore biomarkers of TBI and 2) understand the physiology of TBI. These efforts in these fields will be discussed more thoroughly in chapters 2-4.

1.2 Diffusion-Weighted Imaging

Another MRI method, diffusion-weighted imaging, uses the abundant signal from protons to determine the varying rate of Brownian water diffusion in a tissue of interest [34]. DWI is a considered a standard imaging technique and can provide tissue contrast. However, the data require significant post-processing. After image acquisition, apparent-diffusion coefficient (ADC) maps can be generated and the reported values from these maps can be analyzed (see section 1.2.2). DWI has diverse applications for studying different diseases and different tissues, such as breast cancer, brain development and injury, and musculoskeletal imaging [35]. In general, diffusion rates are observed to change in diseased or damaged tissues. When tissues are damaged, diffusion typically increases due to increased extracellular space and a corresponding increase in free water [34]. However, there are instances when diffusion decreases, including ischemia, malignancies, and infection [34]. While most studies use DWI and DTI to study tissue properties, these methods could also be applied for novel non-tissue applications. One such application relates to *in situ* forming implants (ISFIs) - small, biodegradable polymers designed to elute drug at a specific site and over a specific time [36, 37]. The application of DWI to study ISFIs *in vivo* will be

discussed further in chapter five. First, it is necessary to describe the methods of DWI acquisition and subsequent data analysis.

1.2.1 Diffusion-Weighted Imaging: Spin Echo Pulse Sequence

While many DWI pulse sequences exist, the classic spin echo (SE) sequence is considerably robust [38,39]. The DWI-SE sequence is marked by two diffusion-sensitizing gradients on either side of a 180° RF pulse (Figure 1.10). Proton spins that are non-mobile remain unaffected by the diffusion gradients and have no net change in phase [40]. However, mobile spins do experience a phase shift due to their displacement (Fig. 1.10). It should also be noted that while MRS is concerned only with the frequency output, DWI acquires spatial information. For this reason, the readout gradient is turned on during image acquisition.

1.2.2 DWI Analysis

As previously mentioned, spatial information is acquired for a given a ROI. In the case of DWI, this spatial information is related to the rate of water diffusion. The metric calculated from a DWI scan is referred to as the apparent diffusion coefficient (ADC) which is an average of the diffusion in all directions of the ROI [41]. To calculate ADC, two b-values (a measure of diffusion gradient strength; s/mm^2) must be used [42]. As the b-value increases, diffusion effects also increase. Typically, a b-value of 0 and 1000 s/mm^2 are used for brain imaging [35]. The relationship between b-value and signal intensity is given by equation 1.3 where S is the signal intensity, S_0 is the baseline signal intensity, b is the b-value, and D is the diffusion coefficient [42].

$$S = S_0 e^{-bD} \tag{1.4}$$

The two b-values are entered into the equation to solved for D. This is accomplished by taking the log of the signal intensity and plotting it as a linear function [35, 42]. The best fit of the linear regression is equal to D, which can then be

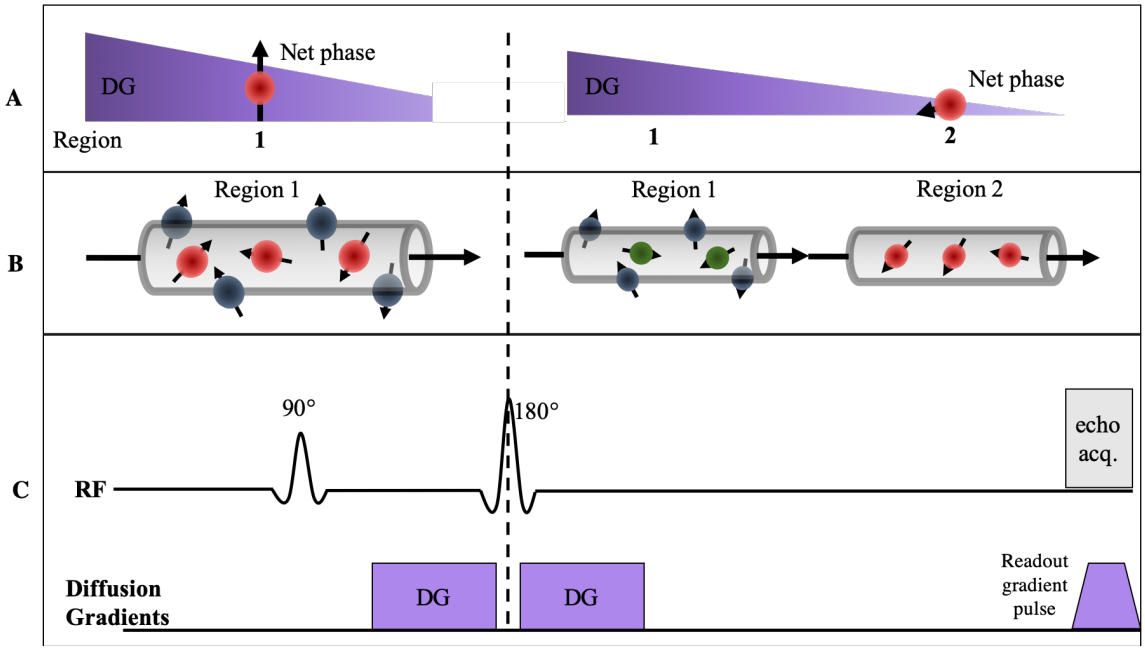

Fig. 1.10. Graphical representation of DWI signal acquisition. (A) DG represents the first and second diffusion gradients spatially. The net phase of the red spins is also depicted and labelled by region in space. (B) The blue spins are stationary and the red spins are mobile. In region 1, the red spins experience a gradient strength of a specific magnitude based on their location. The blue spins also experience the same gradient strength. After the second DG gradient is applied, the red spins have now moved to another location (region 2) and therefore experience a different gradient strength and have a different net phase than experienced in region 1. The blue spins remain stationary and therefore do not experience a change in gradient strength. (C) The pulse design of a DWI-SE sequence. A readout gradient is applied during echo acquisition to give spatial information.

determined for each pixel of the image and plotted in 2D to generate an ADC map. In general, regions with low diffusion will result in a flat linear regression curve and low D value on the ADC map. The opposite holds true for regions with high diffusion (Figure 1.11).

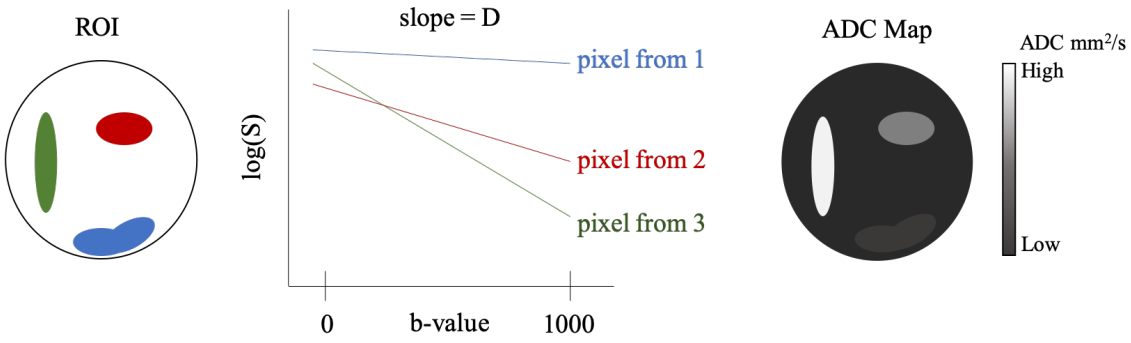

Fig. 1.11. Linear regression of signal intensity and b-value to determine apparent diffusion coefficients (mm^2/s).

1.2.3 DWI Applications

DWI can be applied to characterize and investigate the health of various tissues. One common application is in cases of brain ischemia when blood flow is cut off to certain regions of the brain. Brain regions experiencing restricted blood flow are marked by decreased ADC [35]. This can be helpful for diagnosing stroke severity and providing appropriate care. DWI can also be used to pinpoint malignant tumors in abdominal regions such as the pancreas and gall bladder [35]. Regions appear as hyperintensities on high b-value maps of the diffusion image (*not* ADC map). The hyperintense signals in these images result because the protons in the ROI have remained stationary and therefore have lost the *least* amount of signal intensity. While most applications focus on biological tissues, DWI can also be used to investigate implantable devices, such as ISFIs. Here, the 'tissue' of interest is now the ISFI which has been implanted into a desired tissue. How does the tissue environment affect the release of drug out of ISFIs over time? Answers to this question will be revealed in chapter five.

2. MRS INVESTIGATION OF A NOVEL TBI BIOMARKER: ACROLEIN

The increasing awareness of TBIs and lack of quantitative assessment tools warrant the investigation of novel TBI biomarkers. Magnetic resonance spectroscopy proves useful for the noninvasive analysis of tissues. While MRS experiments can provide information regarding physiological changes following TBI, investigations of the commonly studied brain metabolites do not result in quantitatively consistent findings across TBI studies [43–47]. Additionally, concentrations of these commonly studied brain metabolites (choline, creatine, myo-inositol, N-acetyl aspartate, glutamate/glutamine, and sometimes lactate) may change due to other factors such as age, gender, and diet. Lastly, most patients do not have baseline scans, and their metabolic concentrations cannot be compared to a healthy baseline. Therefore, it is critical to investigate alternative TBI biomarkers that can be consistently quantified across a spectrum of injury severities. Acrolein, an $\alpha\beta$-unsaturated aldehyde, has been shown to increase in brain tissues following contact- and blast-related TBI in animal models [48–50]. Because acrolein is specific to central nervous system injury, it is a promising biomarker of TBI. Chapter two presents acrolein as a novel MRS biomarker for TBI by first introducing TBI and acrolein.

2.1 Introduction to Traumatic Brain Injury: Epidemiology, Mechanisms, and Consequences of Injury

The Centers for Disease Control and Prevention (CDC) define TBI as "an injury that disrupts the normal function of the brain...caused by a bump, blow, or jolt to the head or a penetrating injury" [51]. TBI can be diagnosed as mild, moderate, or severe in severity, and symptoms, as well as length of symptom persistence, differ

based on diagnosis. A summary of TBI severity and corresponding symptoms are shown in Table 1.1 [52, 53].

Table 2.1.
Levels of TBI severity and associated symptoms.

TBI Severity	Symptom Category	Symptoms
Mild/Concussive	Physical Behavioral Cognitive	Headache, malaise, nausea, insomnia Irritability Memory impairment, lack of concentration
Moderate*	Physical Cognitive	Loss of consciousness < 30 minutes, seizure Post-traumatic amnesia >1 day
Severe*	Physical Cognitive	Loss of consciousness >24 hours (death, coma), seizure Post-traumatic amnesia >7 days

*includes mild symptoms

2.1.1 Epidemiology

Annually, approximately 2.8 million people are diagnosed with TBI in the United States [54]. The economic burden associated with these injuries is estimated at $60.4 billion, including both direct and indirect medical costs [55]. This number does not include military personnel, in which case roughly 20% experience a TBI during training and/or combat [56]. There are two primary types of TBI: contact- and blast-related. Contact-related TBIs occur when an object makes physical contact with the head as a result of a collision event; this causes the brain to press and deform against itself and the interior of skull [57]. Based on the angle and location of impact, different tissue-exerting forces can result; these include shearing, compression, and straining. Blast-related TBIs take place when an explosive device detonates near the head. This type of injury accounts for roughly 52% of all military-related TBIs [58]. The inertia of the blast wave propagates through the skull and into the brain, causing complex

deformation of tissue. Both mechanisms of injury result in primary and secondary injury cascades.

2.1.2 Mechanisms of Damage

Primary injury refers to the immediate damage caused by the contact or blast impact event. This can include hemorrhaging and microbleeding, compromised blood-brain-barrier, cavitation, and physical tearing or shearing of neurons and glia [58, 59]. Secondary injury can occur immediately following primary injury up to years after the injury and includes glutamatergic excitotoxicity, ischemia, and the activation of persistent neuroinflammatory cascades. These cascades produce endogenous toxins, such as free radicals and reactive oxygen species (ROS), which disrupt normal cellular processes, ultimately leading to mitochondrial dysfunction, cell death, tissue damage, and lipid peroxidation [60, 61]. Lipid peroxidation refers to the breakdown of lipids via free radicals which scavenge electrons from lipid molecules. In the case of TBI, the overproduction of free radicals and ROS results in damage to myelin and production of toxic secondary ROS (Figure 2.1). One such ROS is acrolein, a highly reactive and electrophilic α, β-unsaturated aldehyde with damaging effects on cellular functions [62].

2.1.3 Consequences of Damage

Long-term morbidity from TBI is referred to as chronic brain injury (CBI), and can vary by patient [63]. CBI can include multiple symptoms such as cognitive impairment, psychosis, chronic headache, and physical disability. Recent advances have also found significant associations between moderate and severe TBIs with Alzheimer's disease, Parkinson-like symptoms, and dementia [64]. Even one TBI event has been shown to cause significant increases in neurofibrillary tangles, tau hyperphosphorylation, and amyloid plaques [65–71]. In addition, it has been cited that psychosis and mental illness frequently appear long after the injury event [72]. This evidence

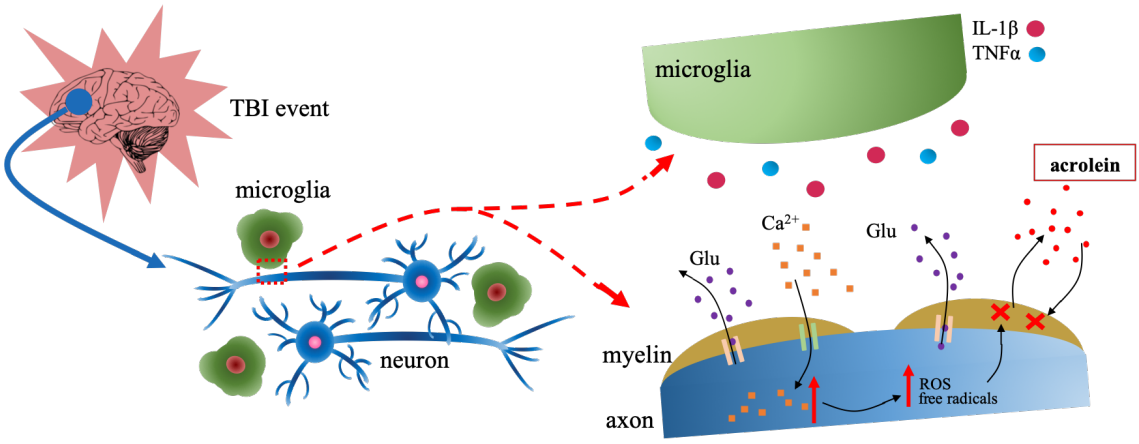

Fig. 2.1. Cascade of events following TBI. Physical damage to brain tissue results in membrane disruption and leakage. Neuroinflammatory molecules (Interleukin-1β, IL-1β and Tumor Necrotic Factor α, TNFα) are released from microglia and initiate production of ROS and free radicals. Glutamate is released from neurons at a high rate leading to glutamatergic toxicity. Calcium ions flood into the neuron, triggering neuroinflammatory cascades and subsequent production of ROS and free radicals. Acrolein, an ROS, is released as a byproduct of lipid peroxidation - an event triggered by initial ROS accumulation. Acrolein itself is a catalyst, causing subsequent membrane damage and mitochondrial dysfunction.

suggests that the sequalae of TBI is long-term, irreversible, and cumulative in nature. It has been hypothesized that the mechanism underlying these processes is persistent and toxic neuroinflammation [73, 74]. Acrolein is an important player in the neuroinflammatory pathway and can induce significant cellular damage [62].

2.2 Introduction to Acrolein

As mentioned, acrolein can be released as a result of a TBI event. Acrolein is a strong electrophilic ROS with a long half-life and damaging effects on cellular structures and systems [75]. It has also been shown to accumulate at high concentrations (1-500 μM) and diffuse to other brain regions (r = 10 mm) following injury [48]. Due

to its inherent characteristics and damaging effects following TBI events, acrolein is proposed as a potential biomarker of TBI.

2.2.1 Damaging Cellular Effects

Acrolein is released as a byproduct of lipid peroxidation following axonal damage [62]. Electrophilic ROS attack the lipid structure of myelin, causing membrane breakdown and production of secondary ROS (i.e. acrolein). Acrolein, itself, is a strong electrohpilic ROS, and thus has damaging effects on many nucleophilic structures (e.g. DNA and proteins) [76,77]. Specifically, acrolein targets sulphydryl groups on amino acids - important building blocks of proteins [77]. This can cause dysfunction on multiple levels including enzyme breakdown, detection of ROS, and redox signaling [77]. Furthermore, acrolein is a perpetuator of oxidative stress - a state in which the cellular environment is overwhelmed with ROS and cannot compensate with antioxidants (ROS scavengers) [78]. Because acrolein is both a product and catalyst of lipid peroxidation, it can exacerbate oxidative stress, leading to further cellular damage. Lastly, acrolein has been shown to cause mitchondrial dysfunction in some cells *in vitro*, eventually leading to cellular apoptosis [77, 78]. In summary, acrolein has been shown to 1) exacerbate membrane damage and lipid peroxidation, 2) cause mitchondrial dysfunction, and 3) perpetuate oxidative stress [48].

2.2.2 Half-Life

In addition to its host of damaging cellular effects, the half-life of acrolein (7-10 days) is longer than the typical ROS (10^{-12} seconds) [75, 78]. This observation emphasizes the catalytic affect of acrolein on prolonged oxidative stress and cellular damage. In addition, the long half-life suggests that acrolein could be 1) an excellent target for TBI treatment and therapy, and 2) acrolein can realistically be quantified and localized using MRS following an injury. But how is acrolein maintained for such long periods of time?

2.2.3 Scavenging Acrolein

Significant research has been done investigating acrolein scavengers as potential TBI treatments. Glutathione (GSH), an endogenous antioxidant, scavenges ROS and free radicals following central nervous system damage. Specifically, GSH scavenges acrolein via chemical conjugation; this process can occur without a catalyst [79]. The long half-life of acrolein may be, in part, due to its conjugation with GSH. By forming a more stable structure, acrolein can persist in the cellular environment for longer periods of time [48]. Following TBI, large amounts of ROS and free radicals are produced which GSH attempts to scavenge. However, acrolein has been shown to deplete these GSH stores at a rate 115-120 times faster than other potent ROS [80]. This 1) provides a mechanism for acrolein to persist in tissue, and 2) depletes GSH, allowing other ROS to induce further damage.

For these reasons, different treatments have been tested to improve ROS scavenging following central nervous system injury. One example is hydralazine which has been demonstrated to neutralize acrolein and its adducts [81]. Experiments conducted with *ex vivo* guinea pig spinal cords showed reductions in acrolein-related damage when hydralazine was administered 15 minutes following a spinal cord compression injury [82]. Additionally, hydralazine has been shown to be effective at reducing acrolein-mediated damage in both mice and rats [48]. Another potential treatment is with phenelzine - a monoamine oxdiase inhibitor. Phenelzine has been shown to prevent ischemic brain injury [83]. The benefit of phenelzine lies in that it is *not* a vasodilator; this trait would allow phenelzine to be administered at higher concentrations, potentially providing a greater therapeutic effect. Given these observations, the therapeutic effect(s) of potential scavengers could be monitored using acrolein as a therapeutic biomarker of tissue damage, both noninvasively and *in vivo*.

2.2.4 Summary of the Problem and Introduction to Research Approach

Due to the wide range of complications associated with TBI sequelae, it is critical to develop quantitative and noninvasive methods to further understand the prognosis of, and implement patient-specific therapies for, these injuries. Doing so could provide a means to (1) determine location(s) of the injury, (2) quantify the relative severity of injury, (3) monitor recovery, (4) assess the efficacy of treatments and rehabilitation therapies, and (5) ultimately improve the quality of life. However, no methods currently exist to noninvasively localize, evaluate, and monitor TBI severity.

Magnetic resonance spectroscopy (MRS) is a noninvasive nuclear magnetic resonance (NMR) technique that can be used to investigate the chemical profile of a specific body region. Clinically, MRS has been used to assist in the classification of brain tumors, altered brain metabolism, and multiple sclerosis [84–86]. These brain diseases can be classified by determining the concentration of metabolites in the range of 1-4 parts per million (ppm) on a ^{1}H (proton) NMR spectrum. The most commonly studied brain metabolites include N-acetyl aspartate (NAA), choline (Cho), creatine (Cr), myo-inositol (mI), glutamate/glutamine (Glx), and lactate (Lac). Because MRS is both noninvasive and quantitative, it is a promising method for monitoring brain health following a TBI. However, the commonly studied brain metabolites, listed above, show varying and/or minimal-to-no change following mild to moderate TBIs, making it difficult to translate this technique to the clinic [44, 46]. Additionally, other factors may contribute to changes in these brain metabolites such as diet, sleep, and exercise, again making it difficult to form conclusions and translate to the clinic [87–90]. Because the commonly studied brain metabolites remain relatively stable following TBI, and can be influenced by many outside factors, it is necessary to investigate novel MRS biomarkers of brain injury.

Acrolein, an $\alpha\beta$-unsaturated aldehyde, has damaging effects on cellular functions. Exogenously, acrolein is released into the environment when fats and oils are burned at high temperatures. Endogenously, acrolein is a byproduct of lipid peroxidation

and is released when axons and myelin are damaged. In the brain, acrolein can cause membrane damage and disrupt mitochondrial functions, ultimately resulting in significant oxidative stress and cellular dysfunction and/or death [48, 62, 91, 92]. Acrolein can persist in the body from hours to days following injury, making it a prime candidate for clinical MRS analysis and follow-up [48,75,93]. In rat brain tissue, acrolein has been shown to increase following contact and blast TBIs; however, current methods to quantify acrolein remain largely sacrificial [50,92,94,95]. In addition, only one of the acrolein adducts have been quantified, suggesting that reported values may be underestimates of true biological concentrations [96, 97]. Less invasive methods have been attempted to quantify an acrolein byproduct, 3-HPMA, in urine. While successful in animal studies and in human subjects, methods are unable to specifically localize acrolein, a key piece of information required to predict functional loss and guide treatments [97]. Recent studies have discovered promising blood biomarkers for TBI [98, 99]. However, similar to urine 3-HPMA, many blood biomarkers are not specific to the CNS, are only elevated acutely in cases of more severe TBI, and therefore have not been used clinically. Thus, it is crucial to investigate alternative biomarkers using different methodologies that will not only provide temporal, but also spatial resolution.

Although a majority of MRS research focuses on the spectral range of 0-4 ppm, there has been increasing interest in metabolites downfield of 4 ppm, including larger macromolecules and aldehydes. Based on findings from the Human Metabolome Database, acrolein, an aldehyde, shows resonances at 6.4 ppm and 9.3 ppm [100]. However, acrolein has not yet been investigated using the more clinically relevant method, MRS. Additionally, acrolein levels have been shown to peak between 24-72 hours post-TBI, making it a prime biomarker candidate for TBI given the time window commonly associated with the development and reporting of symptoms [78, 94]. Notably, acrolein can be monitored over extended periods of time given its long half-life [93, 101].

Current methods to assess TBI are qualitative, invasive, and/or nonspecific. By using acrolein as a biomarker for TBI and standard MRS protocols, it may be possible to map injury location and quantify injury severity. With knowledge of injury location and severity, patient-specific treatment and rehabilitation strategies can be developed to enhance recovery and decrease long-term morbidity. Additionally, implementation of MRS does not rely on patient factors such as language, age, etc. and can thus be used in any clinical setting with access to an MRI. However, to become clinically translatable, methods must be developed and validated to noninvasively quantify acrolein with both high sensitivity and specificity. Using acrolein as a biomarker for TBI is novel and requires extensive experimentation before *in vivo* validation. In this work, we present results from NMR and pre-clinical 7 tesla (T) MRS experiments. Results from these experiments will guide the development of MRS protocols that can be used for *in vivo* experiments with rodents for eventual implementation in human subject protocols.

2.2.5 Materials and Methods

NMR Experimentation

Experiments were conducted in an ARX300 (7T) NMR system (Bruker, Billerica, MA, USA). Neat acrolein (Sigma Aldrich, Cat. #4S8501) was diluted to 90 mM in D_2O for T_1 and T_2 experiments. T_1 relaxation was determined using an inversion recovery sequence; eight-point measurements were taken with delay times of 0.01, 2.5, 5, 8, 12, 18, 30, and 50 seconds. T_2 relaxation was determined using the Carr-Purcell-Meiboom-Gill (CPMG) sequence (RF field strength = 23 kHz) [27]; eight-point measurements were taken with delay times of 0.08054, 0.8054, 2.416, 4.832, 8.054, 16.108, 24.162, and 32.216 seconds. Both the T_1 and T_2 experiments were performed in triplicate, and resulting spectra were averaged across the three trials. MestReNova was used to calculate T_1 and T_2 relaxation times by fitting the curves with a three-parameter exponential fit [102].

Additional experiments were conducted in an AV800 (18.8 T) NMR system (Bruker, Billerica, MA, USA). One M acrolein was diluted to 900 mM using D_2O as the solvent. 1D ^1H and NOESY experiments were conducted at 800 MHz, and the 1D ^{13}C spectrum was obtained at 200 MHz. MestReNova was used for all data processing.

MRS Experimentation

Corresponding to the 7 T static magnetic field of the ARX300 NMR system, localized MRS experiments were conducted in a 7 T pre-clinical MRI system (Bruker BioSpec 70/30 USR, Billerica, MA, USA). Neat acrolein was diluted with MilliQ water to create three solutions: 1 M, 100 mM, and 10 mM. Solutions were prepared in 1.5 mL Eppendorf tubes and secured and centered in a circularly polarized mouse head ^1H volume coil (RF RES 300 ^1H 023 M.BR QSN TR, Bruker, Billerica, MA, USA). Standard Point RESolved Spectroscopy (PRESS) was used for all MRS experiments. Based on our results from NMR experiments and the long T_1 and T_2 expected from aldehydes, repetition time (TR) was adjusted for MRS experimentation using the following equation where $T_{1,water}$ = 4 seconds, $T_{1,acrolein}$ = 12 seconds, and X = scaling factor:

$$T_{1,water} = X(T_{1,acrolein}) \tag{2.1}$$

The scaling factor, X, was then used to determine the appropriate TR where TR_{std} = TR of the standard PRESS sequence, X = scaling factor determined in equation 2.1, and $TR_{acrolein}$ = calculated TR for acrolein experiments:

$$\frac{TR_{std}}{X} = TR_{acrolein} \tag{2.2}$$

Initial experiments were conducted to alter the TE and flip angle. However, there was no improvement in signal-to-noise ratio (SNR) and, therefore, only TR was altered for all following experiments. PRESS parameters were adjusted (TE = 16.5 ms; TR = 6000 ms; 256 averages; 3 mm^3 voxel; flip angle = 90°/180°/180°; pulse BW

= 5.4/2.4/2.4 kHz, spoiler gradient duration 3 ms, read/phase/slice spoiler gradient strengths 56.0/-56.0/56.0 mT/m around first refocusing pulse, 6.6/79.2/79.2 mT/m around second refocusing pulse, t = 25:36 minutes. Standard localizing, B_0 mapping, and shimming procedures were completed prior to PRESS imaging. Data quality was checked using TopSpin (Bruker, Billerica, MA, USA) and later visualized and analyzed using MestReNova, which has the capabilities to fit and quantify metabolites not available in TARQUIN. Data from PRESS experiments were Fourier transformed and peaks were integrated using water as an internal reference.

Phantoms were developed to simulate normal brain tissue. To prepare a whole-brain phantom for acrolein injection and 7 T MRS experimentation, measurements were calculated using percent values indicated on the Braino MRS phantom (GE Medical Systems, Milwaukee, WI, USA). Potassium phosphate monobasic anhydrous, 0.68% w/v (VWR Life Sciences, Cat. #0781-500G), L-glutamic acid monosodium salt monohydrate, 0.234% w/v (Alfa Aesar, Cat. #A12919), N-acetyl-L-aspartic acid, 0.219% w/v (Sigma Aldrich, Cat. # 00920-5G), myo-inositol, 0.135% w/v (Dot Scientific, Cat. #DS154040-100), g sodium hydroxide, 0.226% w/v (pH buffer; BDH, Cat. #BDH9292-500G), creatine, 0.15% (Spectrum, Cat. #CR105), choline chloride, 0.05% w/v (Dot Scientific, Cat. #DSC1040-100), DL-lactic acid lithium salt, 0.05% w/v (MP Biomedicals, Cat. #100824), gadolinium, 0.047% w/v (contrast agent; Sigma Aldrich, Cat. #381667), and sodium azide, 0.1% w/v (preservative; Dot Scientific, Cat. #DSS24080-250) were measured using an analytical balance and dissolved with RODI water to make a 200 mL solution. The solution was equally portioned into 30 mL bottles, equating to 40 mL per bottle when filled to the brim. Metabolite concentrations were verified using a rat head/mouse body 1H volume coil (RF RES 300 ^{1}H 075/040 QSN TR, Bruker, Billerica, MA, USA) and a standard PRESS sequence (TE=16.5 ms; TR=2500 ms; 256 averages; 3 mm^3 voxel). Data were processed and visualized using TARQUIN to compare whole-brain phantom metabolic concentrations to normal human neurometabolic concentrations [22]. Four-hundred μL of 1 M stock acrolein was subsequently injected into the 40 mL whole brain

phantom, creating a 10 mM solution. The phantom was centered in the volume coil and PRESS imaging was completed. Creatine (0.15% w/v) was used as the internal reference for whole-brain phantom analysis.

2.2.6 Statistical Analysis

An unpaired, unequal variances, two-tailed t-test ($\alpha = 0.05$) was performed to determine if there was a significant difference between average human brain metabolic concentrations and metabolic concentrations in the whole-brain phantom.

2.2.7 Results

The whole-brain phantom was validated first using 7 T MRS. Using water as an internal reference, the calculated concentrations of metabolites in the whole-brain phantom were not significantly different from average metabolic values of the human brain (Figure 2.2; $p = 0.75$).

From the 7 T NMR acrolein experiments, T_1 for the proton peaks at 9.3 ppm equated to 13.31 seconds and T_1 for the proton peaks between 6.3-6.6 ppm equated to 11.19 seconds (Figure 2.3). T_2 for the proton peaks at 9.3 ppm equated to 11.17 seconds and T_2 for the proton peaks between 6.3-6.6 ppm equated to 9.26 seconds (Figure 2.4).

PRESS spectra obtained from different dilutions of acrolein in the 7 T MRS scanner are shown in Figure 2.5. For whole-brain phantom, 10 mM acrolein was detectable at 7 T (Figure 2.6). Results from water and whole-brain phantoms are summarized in Table 2.1. 1D ^{1}1H and NOESY experiments conducted at 800 MHz are shown in Figures 2.7 and 2.8, and the 1D ^{13}C spectrum obtained at 200 MHz is displayed in Figure 2.9.

	mI	Cho	Cr	Glx	NAA
Average Human Brain (mM)	5.54	2.52	11.51	13.74	16.89
Whole Brain Phantom (mM)	6.16	4.66	14.52	13.80	17.75

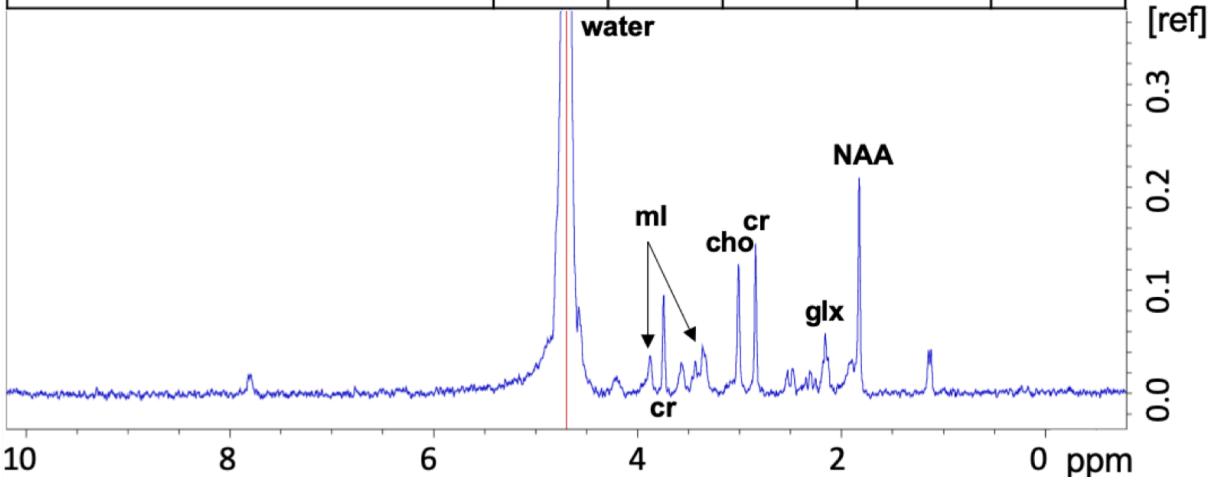

Fig. 2.2. Whole-brain phantom spectral validation. Spectrum from the whole-brain phantom was obtained using a standard PRESS sequence on a Bruker pre-clinical 7 T MRI system with the Bruker rat head/mouse body coil. Data were fitted using TARQUIN and a human brain basis set. Metabolites were not statistically different when comparing average human brain and whole-brain phantom values ($p = 0.75$) validating the use of whole-brain phantoms in future phantom analyses.

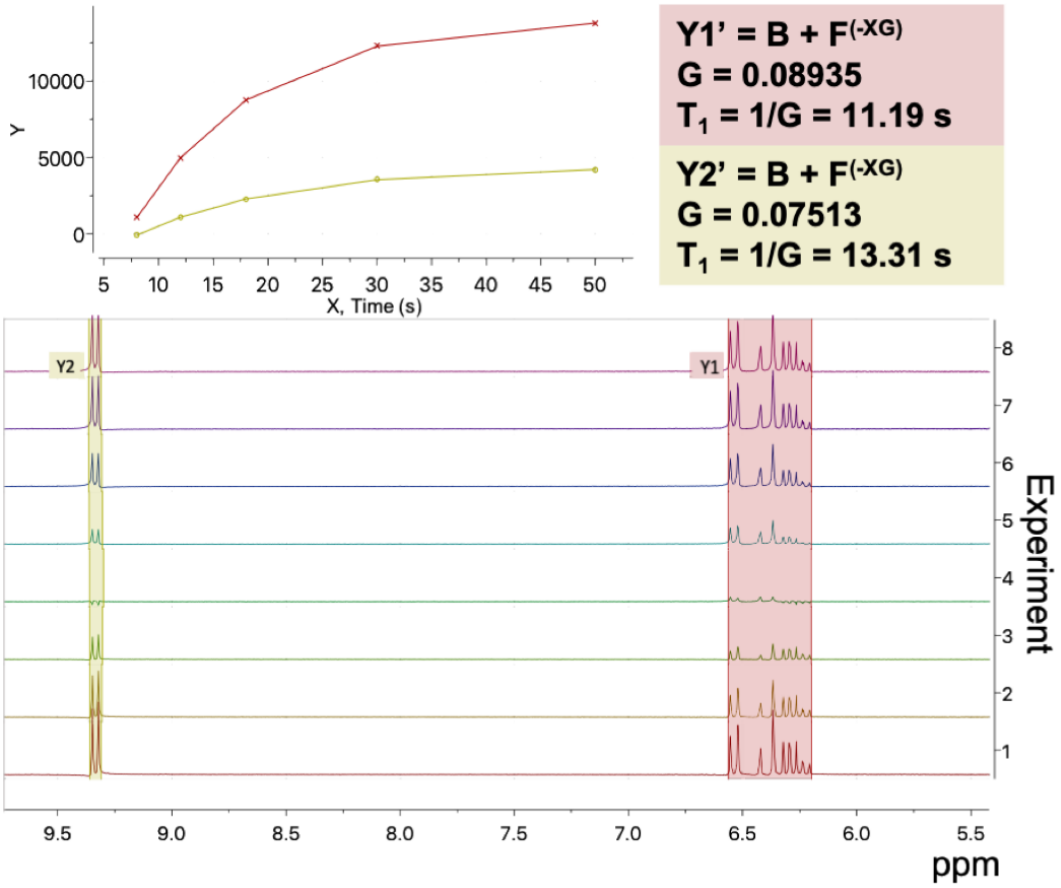

Fig. 2.3. Calculation of T_1 for each selected peak region performed by fitting the curves with a three-parameter exponential fit, with $G = 1/T_1$. T_1 for the proton peaks at 9.3 ppm equals 13.31 seconds, and T_1 for the proton peaks between 6.3-6.6 ppm equals 11.19 sesconds.

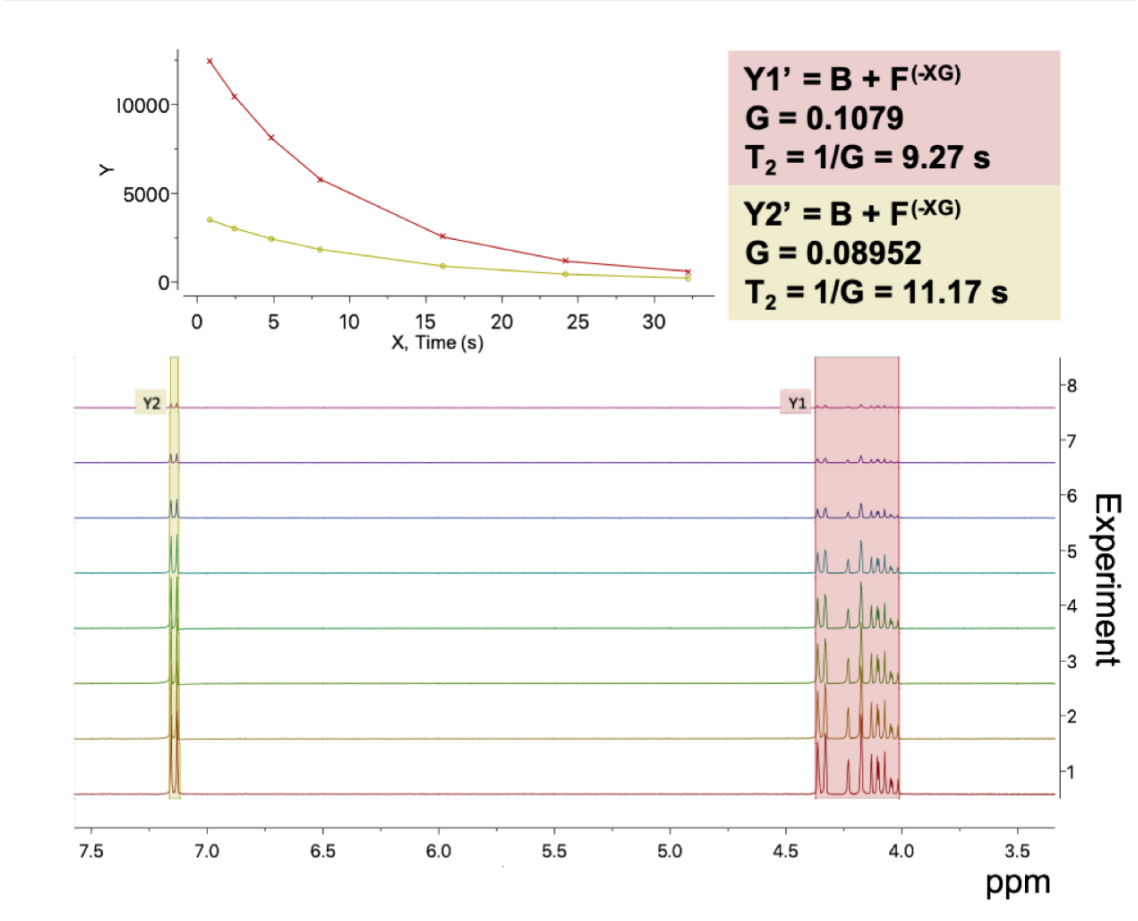

Fig. 2.4. Calculation of T_2 for each selected peak region performed by fitting the curves with a three-parameter exponential fit, with $G = 1/T_2$. T_2 for the proton peaks at 9.3 ppm equals 11.17 seconds, and $T_2 2$ for the proton peaks between 6.3-6.6 ppm equals 9.26 seconds.

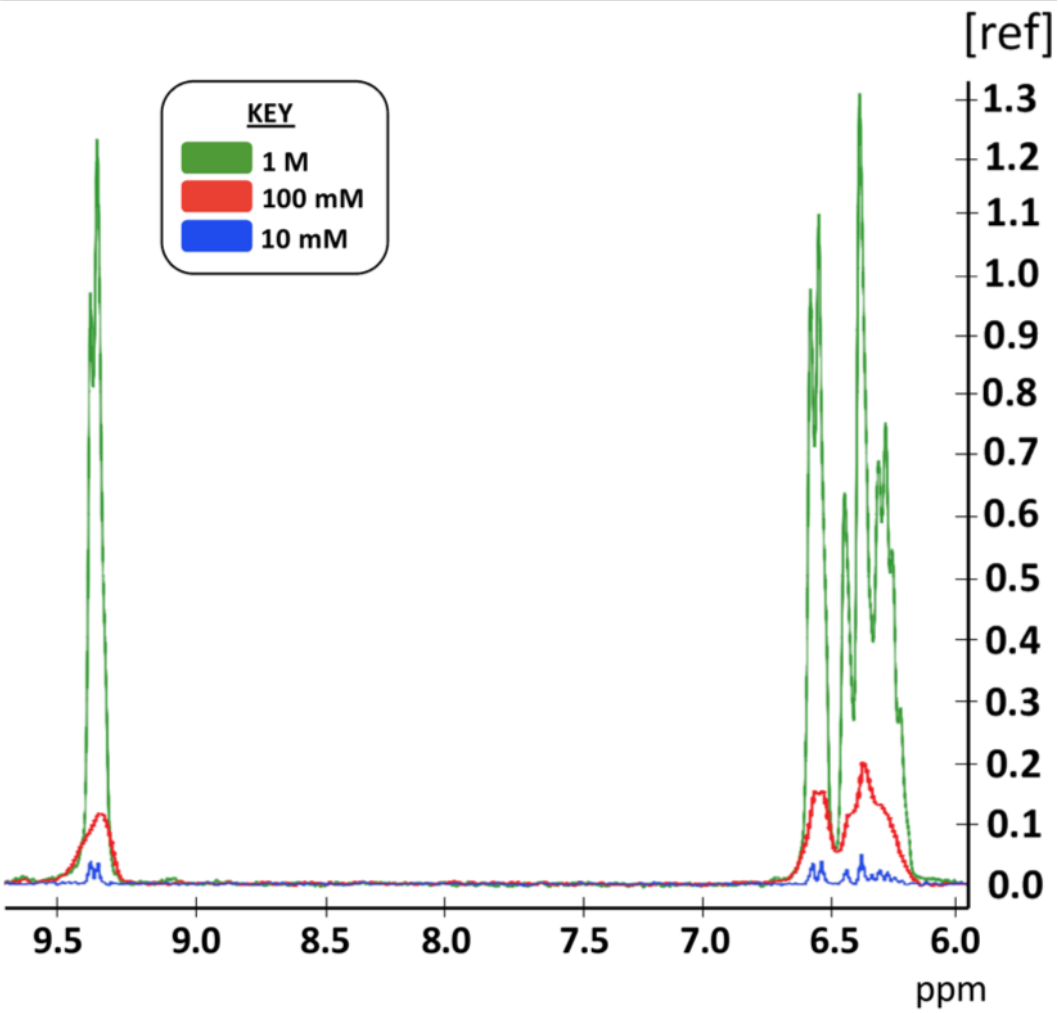

Fig. 2.5. PRESS spectrum obtained from 7 T/300 MHz Bruker pre-clinical MRI system. Acrolein was diluted to three concentrations: 10 mM, 100 mM, and 1 M. Acrolein peaks are located at 6.3 ppm, 6.5 ppm, and 9.4 ppm. The spectrum confirms the sensitivity of a 7 T pre-clinical MRI system to detect acrolein signal using PRESS.

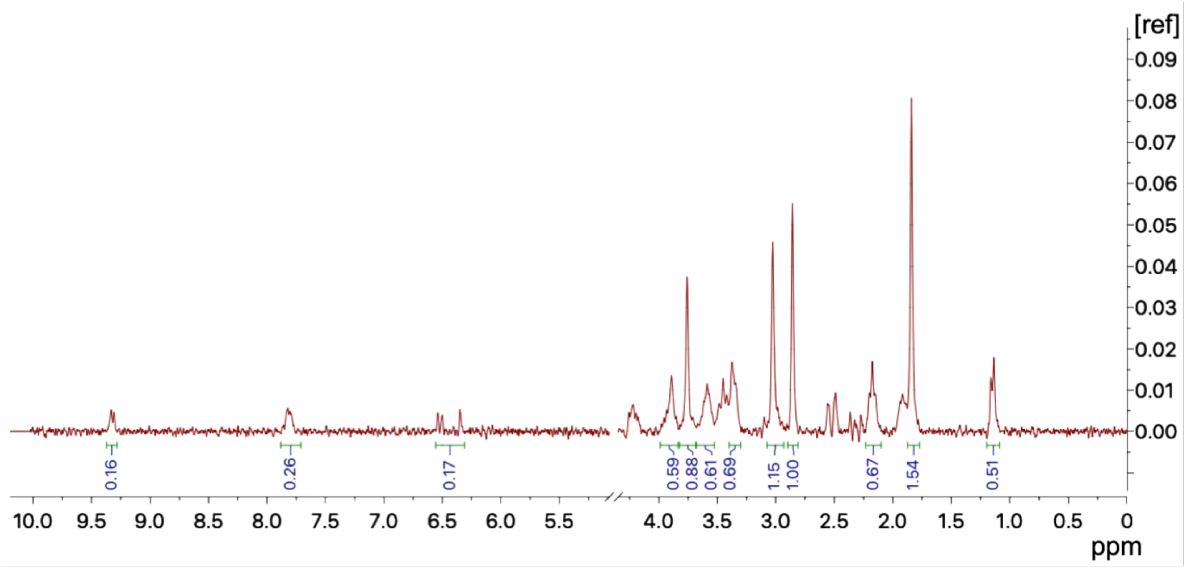

Fig. 2.6. Spectrum from whole-brain phantom injected with acrolein. Spectrum from a 10 mM solution of acrolein injected into a whole-brain phantom. The spectrum relays the relative magnitude of signal obtained from acrolein compared to normal brain metabolites.

Table 2.2.

Results from Acrolein Peak Integration — Acrolein peaks were manually integrated for all solutions using MestReNova. The complex multiplet was integrated between 6.3 and 6.6 ppm. The doublet was integrated between 9.25 and 9.4 ppm. Water was used as an internal reference for the water phantom and creatine was used as the internal reference for the whole-brain phantom.

Solution Concentration	Phantom Type	Reference Peak	6.3-6.6 ppm Integration	6.3-6.6 ppm Integration
10 mM	Water	Water	0.04	0.01
100 mM	Water	Water	0.09	0.03
1 M	Water	Water	0.84	0.27
10 mM	Whole-brain	Creatine	0.17	0.16

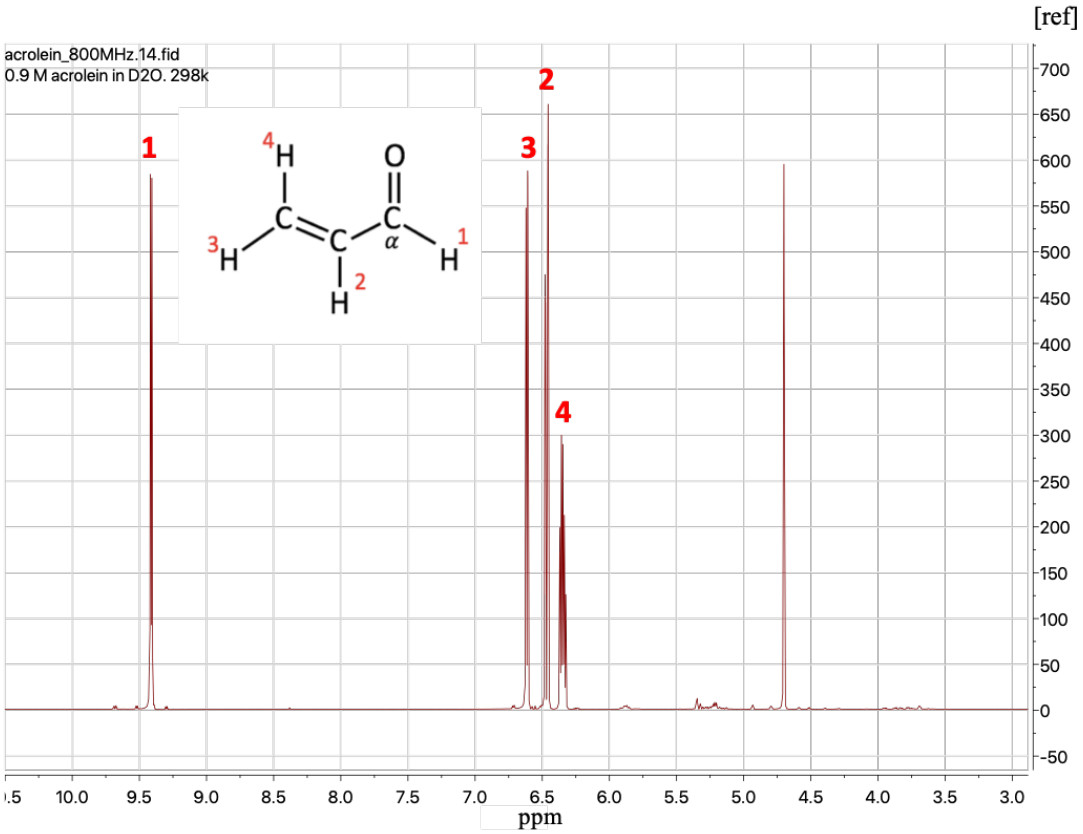

Fig. 2.7. ^{1}H NMR acrolein spectrum. Spectrum was obtained with an AV800 (800 MHz) NMR system at 800 MHz. Acrolein peaks have high intensity signal around 6.5 ppm and at 9.4 ppm. The SNR obtained with NMR experimentation is drastically higher than with MRS. Solvent residual peak is observable at 4.7 ppm. The labile proton, labeled 2, is suggested to be bonded to the alpha hydrogen.

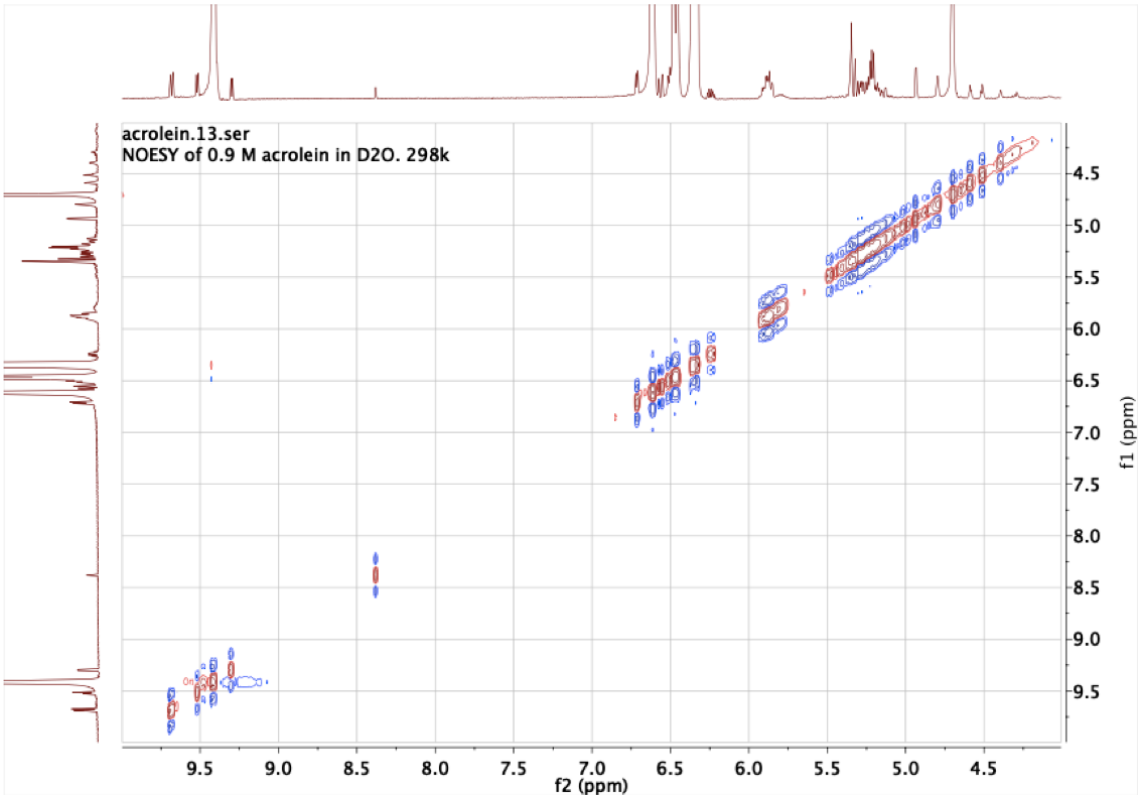

Fig. 2.8. ^{1}H 2D NOESY acrolein spectrum. Spectrum was obtained with an AV800 (800 MHz) NMR system at 800 MHz. The 1D spectrum is positioned above and to the left of the NOESY spectrum to correlate residues between 1D and 2D spectra. There do not appear to be significant through-space interactions between acrolein protons.

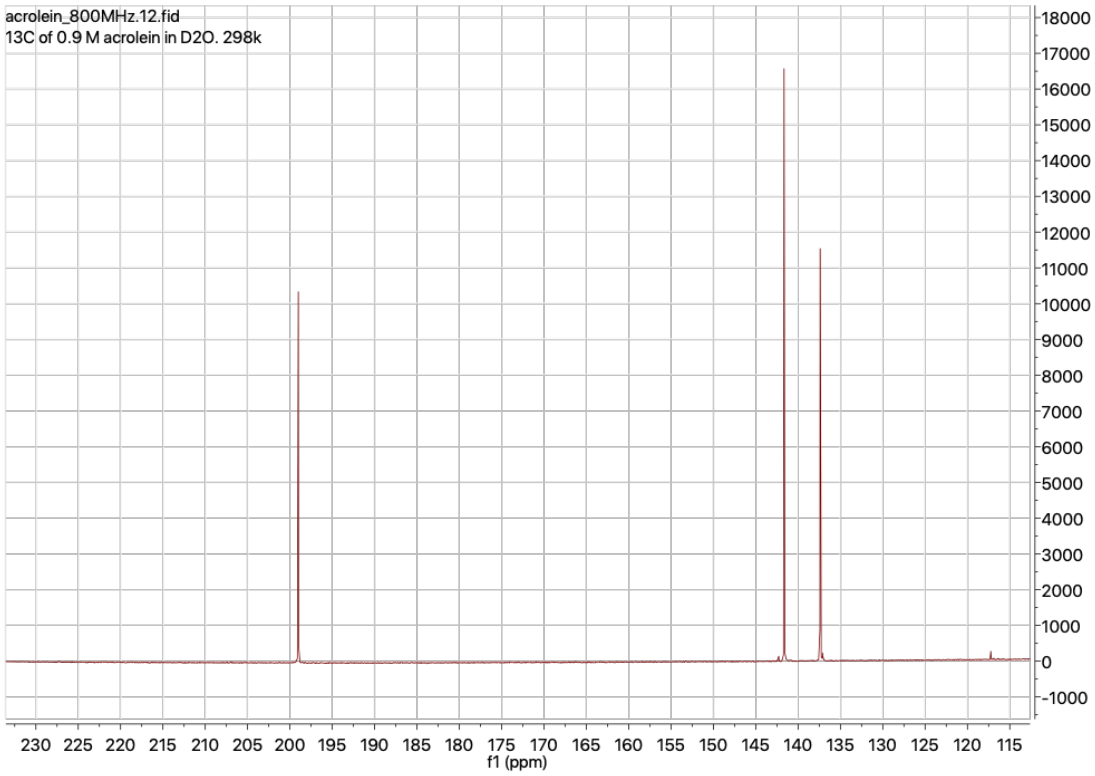

Fig. 2.9. ^{13}C NMR acrolein spectrum. Spectrum was obtained with an AV800 NMR system at 200 MHz. Acrolein peaks have high intensity signal around 137, 142 and 199 ppm.

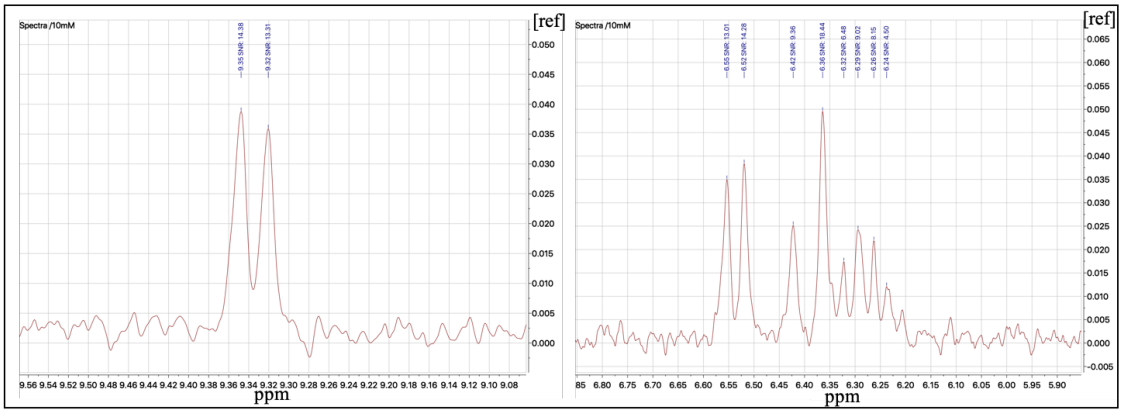

Fig. 2.10. SNR analysis of a 10 mM concentration of acrolein. The average SNR between 6.24-6.55 ppm is 10.41. The average SNR between 9.32-9.35 ppm is 13.85.

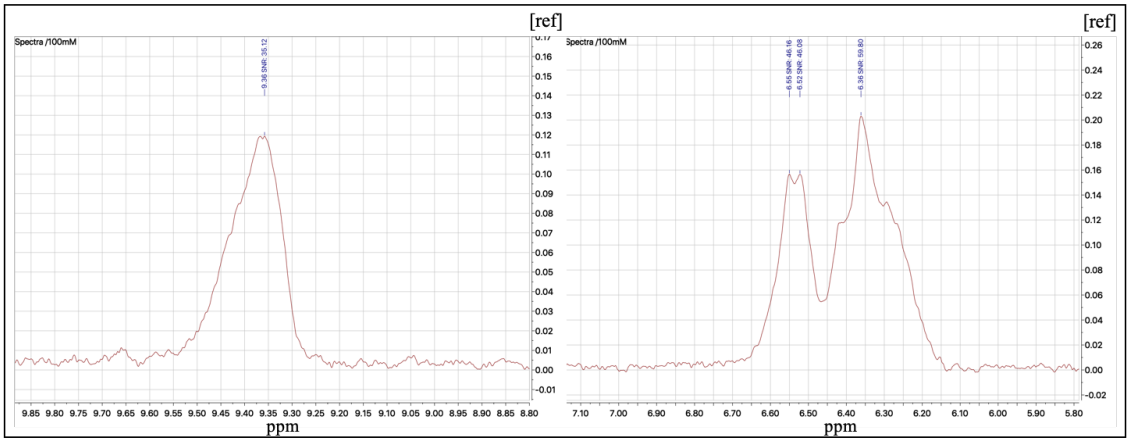

Fig. 2.11. SNR analysis of a 100 mM concentration of acrolein. The average SNR between 6.24-6.55 ppm is 50.68. The average SNR between 9.32-9.35 ppm is 35.12.

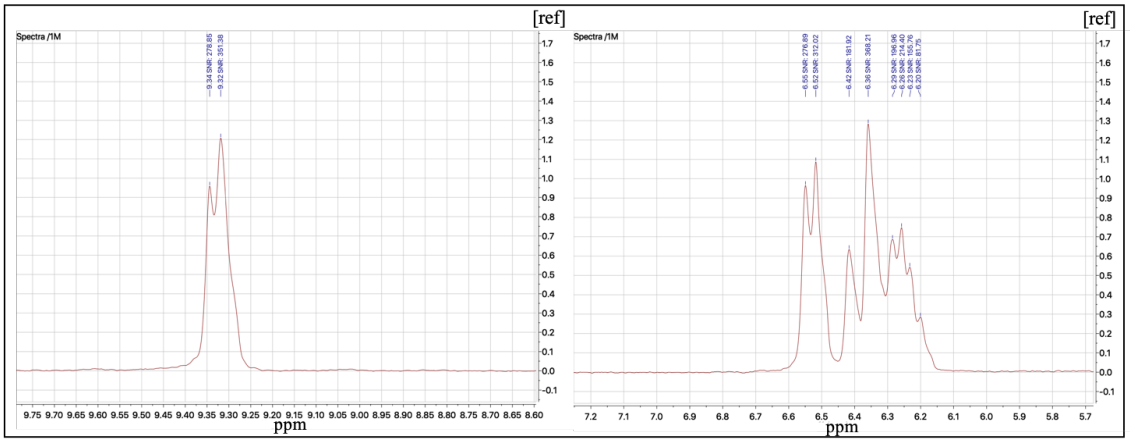

Fig. 2.12. SNR analysis of a 1 M concentration of acrolein. The average SNR between 6.24-6.55 ppm is 223.49. The average SNR between 9.32-9.35 ppm is 315.12.

2.2.8 Discussion

With the increasing awareness of TBI in military training and combat and contact sports, and the associated long-term disabilities associated with these injuries, it is critical to investigate novel methods to better localize and quantify injury severity. Doing so could offer valuable clinical insight to specialize patient treatment and rehabilitation plans. While some MRI methods, such as functional MRI and diffusion tensor imaging, require intensive data processing, MRS data can be analyzed in the matter of minutes and include brain region spatialization and analysis of metabolite concentrations. Studies analyzing metabolites in the 0-4 ppm range show relatively inconsistent data regarding concentration changes following TBI, confirming the need to investigate alternative biomarkers.

Acrolein, an endogenous neurotoxin, is a prime candidate for investigating TBI as it is known to increase in brain tissue following physical damage to neuronal tissue. We have demonstrated that acrolein can be quantified in a pre-clinical MRI system, suggesting further applications in animal and human studies. Using data obtained from *ex vivo* NMR experiments, *in vivo* MRS protocols can be adjusted to improve the SNR of acrolein, thereby decreasing the limit of detection from millimolar concentrations to micromolar. An analysis of peak-specific SNR from the 7 T MRS experiments can be viewed in Figures 2.10-2.12. However, there remains a drop in signal when comparing NMR and MRS data. The large drop in signal can result from magnetic field inhomogeneities, gradient imperfections, sample concentration, acrolein purity and stability, and is confounded by the long acrolein-associated T_2 compared to TE. Previous studies have reported long relaxation times associated with aldehydes, confirming the long T_1 and T_2 times of acrolein [103–105]. Acrolein, a small, mobile molecule, has a high rate of molecular motion which results in longer T_1 relaxation [106, 107]. An increase in T_1 occurs because the rate of motion is higher than the Larmor frequency. This effect becomes even more apparent at higher field strengths, like 7 T [107]. For these reasons, it is rational to believe the lengthy

acrolein-associated T1 time. T_2 should be equal to or less than T_1, and a typical proton T_2 is 1-10 seconds [106]. However, due to acroleins small molecular weight, size, and high rate of molecular motion, the T_2 relaxation is long, but still less than T_1.

By obtaining T_1 and T_2, TR can be adapted to ensure acrolein reaches a complete relaxation and enough time is allotted to obtain maximum signal. T_1 refers to the time it takes for the protons of a particular molecule or metabolite to relax longitudinally, to which they are tipped using radiofrequency pulses, back to the z-plane of the magnetic field. Because acrolein is a reactive, small aldehyde, its T_1 relaxation time is quite long, thereby lengthening TR, and consequently, scan time (t=25:36). Although the scan time is longer than typical spectroscopic imaging procedures, it can provide invaluable information regarding the precise location of an injury and relative concentration of acrolein following TBI. This procedure would be most valuable for patients who require rehabilitation following initial hospitalization as spatial acrolein maps could be used to indicate primary regions of injury for patient-specific rehabilitation plans.

To date, no MRS methods have been validated to give ground truth *in vivo* metabolic concentrations, and the true, physiological levels of brain metabolites remain unknown [21]. This is in part due to the inability to perform invasive *in vivo* procedures to extract exact tissue concentrations. Methods do exist to quantify metabolites *ex vivo*, however, these values are not a true representation of physiological levels. To address these issues, quantitative methods have been developed to produce relative metabolite concentrations. The three most common methods for *in vivo* spectroscopy are 1) use of a phantom with known metabolic concentrations (i.e. an external reference), 2) use of an internal reference (e.g. water or creatine), or 3) use a basis set provided by a post-processing software [17].

The most widely used method is the use of an internal reference. Water exists in all biological tissues, including the brain. Because of its abundance, the water peak typically overshadows peaks of interest. To combat this problem, water is nor-

mally suppressed in parallel with the MRS pulse sequence. However, if a non-water-suppressed scan is completed, the known concentration of unsuppressed water (80 M in human brain) can be used as an internal reference [16, 18, 87]. Creatine, a known brain metabolite, may also be used as an internal reference; results using this method are reported as ratios to creatine (e.g. Glx:Cr) [17]. Creatine has been reported to remain stable in many TBI studies, hence its frequent use as a reference [46, 108]. However, some studies have reported changes in creatine following TBI [109].

Figures 2.5 and 2.6 depict the relative concentrations of acrolein using the internal reference methods described. Discrepancies between acrolein concentrations in the water phantom versus the whole-brain phantom result from use of a different reference molecule (i.e. water vs. creatine). Although creatine has been reported stable in TBI many studies, it has also been reported to fluctuate [42]. For this reason, best practice would be to conduct a non-water-suppressed reference scan and use water as an internal reference for acrolein concentration calculations.

The possibility remains that signal will drop too significantly when transitioning protocols to phantoms to animal models and human subjects. In the case that acrolein is undetectable, byproducts can be investigated, such as 3-HPMA. Additionally, acrolein is scavenged by the antioxidant, glutathione (GSH) which has been measured using MRS methods in human subjects. Acrolein has been shown to deplete GSH stores, and it can be hypothesized that GSH would decrease in the brain following TBI [80]. However, GSH also scavenges other free radicals, making it impossible to conclude that a decrease in GSH corresponds solely to an increase in acrolein. However, using both 3-HPMA and GSH, it is possible to indirectly quantify acrolein since 3-HPMA is a direct byproduct of the reaction between GSH and acrolein. An additional alternative would be the use of a human 7 T MRI system. These systems are becoming increasingly popular for use in clinical research as the higher magnetic field greatly improves the SNR and quality of the data obtained. As 7 T systems increase in popularity and use, it would be possible to implement animal-based pro-

tocols devised and tested with 7 T pre-clinical MRI systems (e.g., Bruker) on human subjects.

Overall, the quantification of acrolein using MRS, and potentially magnetic resonance spectroscopic imaging (MRSI), could provide valuable information regarding the location and severity of brain damage. MRS typically uses a single voxel which can be placed in any region of interest; whereas, MRSI can be used to quantify metabolites across the entire brain. Future work must be done to improve the SNR of acrolein first using a single voxel, followed by translation to MRSI protocols. Using MRSI also increases the scan time a feature that must be considered when developing techniques for clinical use. However, the benefit of discerning precise injury location may vastly outweigh the disadvantage of lengthened scan time required to obtain the spectra. Additionally, animal studies must be completed to 1) correlate injury severity with the normalized concentration of acrolein using the unsuppressed water signal as a reference, 2) establish a time course of acrolein *in vivo*, over time, and 3) develop a model that can predict the severity of injury based on the concentration of acrolein observed. Lastly, it is critical to develop a basis set for acrolein in the context of human brain MRS. This would allow for the use of brain-specific MRS tools, such as Tarquin and LC Model, for more accurate fitting of acrolein peaks in relation to other brain metabolites [110,111]. This would, additionally, eliminate the need for an unsuppressed water reference scan, thereby decreasing scan time and making it more feasible for clinical applications.

Due to the high incidence and prevalence of TBI, particularly at mild severity, and its association with long-term disabilities, it is crucial to investigate methods that can assist with the diagnosis, treatment, and rehabilitation of patients. Using acrolein as a biomarker for TBI, and adjusted MRS methods, it is possible to create a map of injury severity across the brain. By doing so, a physician could assess where the most severe damage is located and implement patient-specific regimens for treatment and therapy. In addition, these methods could be used to evaluate the efficacy of

pharmaceuticals developed to reverse existing, or prevent further damage, following TBI.

3. POSITION-SPECIFIC MRS INVESTIGATION AND HEAD IMPACT ANALYSIS IN A COHORT OF HIGH SCHOOL AMERICAN FOOTBALL PLAYERS

3.1 Introduction: Sports-related Traumatic Brain Injury

Of the estimated 2.8 million annual TBI events, the highest rate of contact-related, TBI-associated emergency department visits and hospitalizations occurred in those aged 4-24 and were most likely due to participation in a sports-related activity [54]. In total, it has been estimated that 1.6-3.8 million sports-related concussions occur each year, and 30% of these concussions occur in males, aged 15-19 [112]. Because the largest prevalence of sports-related concussions falls in this demographic category, it is important to understand the epidemiology of mTBI in high school athletes [113].

Out of twenty high school sports, the highest incidence (51%) of concussion was reported in football [114]. In addition, football has the highest participation rate among high school athletics [115]. Despite this fact, it is also well-documented that sports-related TBIs, specifically mild TBI (mTBI), or concussion, commonly go underreported and undiagnosed. This can be attributed to multiple factors including lack of obvious symptoms and awareness, concerns with play time and avoidance of reporting, and lack of accurate quantitative methods to accurately diagnose mTBI [116–119].

Not only are concussions concerning; cumulative subconcussive hits have also been show to contribute to a severe, neurodegenerative disorder, chronic traumatic encephalopathy (CTE) [120, 121]. Before its terming, CTE was referred to as *dementia pugilistica*, or punch-drunk, and was first noticed in professional boxers [122, 123]. The unique pathology of CTE was then discovered by Bennett Omalu in professional American football players and studied extensively by Anne McKee in the following years [124–128]. Initial symptoms of CTE manifest as loss of attention and concen-

tration, declining memory, and headache and dizziness [129]. As time progresses, symptoms also progress to include aggressive and violent behavior, impulsivity, development of abuse disorders, and depression and suicide [125,129]. Eventually, there can be loss of motor skills, development of Parkinsonian symptoms, loss of hearing, and dementia [130]. While only a fraction of high school athletes will make it to the professional leagues, the magnitude of cumulative hits sustained during a single season of high school football is alarming [131, 132]. Broglio et al. (2011) reported a staggering 652 average head impact events (>15 g) over a two-week period and seasonal linear acceleration accumulating to 16,746 g. Another study by Bari et al. (2018) reported a cumulative translational acceleration of 12,770 g over the course of the season. Hits data, combined with neuroimaging, can provide profound scientific discovery on the mechanisms underlying sports-related concussion. Specifically, MRS can offer insights into potential neuropathology. The following paragraphs will provide 1) an overview of the devices used to monitor head impacts, 2) variations in HAEs across player positions, 3) a brief summary of the metabolites of interest used in MRS, and 4) the regions of interest.

3.1.1 Hit Monitoring Systems

Recent efforts have been made to quantify the number and magnitude of head acceleration events experienced by collision-sport athletes. By large, the most common method is the use of sensors which include accelerometers. Sensors have been engineered to attach to helmets, adhere to the skin, or embed in mouthguards [133–135]. Each method has associated pros and cons. Head-mounted systems were reported more accurate than helmet-mounted systems when testing the reliability of translational/linear and rotational accelerations [134]. For this reason, head-mounted systems are preferred over helmet-mounted sensors. In particular, the X2 Patch provided reliable quantification head acceleration events (HAEs) when put through a battery of impact tests [134]. Mouthguards provide a promising opportunity for accurate hit

quantification. However, great care must be taken in their design to avoid hazards such as electrocution - especially since the electronics are being placed in a moist environment. For the following studies, the X2 Patch (X2 Biosystems; Seattle, WA) head-mounted sensor was utilized.

3.1.2 Position-Specific Variations in Head Acceleration Events (HAEs)

Previous studies have investigated differences in HAEs across American football positions. The various football positions are depicted in figure 3.1 with linemen positioned on the center line of scrimmage and non-linemen positioned at various other points on the field. In the present study, the term non-linemen includes the quarterback, running back, wide receiver, safety, and cornerback. The linemen term includes both offensive and defensive linemen (i.e. tight end, tackle, guard, etc.). Broglio et al. (2009 and 2011) reported a significantly higher cumulative linear acceleration in defensive linemen and offensive non-linemen compared to other positions [131, 132]. In addition, it has been observed that linear acceleration events are higher on days where a player has been diagnosed with concussion [136]. Talavage et al. (2014) reported significantly higher HAEs in players who did not exhibit clinical impairment but who did show functional impairment, as measured with fMRI [120]. Specifically, the highest number of high magnitude hits in this group occurred on the top-front of the helmet. Together, position seems to play an important role in the magnitude of HAEs experienced over the course of a season, and could potentially predict neurophysiological changes.

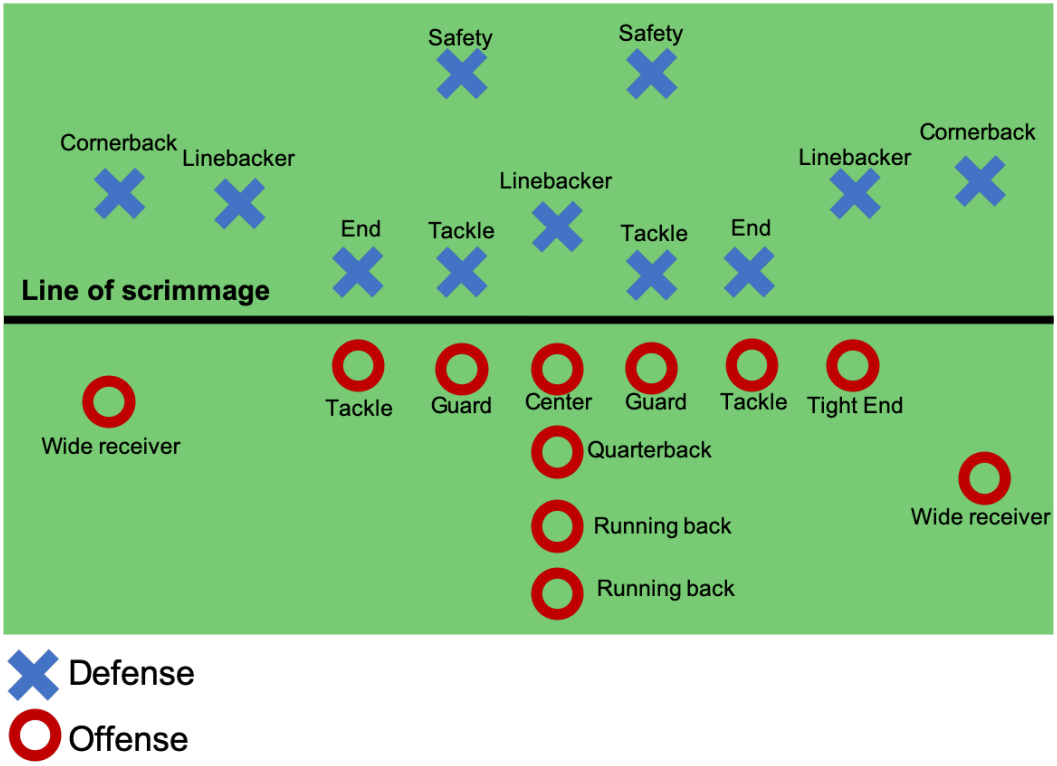

Fig. 3.1. The American football positions. Offensive players are designated as red circles and defensive players are blue Xs. The linemen are located on either side of the line of scrimmage. The non-linemen include all other positions on the field.

3.1.3 Quantifiable Brain Metabolites

Magnetic resonance spectroscopy (MRS) can be applied to study the metabolites profile of various tissues. In the healthy, mature brain, particular metabolites can be reliably quantified: *myo*-inositol (Ins), N-acetyl aspartate (tNAA), choline (tCho), creatine (tCr), and glutamate/glutamine (Glx). The concentrations of these metabolites remain stable in healthy subjects; however, in cases of disease, damage, and disorder, their levels can fluctuate.

Myo-Inositol

The primary functions of *myo*-inositol in the brain are osmoregulation (maintenance of osmotic pressure) and membrane synthesis [137]. Studies have reported increased Ins in cases of myelin damage [33, 43, 138]. This is attributed to the consequential increase in free Ins following tissue damage [43]. Increases in Ins have been quantified in various disease states, including Alzheimer's disease and multiple sclerosis [139,140]. Decreases have been observed in cases of hypoxia and stroke [137]. In addition, higher concentrations of Ins have been reported in white matter when compared with grey matter [22]. Studies on sports-related TBI have revelaed decreases in Ins [44].

N-Acetyl Aspartate

The resulting MRS signal from tNAA is the highest among the quantifiable metabolites. Levels of tNAA have been shown to increase in Canavan disease; however, most pathologies result in decreased tNAA [141]. Decreases in tNAA have been noted in brain injury, ischemia, cancer, multiple sclerosis, and Alzheimer's disease [45,142]. While significant research has been conducted on disease-related tNAA changes, not much is known regarding its specific functions. Baslow (2003) eludes to involvement of tNAA in the removal of intracellular water, thereby making it a

osmoregulator [143]. In cases of brain injury and subsequent edema or swelling, it would make sense for the tNAA signal to decrease. NAA has also been shown to mimic changes in adenosine triphosphate (ATP) - the hallmark energy molecule [144]. In addition, tNAA has been implicated as an important precursor for myelin synthesis [45]. However, further research must be completed to elucidate the exact function(s) of tNAA in the brain.

Choline

Choline is an integral component of neuronal membranes and is the precursor for acetylcholine (ACh) - an important neurotransmitter important for the maintenance of heart rate and breathing, as well and mood and memory [145]. Decreases in ACh have been implicated in Alzheimer's disease [146, 147]. Choline has been shown to increase following TBI [148]. This change is indicative of higher rates of membrane turnover, and resulting increases in free choline [110, 138, 149, 150]. However, choline has been reported to increase or decrease in studies on collision-sport athletes [44,149].

Creatine

Creatine is critically important for buffering and transporting energy-rich ATP in cells [151]. Levels of ATP are tightly regulated to promote cellular efficiency. Following TBI, some studies have reported decreased levels of tCr [44,144,152]. Interestingly, supplementation with creatine has been shown to improve outcomes [153]. However, these studies have been limited to animal models. In general, decreases in tCr may be linked to energy crises which can result from disease or damage. Given the importance of ATP maintenance, decreases in creatine could cause significant imbalance and resulting cellular dysfunction.

Glutamate and Glutamine

Glutamate is an excitatory neurotransmitter which can reach toxic levels when the brain is injured, known as glutamatergic toxicity. Glutamine is the precursor to glutamate; in MRS studies the two peaks are indistinguishable at 3 T, and thus, lumped together [154]. Glutamate acts as the precursor for gamma-amino butyric acid (GABA), a major inhibitory neurotransmitter. In an MRS study of subjects aged 24-68, glutamate and glutamine were shown to decrease with age [155]. Additionally, the two metabolites were highly correlated ($r = 0.052$; $p<0.01$). Glutamate has specific roles in neuronal differentiation, survival, and plasticity during brain development [154]. It is also important in the learning and the formation of memories. In the citric acid cycle (or Kreb's cycle), glutamate catalyzes the reaction of glutamine into α-ketoglutarate - an important constituent of glutathione [154]. Glutathione (GSH) is an endogenous antioxidant and is responsible for scavenging reactive oxygen species in the brain. Because ROS formation is triggered following TBI, any dysfunction in this process may result in diminished stores of GSH and persistent ROS. Levels of glx have been reported to decrease following TBI in both patients and collision-sport athletes [44, 47, 138]

3.1.4 Regions of Interest: Dorsolateral Prefrontal Cortex (DLPFC) and Primary Motor Cortex (M1)

The DLPFC's primary functions are related to working memory and executive functions, including decision making, impulse control, and strategic planning [156–158]. The DLPFC lies at the front of the brain in the frontal cortex. Functions and dysfunctions in this small region have primarily been determined from lesional, electrophysiological, and neuroimaging studies. Functional MRI examination of high school football athletes revealed decreased activation in this region [120]. Because the anatomy is located at the front of the head, it could be postulated that repetitive impacts to this region may result in cumulative damage and/or neurophysiological

dysfunction. In fact, some studies have reported neurometabolic changes in this brain region [44, 47, 138].

The primary function of M1 is motor planning and control. However, recent research has highlighted its roles in motor learning and memory as it is interconnected to regions such as the hippocampus and thalamus [159,160]. Patients with amyotropic lateral sclerosis, a motor disease, showed decreased levels of tNAA and increased tCho in M1 [161]. Additionally, patients with mild cognitive impairment had lower tNAA, higher tCho, and showed comparatively poorer performance in gaiting tasks [162]. Interestingly, neurometabolites have been reported to fluctuate in this brain region following TBI. Henry et al. (2010) reported decreased Glx and tNAA in M1 in concussed athletes [163]. Poole et al. (2014) reported decreased Glx and tCr in high school football athletes over the course of the season [44].

3.1.5 Motivation

Due to the high incidence of sports-related concussions and the lack of changes to play behaviors, it is important to elucidate the influence of positional-specific HAEs on neurometabolic outcomes. Research has shown 1) neurometabolic changes during the football season and 2) position-specific differences in HAEs. Here, the ultimate goal is to better understand how variations in HAEs by position may influence neurophysiological outcomes in youth collision-sport athletes.

3.2 Methods

3.2.1 Participants

Seventy-two (72) male, high school football players participated in this study (ages: 14-18 years, mean = 16.1). Subjects were recruited from three local high schools and imaged five times over the course of one football season. Due to lack of participation at all sessions, some subjects were excluded from analysis. After post-

processing and data quality checks, the total number of subjects included in statistical analyses was 55, equating to 275 observations. Subjects were further classified based on their primary position (1 = linemen, 2 = non-linemen; $n_{linemen}$ = 20; $n_{nonlinemen}$ = 35). 40% (22/55) of subjects reported a history of concussion (HoC).

3.2.2 Imaging Timecourse

Subjects were imaged five times over the course of the season: once before commencement of contact practice (*Pre*), twice during the competition season (*In1* and *In2*), and twice following the competition season (*Post1*, and *Post2*). Note that *Post2* data were not used in statistical analysis due to transition to a new MRI scanner and lack of sufficient evidence to compare spectroscopic data across scanner models.

3.2.3 Head Acceleration Event Monitoring

Head acceleration events (HAEs) were monitored for every subject at all practices and games using the X2 Patch Biosystems Sensor (X2 Biosystems; Seattle, WA). The sensor was attached behind the ear using an adhesive patch which was applied after cleansing the area with an alcohol prep pad. After each practice and game, data from the sensors were downloaded to the Head Impact Monitoring System software (X2 Biosystems; Seattle, WA). The software provided Peak Linear Acceleration (PLA) and Peak Rotational Acceleration (PRA) for each HAE (>10g) and HAEs <20 g were discarded [164]. Due to inherent limitations of the gyroscope, PRA was not included in any statistical analyses.

3.2.4 MRS Protocol

All data (except *Post2*) were collected at the Purdue University MRI Facility (West Lafayette, IN). A 3 T General Electric (GE) Signa HDx (Waukesha, WI) was used in combination with a 16-channel brain array coil (Nova Medical; Wilmington,

MA). Data were collected using a single voxel PRESS sequence (TE = 30 ms, TR = 1500 ms, averages = 128, FOV = 20 mm^3). For accurate image registration and segmentation, a high-resolution T_1 scan was performed with a 3D SPoiled Gradient Recalled echo (SPGR) sequence (TE = 1.976 ms, TR = 5.7 ms, averages = 128, 1 mm isotropic resolution). PRESS voxels were placed in the dorsolateral prefrontal cortex (DLPFC) and the primary motor cortex (M1) as demonstrated in Bari et al. 2018 [47]. These regions were selected based on 1) the function and location of the specific brain region, and 2) previous research showing significant alterations following TBI (see section 3.1.4). To better match voxel placement across sessions, operators were instructed to use the reconstructed voxel placement from *Pre* sessions. Because multiple operators conducted scans, voxel placement varied at each session. Therefore, any voxels that achieved less than 30% overlap with preseason placement were discarded.

3.2.5 MRS Post-Processing

MRS data were post-processed using a custom Matlab code (courtesy Sumra Bari) [47]. Metabolites of interest included N-acetyl aspartate (NAA), myo-inositol (Ins), total choline (tCho), total creatine (tCr), and glutamate/glutamine (Glx). Quantification of these metabolites has been proven robust in previous studies. TARQUIN, a spectral fitting program, was used to fit the metabolites of interest using tissue water as a reference [165]. TARQUIN comes equipped with brain basis sets which aid in accurate spectral fitting. However, corrections must be made to account for partial volume effects and metabolite and water T_1 and T_2. AFNI, a brain segmentation tool, was first used to correct for partial volumes of white matter, grey matter, and CSF [166]. Next, FSL, a neuroimaging analysis tool, was used to correct for metabolite and water T_1 and T_2 following Poole et al. (2014) [44]. Data were reported as relative concentrations to tissue water. Spectral data were included in statistical analyses if they met the following criteria: 1) achieved Cramer-Rao lower

bounds <25% standard deviation, 2) achieved >30% overlap with preseason voxel placement, and 3) if data were present for all four imaging sessions (*Pre*, *In1*, *In2*, and *Post1*). This resulted in 28 DLPFC subjects and 18 M1 subjects; this large reduction in sample size was primarily due to missing imaging sessions leading to incomplete subject data sets. To fill in the missing sessions, multiple imputations was performed (see section 3.2.7).

3.2.6 HAE Post-Processing

Various HAE values were calculated: total hits per session ($tHits_{session}$), cumulative PLA per player ($cPLA$), cumulative PLA per session ($cPLA_{session}$) total hits per player ($tHits$), average PLA per player ($aPLA$), total hits greater than 50g per player ($tHits_{50g}$), average PLA greater than 50g and 60g per player ($aPLA_{50g}$), cumulative PLA greater than 50g per player ($cPLA_{50g}$), and the ratio of hits greater than 50g and 60g per player to total hits per player ($tHits_{50g}$:$tHits$).

Total hits ($tHits$) and $tHits_{50}$ were calculated by counting all HAEs >20g and >50g for i^{th} players between corresponding j^{th} sessions (first contact practice-*In1*, *In1-In2*, *In2-Post1*).

$$tHits = \sum_{k=1}^{N_j} Hits_{k,i} \tag{3.1}$$

and

$$tHits_{50g} = \sum Hits_{k,i,>50g} \tag{3.2}$$

Total hits per session were calculated using the dates of imaging sessions (*In1, In2, Post1*). Specifically, hits between the first (*In1*) and second (*In2*) imaging sessions and hits between the second (*In2*) and third (*Post1*) imaging sessions were counted.

Cumulative PLA was calculated by summing all PLA events for each i^{th} player between corresponding j^{th} sessions (first contact practice-*In1*, *In1-In2*, *In1-Post1*).

$$cPLA_{ij} = \sum_{k=1}^{N_j} PLA_{k,i} \tag{3.3}$$

This equation was also used to sum PLA values greater than 50g.

$$cPLA_{ij,50g} = \sum_{k=1}^{N_j} PLA_{k,i,50g} \tag{3.4}$$

Cumulative PLA per session was calculated using the dates of imaging sessions (*In1, In2, Post1*). Specifically, hits between the first (*In1*) and second (*In2*) imaging sessions and hits between the first (*In1*) and third (*Post1*) imaging sessions were counted.

The average PLA (aPLA) was calculated by dividing cPLA by tHits for each i^{th} player between corresponding j^{th} sessions (first contact practice-*In1*, *In1-In2*, *In1-Post1*). This formula was also used to calculate the average number of hits greater than 50g.

$$aPLA_{ij} = \frac{cPLA_{ij}}{tHits_{ij}} \tag{3.5}$$

and

$$aPLA_{ij,50g} = \frac{cPLA_{ij,50g}}{tHits_{ij,50g}} \tag{3.6}$$

Lastly, the ratio of tHits_{50g} and tHits was determined using

$$\%Hits > 50g = \frac{tHits_{50g}}{tHits} x100 \tag{3.7}$$

An identical equation was used to determine the percentage of hits greater than 60g.

3.2.7 Statistical Analysis

All statistical analyses were conducted in STATA [167]. Due to the large number of missing sessions, multiple imputations were conducted and the means of 50 im-

putations were reported [168]. Combining the imputed values with preexisting data resulted in 51 DLPFC subjects and 32 M1 subjects. It should be noted that multiple imputations were only conducted if 1) the subject was missing *one* imaging session, or 2) *one* imaging session was thrown due to poor quality (i.e. overlap >30%).

First, metabolite concentrations were checked for normality and equal variances using Shapiro-Wilks test for normality and Bartlett's test for equal variances [169, 170]. All reported p-values were less than 0.05, indicating concentrations were not normally distributed and did not have equal variances. For this reason, all raw metabolite data (i.e. non-transformed) were analyzed using nonparametric analyses. Comparisons of two groups were completed using t-test since sample size was greater than 20 for both DLPFC (51) and M1 (32) subject pools. Next, the effect of age on metabolite concentrations at *Pre* were investigated using the Kruskal Wallis nonparametric test followed by Bonferroni multiple comparisons correction [171, 172]. No significant age-related differences were discovered in DLPFC or M1 ($p < 0.05$). Next, interactions between session and HoC as well as session and position were tested. No significant interactions were found between HoC and session or position and session for DLPFC and M1 metabolites.

Following the above analyses, session-dependent changes in DLPFC and M1 metabolites were analyzed using the Friedman test - a nonparametric version of a one-way repeated measures ANOVA. Friedman-reported p-values less than 0.05 were further analyzed using the Wilcoxon ranksum test for pairwise comparisons and the false discovery rate (FDR) multiple comparisons correction [47, 173, 174]. Pairwise comparisons reporting a p-value less than 0.05 were considered statistically significant.

Additionally, position-dependent effects on DLPFC metabolites at each session were studied using standard t-test to compare position one (linemen; $n = 20$) and position two (non-linemen; $n = 31$). Reported p-values less than 0.05 were considered statistically significant. Position-dependent effects across all sessions were analyzed using the Friedman test, followed by the Wilcoxon ranksum test with FDR correction. Position-dependent effects on M1 metabolites at each session were compared

independently using Wilcoxon Ranksum test since the sample size for linemen was less than 20 in this group (n = 11). Again, position-dependent effects across all sessions were analyzed using the Friedman test, followed by the Wilcoxon ranksum test with FDR correction.

Next, position-specific variations in head acceleration events (HAEs) were investigated using a Wilcoxon ranksum test. M1 and DLPFC subjects were combined for these analyses resulting in 20 linemen and 35 non-linemen (n = 55). Reported results with p-values less than 0.05 were considered statistically significant.

Following session-wise and pairwise analyses, metabolite data were normalized sing equation 3.8. Because results from HAE analyses showed significant position-dependent changes in end-of-season, or cumulative, hits, the normalization was conducted between *Pre* and *Post1* sessions. Figure 3.1 depicts this method further.

$$NormalizedMetabolite = \frac{\Delta Metabolite_{pre-session}}{[Metabolite]_{pre}} \tag{3.8}$$

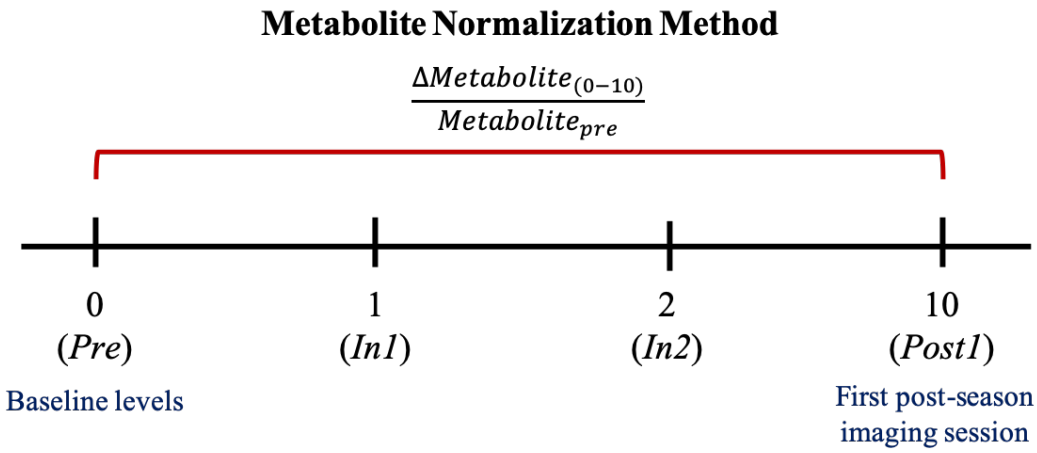

Fig. 3.2. Metabolites were normalized by subtracting the *Post*-season metabolite concentration from the *Pre*-season metabolite concentration for each subject. The difference was then divided over the same *Pre*season value.

Normalized metabolites were regressed against end-of-season hits variables to determine significant associations between changes in metabolic concentrations and HAEs

(*cPLA*, *tHits*, *aPLA*, $cPLA_{50g}$, $tHits_{50g}$, $aPLA_{50g}$, and $tHits_{50g}$:*tHits*) Only *In1*, *In2*, and *Post* sessions were used for regression analysis. Cook's Difference was used to determine the significance of potential outliers on the regression models [175]. Using this method, no outliers were shown to significantly affect the outcome of the regressions (Cook's D <5). Therefore, no values were removed for regression analyses.

Lastly, metabolite levels were compared between high school non-collision sport controls and high school athletes. Controls (n = 14; mean age = 16.2) were imaged during a previous season but the same imaging protocol and scanner model was used [47]. Controls were also age- and gender-matched. These non-collision sport athletes underwent two imaging sessions - test and re-test. There were no significant differences between test and retest metabolites in control athletes (Wilcoxon p-value >0.05). Wilcoxon ranksum test was then used to compare metabolite levels between collision and non-collision athletes. The test session in control athletes was compared to *Pre* in football athletes and re-test was compared to *Post*. Any p-values less than 0.05 were reported as significant.

3.3 Results

3.3.1 DLPFC Changes by Session

Friedman analysis of DLPFC metabolites by session yielded a significant finding in inositol levels by session (p-value = 0.0020; n = 51). Inositol was significantly lower at *In1* (p-value = 0.0239), *In2* (p-value = 0.0012) and *Post* (p-value = 0.0001) compared to *Pre*/baseline (Figure 3.3). Box plots are displayed as follows: the middle line on the box represents the median, the lower and upper lines on the box represent the 25^th and 75^th percentiles, respectively; outliers are represented as dots.

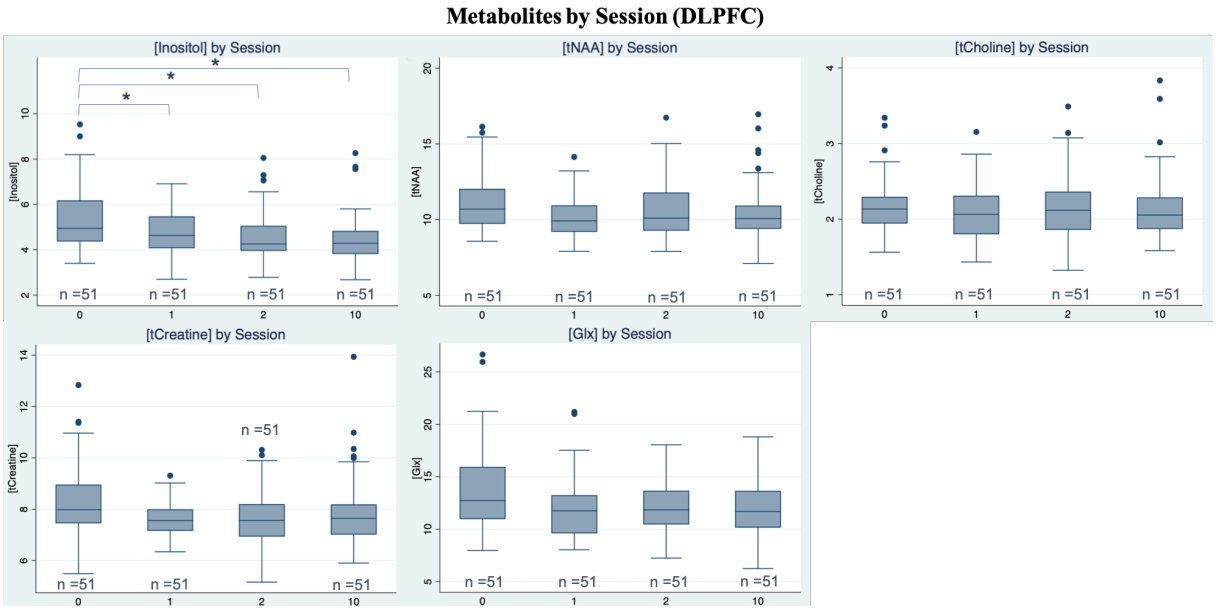

Fig. 3.3. Metabolic changes in DLPFC in male, high school athletes over a season of American football (n = 51 for all sessions). Inositol significantly decreased between *Pre-In2* and *Pre-Post* (* indicates FDR-corrected p-value <0.05)

3.3.2 DLPFC Metabolic Changes by Position

Non-linemen (red) exhibited significant changes in inositol by session (p-value = 0.0199). Specifically, inositol was significantly lower between *Pre* and *In1* (p-value = 0.0276), *Pre* and *In2* (p-value = 0.0062), as well as *Pre* and *Post* (p-value = 0.0002) (Figure 3.4). In addition, inositol was significantly lower in non-linemen (red; n = 31) versus linemen (blue; n = 20) at *Post* (p-value = 0.0193). Lastly, tNAA was significantly lower in non-linemen (red; n = 31) compared to linemen (blue; n = 20) at *In1* (p-value = 0.0049).

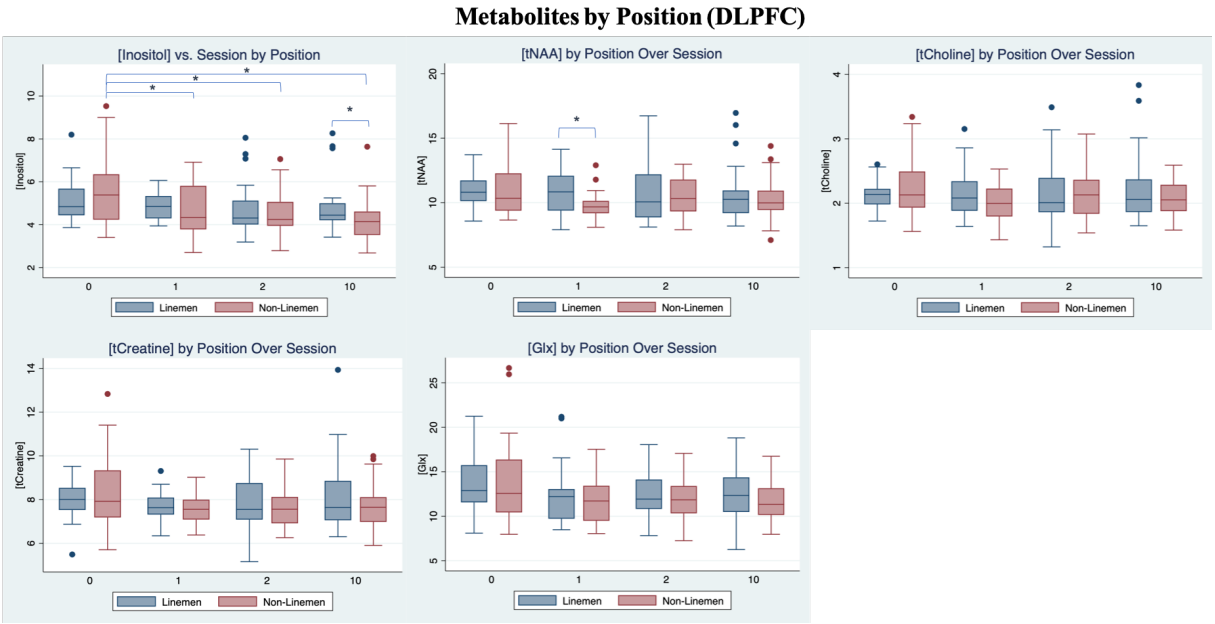

Fig. 3.4. Analysis of DLPFC metabolites by position over sessions revealed significant differences in inositol by session. Non-linemen displayed significantly lower Ins at *In1*, *In2*, and *Post* compared to *Pre*. Inositol was significantly lower in non-linemen at *Post1* and tNAA was significantly lower in non-linemen at *In1* (0 = *Pre*, 1 = *In1*, 2 = *In2*, 10 = *Post*).

3.3.3 M1 Changes by Session

Friedman analysis of metabolite by session in M1 yielded revealed significant changes in all metabolites by session (n = 32). Inositol was significantly lower at *In1* (p-value = 0.0005) , *In2* (p-value = 0.0001), and *Post* (p-value = 0.0011) compared to *Pre*/baseline (Friedman overall p-value = 0.0001). Total choline was significantly lower at *In1* (p-value = 0.0001), *In2* (p-value = 0.0011), and *Post* (p-value = 0.0106) compared to *Pre*-season levels (Friedman overall p-value <0.0001). Total creatine was significantly lower at *In1* (p-value = 0.0008), *In2* (p-value = 0.0005), and *Post* (p-value = 0.0238) compared with baseline (*Pre*) (Friedman overall p-value = 0.0011). In addition, tCr was significantly higher at *Post* compared to *In2* (p-value = 0.0447).

Lastly, glutamate/glutamine (Glx) was significantly lower at *In1* (p-value = 0.0187) and *In2* (p-value = 0.0009) compared with *Pre* (Friedman overall p-value = 0.0042). Box plots are shown in Figure 3.5.

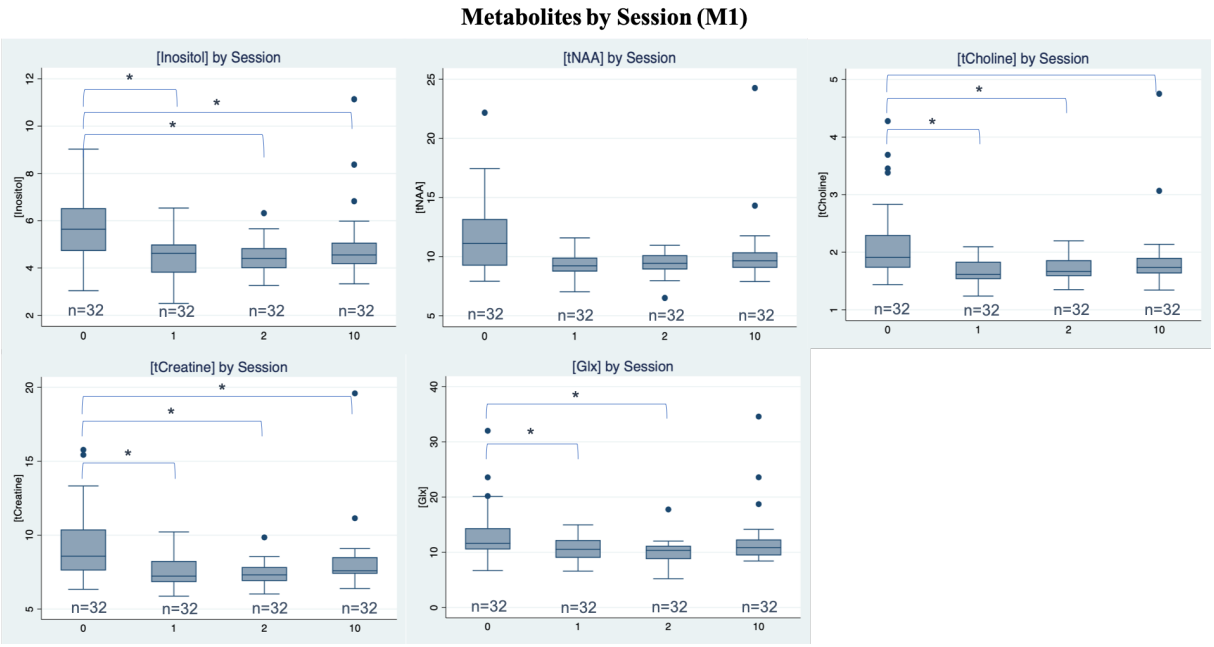

Fig. 3.5. Metabolic changes in M1 in male, high school athletes over a season of American football (n = 32 for all sessions). All metabolites, apart from tNAA, exhibited significant decreases from *Pre*-season levels (* indicates p-value <0.05).

Further analysis of metabolites by position over all sessions revealed significant differences in all metabolites for non-linemen (n = 21) and significant differences in Ins and tCho for linemen (Figure 3.6). Inositol was significantly lower in non-linemen at *In1* (p-value = 0.0010), *In2* (p-value = 0.0019), and *Post* (p-value = 0.0173) compared to *Pre* (Friedman overall p-value = 0.0010). Choline was significantly lower in non-linemen (Friedman overall p-value = 0.0006) at *In1* (p-value = 0.0025) and *In2* (p-value = 0.0419) versus *Pre*. Non-linemen also exhibited significantly lower tCho at *In1* compared to *Post* (p-value = 0.0091). In addition, choline was significantly lower in linemen at *In1* (p-value = 0.0043), *In2* (p-value = 0.0043) and *Post* (p-

value = 0.0043) compared to *Pre* (Friedman overall p-value = 0.0025). Creatine was significantly lower at *In1* (p-value = 0.0067) and *In2* (p-value = 0.0084) compared to *Pre* (Friedman overall p-value = 0.0036). Creatine was also significantly lower at *In1* versus *Post* (p-value = 0.0475). Lastly, glx was significantly lower in non-linemen at *In2* compared to *Pre* (p-value = 0.0132; overall Friedman p-value = 0.0094).

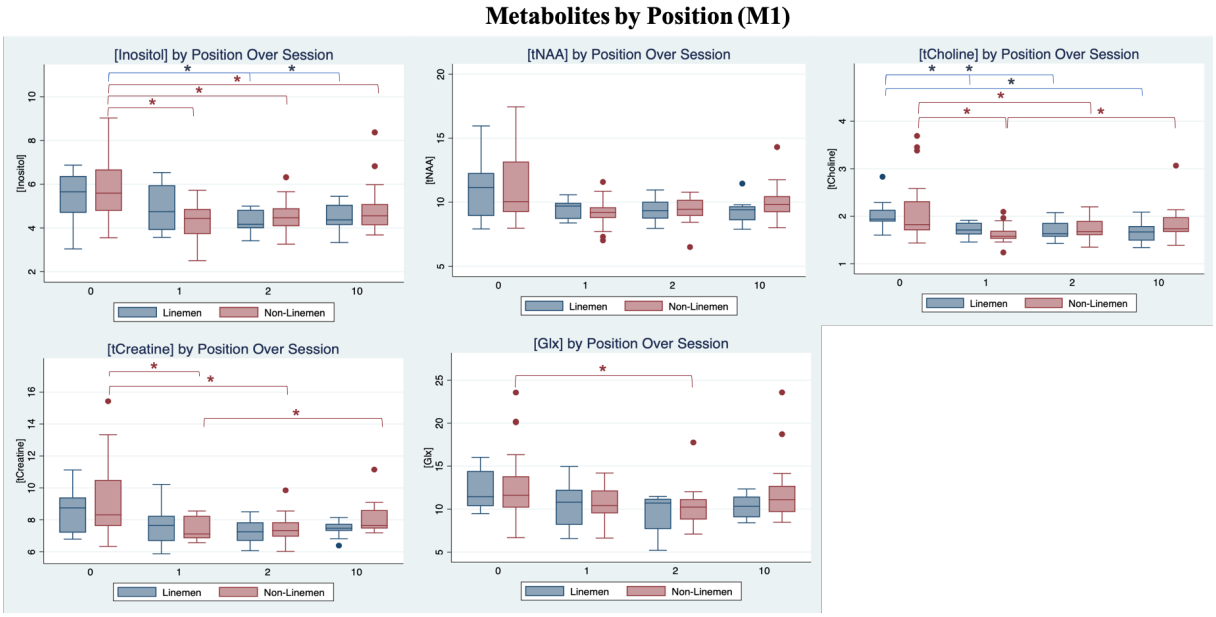

Fig. 3.6. Analysis of M1 metabolites by position over all sessions. Inositol was significantly lower in non-linemen at *In1*, *In2*, and *Post* compared to *Pre*. Ins was signficantly lower in linemen at *In2* and *Post* compared to *Pre*. tCho was significantly lower in non-linemen at *In1* and *In2*, recovering slightly at *Post1*. tCho was significantly lower in linemen at *In1*, *In2*, and *Post* compared to *Pre*. tCr was significantly lower in non-linemen at *In1* and *In2* compared to *Pre*, and recovering at *Post1*. Glx was significantly lower in non-linemen at *In2* compared to *Pre* (* designates p-value <0.05).

3.3.4 HAE Variations by Position

Analysis of the interactions between position and different hit metrics revealed that linemen ("1"; n = 20) accumulated more hits over the course of season, but non-linemen ("2"; n = 35) (running backs, defensive backs, etc.) sustained greater average impacts (e.h. aPLA$_5$0g) (Figure 3.7). Specifically, linemen had significantly higher levels of *tHits* (p-value = 0.0003) and *cPLA* (p-value = 0.0007) compared to non-linemen. Non-linemen had significantly higher *aPLA* (p-value = 0.0191) compared to linemen.

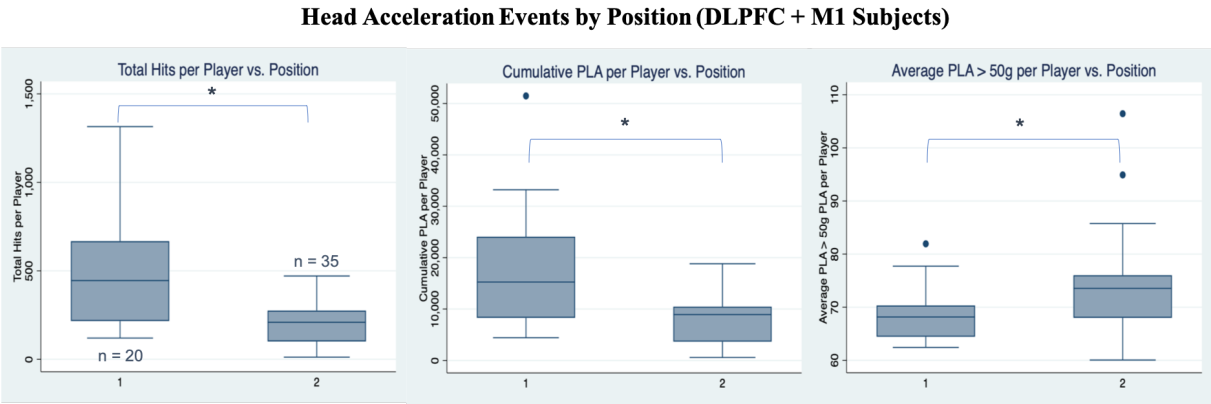

Fig. 3.7. Analysis of hit metrics by position. Position 1 = linemen and position 2 = non-linemen. All reported plots were statistically significant (* indicates a p-value <0.05).

3.3.5 Linear Regression Analyses: Metabolite-HAE Interactions

DLPFC Regression Analyses

Normalized DLPFC metabolites were regressed against hit metrics detailed in Section 3.2.6. Normality and equal variances were confirmed before regression analysis and only metabolites which were normally distributed were further analyzed. Cumulative metrics, such as *tHits* and *cPLA*, were regressed against metabolite values at

Post1. Coefficients were reported as standardized metabolite and hit values to reveal the true unit change. Normalized Glx ($\Delta Glx/Glx_{pre}$) showed a negative association with *aPLA* (coefficient = -0.2957, p = 0.037) (Figure 3.7).

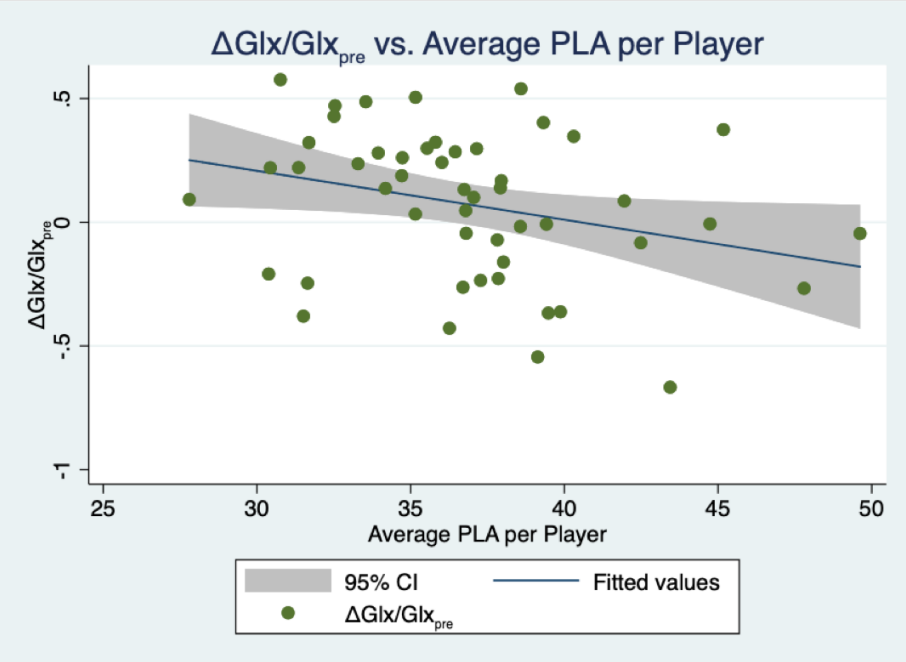

Fig. 3.8. **DLPFC**: Linear regression of $\Delta Glx/Glx_{pre}$ and *aPLA*. Normalized Glx decreased with increasing average PLA per player. The shaded region represents the 95% confidence interval (coefficient = -0.2957; $p = 0.037$).

3.3.6 Influence of Position on Metabolite-HAE Interactions

Further analysis of metabolite-HAE associations were conducted by position for both DLPFC and M1.

DLPFC

First, normalized Glx was analyzed by position (linemen vs. non-linemen). Regressions were run against all cumulative HAEs to reveal potential hidden effects of

position on the metabolite-HAE regressions. Normalized Glx concentrations in non-linemen showed significant negative associations between $aPLA$ (coefficient = -0.3968; p-value = 0.022) and $tHits_{50g}$ (coefficient = -0.3681; p-value = 0.037) (Figure 3.8).

Metabolite	Variable	Position	Trend	Coefficient	P-value
$\Delta Glx/Glx_{pre}$	Avg. PLA/Player	Linemen	Decrease	-0.0663	0.833
$\Delta Glx/Glx_{pre}$	Avg. PLA/Player	Nonlinemen	Decrease	-0.3968	**0.022**
$\Delta Glx/Glx_{pre}$	$tHits_{50g}$	Linemen	Decrease	-0.0499	0.864
$\Delta Glx/Glx_{pre}$	$tHits_{50g}$	Nonlinemen	Decrease	-0.3681	**0.037**

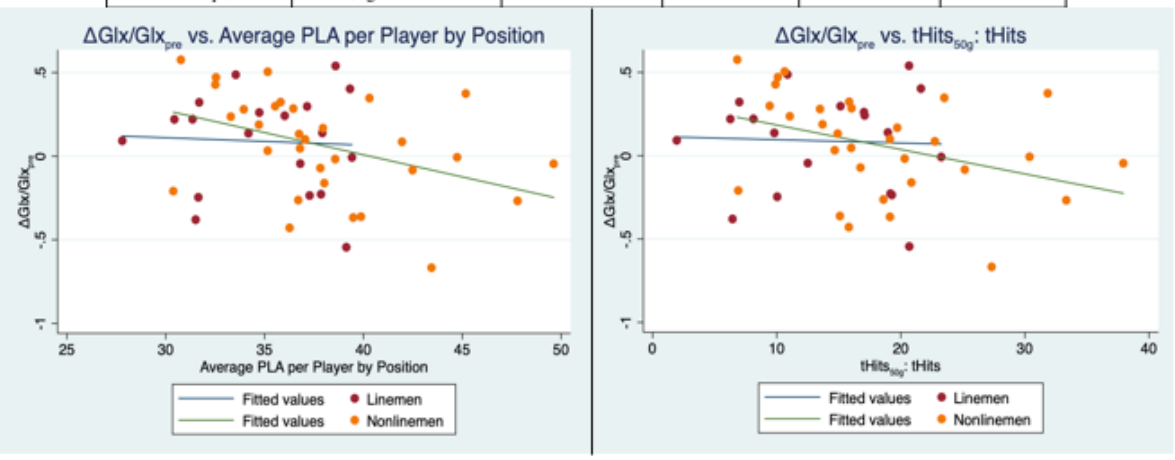

Fig. 3.9. Normalized Glx was regressed against HAEs by position. There was a significant association between $\Delta Glx/Glx_{pre}$ and aPLA as well as $\Delta Glx/Glx_{pre}$ and $tHits_{50g}$.

When broken up by position (i.e. linemen vs. non-linemen), only the non-linemen a significant trend of decreasing Glx with increasing aPLA (coefficient = -0.3968, p = 0.022). While an overall trend in $\%tHits_(50g)$ was not observed, position-specific analysis revealed a significant trend of decreasing Glx with increased $\%tHits_(50g)$ in non-linemen (coefficient = -0.3681, p = 0.037) (Figure 3.9).

M1

In M1, there was an overall trend of decreasing normalized Glx with increasing percentage of hits exceeding 60g (coefficient = -0.4317; p = 0.0172). Further position-specific analyses were conducted to reveal possible interactions when positions were analyzed separately (linemen vs. non-linemen). Normalized tNAA was significantly associated with *tHits* in linemen (coefficient = 0.5923; *p*-value = 0.040). In particular, as *tHits* increased, normalized tNAA also increased (Figure 3.10).

Metabolite	Variable	Position	Trend	Coefficient	P-value
$\Delta tNAA/tNAA_{pre}$	tHits	Linemen	Increase	0.5923	**0.040**
$\Delta tNAA/tNAA_{pre}$	tHits	Nonlinemen	Decrease	-0.2958	0.410

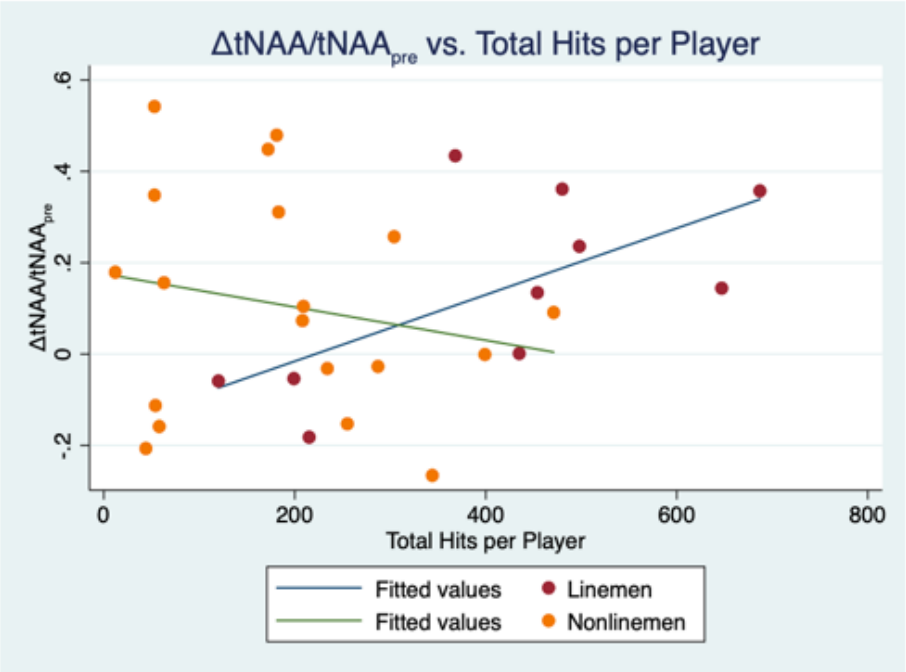

Fig. 3.10. Normalized tNAA showed a significant positive association with tHits in linemen only.

3.3.7 Metabolite Comparisons Between Controls and High School Football Athletes

DLPFC

Football athletes exhibited significantly higher levels of Ins (p-value <0.0001), tNAA (p-value = 0.0256) tCho (p-value = 0.0010), tCr (p-value = 0.0017), and Glx (p-value = 0.0173) at *Pre* compared to test in controls. In addition, Ins (p-value = 0.0089), tCho (p-value = 0.0043), and tCr (p-value = 0.0153) were also significantly elevated at *Post* compared to re-test in controls (Figure 3.11).

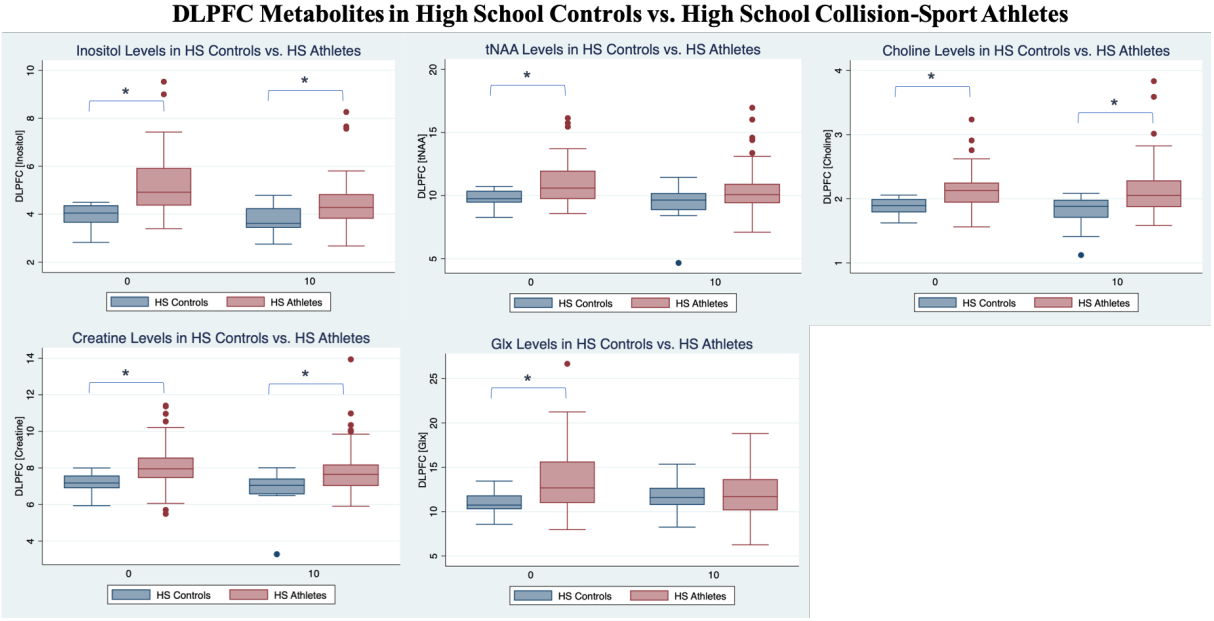

Fig. 3.11. Comparison of DLPFC metabolites in non-collision sport control athletes with football athletes. Ins, tNAA, tCho, tCr, and Glx were all significantly elevated in football athletes at *Pre*. Ins, tCho, and tCr were also significantly elevated in football athletes at *Post* (0 = *Pre*/test; 10 = *Post*re-test) (* p-value <0.05).

M1

Again, football athletes exhibited significantly higher levels of metabolites compared to controls. Specifically, Ins (p-value = 0.0022), tNAA (p-value = 0.0241), tCho (p-value = 0.0033), and tCr (p-value = 0.0018) were significantly higher at *Pre* compare to test in controls. At *Post*, football athletes had significantly higher levels of tCr compared to re-test in controls (p-value = 0.0094) (Figure 3.12).

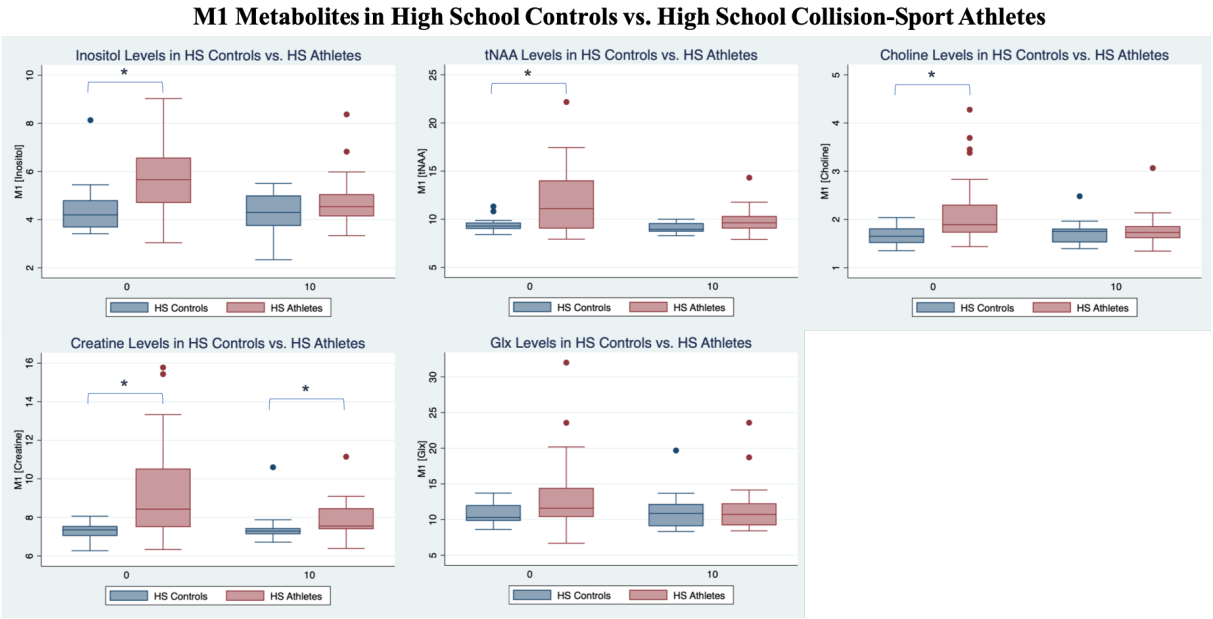

Fig. 3.12. Comparison of M1 metabolites in non-collision sport control athletes with football athletes. Ins, tNAA, tCho, and tCr were all significantly elevated in football athletes at *Pre*. Only tCr was significantly elevated in football athletes at *Post* (0 = *Pre*/test; 10 = *Post*re-test) (* p-value <0.05).

3.4 Discussion

Due to the high incidence of sports-related concussion in youth athletes and the potential for long-term morbidity, it is critical to evaluate how play behavior affects brain homeostasis. In the presented study, 55 male, high school football athletes were imaged at four time points and monitored for HAEs at each practice and game. Imaging data were collected and post-processed to analyze associations between neurometabolic changes and HAEs based on primary position (linemen vs. non-linemen). Significant associations between neurometabolites, HAEs, and position were observed.

3.4.1 DLPFC Neurometabolic Changes: Inositol

In the DLPFC, inositol (Ins) was observed to significantly decrease from baseline (*Pre*) at *In1*, *In2*, and *Post*. Myo-inositol is involved in the synthesis of the phospholipid membrane surrounding axons and is a potential marker of membrane turnover [44, 138]. It is also an astrocytic marker and osmolyte - meaning it is important in maintaining cell integrity via maintenance of fluids. Commonly in the literature, myo-inositol has been reported to increase following TBI [43, 138, 149]. However, the time of imaging and ROI become important when considering these findings, and most studies look at the acute phase of injury. Interestingly, one study on patients involved in motor vehicle accidents reported fluctuating Ins:tCr between two weeks and 10 months [176]. Notably, Ins:tCr was significantly lower in patients imaged 2-3 weeks post-TBI. Poole et al. (2014) found decreases in DLPFC inositol in collision-sport athletes at one, two, and three months following baseline scans [44]. Xu et al. (2012) also found decreased inositol in rats with controlled closed-head injuries [177]. These changes may reflect an energy crisis and hypo-osmolarity from swelling, where inositol is metabolized to generate energy for repair mechanisms [177]. It could be that cumulative injury between *Pre* and *In1*, *In2*, and *Post* results in the observed Ins decrease. If true, this could be indicative of localized swelling and energy crises - markers of significant tissue damage.

3.4.2 M1 Neurometabolic Changes: Ins, tNAA, tCho, tCr, Glx

In M1, all metabolites, apart from tNAA, were found to significantly decrease from preseason levels. Inositol (Ins), choline (tCho), creatine (tCr), and glutamte/glutamine (Glx) were found to significantly decrease between *Pre* and *In1* as well as *Pre* and *In2*. Ins, tCho, and tCr were also noted to significantly decrease between *Pre* and *Post*. These changes reflect significant neurometabolic dysfunction and crises. Reasons for the observed decrease in Ins were discussed above in section 3.4.1.

Previous research has reported significant decreases in tNAA following TBI [46, 144, 148]. In addition, tNAA reductions are more pronounced in as injury severity increases [144]. NAA is synthesized in the mitochondria and shuttled down the axon. It has been implicated as a marker of neuronal density and integrity, and has been shown to mimic changes in adenosine triphosphate (ATP; the primary energy source in cells) [144]. It has also been to shown to be important for the removal of intracellular water and thus, osmoregulation [143]. tNAA has also been implicated as an important precursor for myelin synthesis [45]. For these reasons, decreases in tNAA may be reflective of decreased energy sources (i.e. ATP), dysfunctional water removal, increased myelin synthesis requirements, and/or axonal swelling.

Choline, a neuronal membrane marker, has been shown to increase following TBI - indicative of a higher rate of membrane turnover [108, 138, 149, 150]. However, some studies have reported significant decreases in tCho following TBI which could be representative of tissue damage [44, 178]. Choline is a precursor for acetylcholine (ACh), an important neurotransmitter for learning and memory. Decreases in ACh neurotransmission pathways have been associated with Alzheimer's disease [146]. Decreases in tCho may lead to decreased ACh neurotransmission and ultimately impairment in memory tasks. In fact, cognitive impairment *has* been reported in some studies on high school football athletes [120, 179, 180]. Together, a decrease in tCho could be indicative of tissue damage and swelling.

In the brain, creatine is a marker of energy status. In many TBI studies, tCr remains stable and is therefore used as an internal reference [47, 138]. However, tCr was significantly decreased in the presented results. Other studies have also reported this decrease [44, 144, 152]. This observation 1) further questions the use of tCr as an internal reference, and 2) suggests a state of energy crisis and impaired ATP buffering.

In addition to the above changes, Glx also significantly decreased between *Pre* and *In2*. Glx includes both glutamate and glutamine, combined. When glutamine undergoes a enzymatic reaction with glutaminase, glutamate is producced [154]. Glutamate is the precursor to the inhibitory neurotransmitter, gamma-amino butyric acid (GABA). On its own, glutamate is a major excitatory neurotransmitter and has important roles in synaptic plasticity, learning and memory pathways, neuronal differentiation and survival during brain development, and cytoskeletal maintenance [154]. In addition, glutamine can be converted to α-ketoglutarate via glutamate; α-ketoglutarate is an intergral component of glutathione (GSH), an important ROS scavenger. MRS analyses in TBI studies have also revealed decreased levels of Glx [44, 47, 152]. Together, decreased Glx may be linked with impaired neurotransmission, decreased synthesis of GSH and persistence of ROS, memory deficits, and dysfunctional neuronal differentiation - which is especially important in developing youths.

In general, metabolic changes following TBI are more frequently observed in M1, consistent with our findings. Decreased levels of these metabolites in both DLPFC and M1 suggest significant tissue damage, initiation of repair, swelling, and energy crises.

3.4.3 Position-Specific Effects

Based on the presented results, linemen accumulated more hits (tHits and cPLA) while non-linemen had a higher average PLA when counting hits greater than 50g ($aPLA_{50g}$) (Figure 3.7). Linemen are positioned at the line of scrimmage and defend

or offend other players and linemen, respectively. During each play sequence, linemen make contact with another player. Therefore, the larger number of HAEs in linemen makes intuitive sense. Non-linemen (e.g. running backs, defensive backs, and kickers) withstand fewer contacts, but these contacts are typically much larger in force - hence, the higher aPLA. Again, the results align with this observation.

An analysis of position-dependent metabolite changes across sessions was also performed. Inositol was significantly lower in non-linemen at *In1*, *In2*, and *Post* compare to *Pre*-season levels. Additionally, Ins was lower in non-linemen at *Post* and tNAA was lower in non-linemen at *In1* compared to linemen. This result may elude that non-linemen, who accrue fewer but higher magnitude hits, may be particularly susceptible to neurometabolic changes. Analysis of M1 metabolites by position revealed significantly lower levels of Ins, tCho, tCr, and Glx in non-linemen at *In1*, *In2*, and/or *Post*. Linemen also exhibited significantly lower Ins and tCho at *In1*, *In2*, and/or *Post*. However, again, it is the non-linemen group that is dominating the significant observations. In the M1 cohort, the lack of additional observations could be due to a small linemen sample size (n = 11).

3.4.4 Interactions Between Metabolites, HAEs, and Position

Regression analysis of metabolite changes against various HAEs revealed significant results. In DLFPC, normalized Glx significantly decreased with increasing aPLA in non-linemen only (Figure 3.8). That is, players with higher magnitude hits exhibited significantly more pronounced decreases in Glx. Again, this could be the result of higher magnitude hits dominating changes in neurometabolic concentrations.

Significant interactions were also observed in M1. Normalized Glx was found to negatively correlate with the percentage of tHits_{60g}. In other words, Glx decreased with an increasing percentage of hits greater than 60g. This makes sense intuitively, given that larger decreases in metabolites are observed with more severe injury. When broken down by position, changes in Glx were no longer significant - indicating that

decreases in Glx are not position-specific. In general, larger high magnitude hit counts may be predictive of significant decreases in Glx. tNAA was also observed to change; here, tNAA increased with increasing $tHits$ in linemen, specifically. This is an interesting observation and may be the result of 1) a small sample size, or 2) repair mechanisms. $tHits$ were higher in linemen compared to non-linemen, but non-linemen exhibited higher magnitude hits. It is plausible that frequent, low-magnitude hits experienced by linemen could initiate repair mechanisms in the brain. Given that tNAA has been implicated in membrane synthesis, levels of this metabolite may increase with minor tissue damage to repair the damaged regions.

These finding suggest that while neurometabolic changes occur in players of both positions, the mechanism of injury and resultant neurometabolic changes may vary. In both brain regions, Glx decreased with increasing higher magnitude hits. Specifically, non-linemen exhibited significant decreases in Glx in the DLPFC but the trend was observed not position-specific in M1. In addition, M1 also exhibited position-specific changes in tNAA. These changes could indicate that non-linemen are more susceptible to changes in neurometabolic concentration between *Pre* and *Post1*. This could be the result of higher magnitude hits or tackle style. Observations are likely due to a combination of effects (i.e. location, angle, severity, etc.) and resulting damage may be unique for every TBI case.

3.4.5 Comparison of Metabolites in Non-Collision Control Athletes versus Football Athletes

Metabolites were significantly elevated in football athletes compared to controls. This trend was observed in both DLPFC and M1, with the majority of differences occurring at *Pre*-season. One explanation for this observation could be the development of compensatory mechanisms via neuroplasticity. Neuroplasticity is a central nervous system function which allows the brain to adapt, especially in cases of disease and injury. In fact, it has been reported that markers of new synaptic growth and axonal

synthesis have increased weeks following injury [181, 182]. In addition, these youth players are still undergoing significant brain development, especially in the DLPFC. It has also been observed that younger brains can more readily adapt to change [183]. However, this reorganization may be detrimental to normal development.

Because near all the metabolites in both brain regions were elevated in high school athletes at *Pre*-season (i.e. before contact practices) it is plausible that the brain has compensated for damage accrued from prior years of play. In fact, this cohort of high school football athletes had on average, seven years of tackle experience. It seems possible that the brain may increase baseline levels of these metabolites in preparation for impending damage. That is, as contact practices and games begin, levels of these metabolites may fall, but they do not reach critically low levels. Instead, metabolites reach levels similar to that of controls. This was observed in M1 where only tCr was still significantly elevated in football athletes at *Post*-season.

The long-term effects of increased baseline levels of these metabolites is unknown. Additional research must be conducted to unveil the potential deleterious effects of this observation.

3.5 Conclusion

In sum, significant neurometabolic changes were observed in both the DLPFC and M1. These changes were significantly correlated with the total count of hits, average PLA, and the percentage of hits greater than 60g. Some of these observations showed position-specific variations, suggesting position may have an effect on sustained hits and neurometabolic changes. Taken together, attention should be paid when studying collision-sport athletes as players can show spectroscopic differences based on their primary position.

3.6 Limitations and Future Work

Limitations of this study include 1) missing data and use of multiple imputations to increase sample size, 2) use of manual voxel placement, 3) variations in time between sessions for each subject, 4) large variability in regression analyses, and 5) sensor reliability. Multiple imputations were only used when one session was missing for a particular subject. This method drastically improved our sample size for statistical analyses. While novel automatic voxel placement methods are currently being developed, no robust methods were available during the length of this study. Therefore, manual voxel placement was necessary and measures were taken to minimize erroneous placement. Lastly, time intervals between sessions were different for each player due to time constraints surrounding imaging. The design of the study could be improved by scanning subjects in a tighter time window. Future work should focus on further investigating the relationships between position and HAEs. For example, it would be interesting to further divide positions by defense, offense, and special teams. However, this would require large sample sizes due to the inherent variations in number of players required per position. Additionally, it would be valuable to investigate the rotational acceleration events. In the current study, this metric was unreliable due to inherent limitations of the gyroscope. However, using more advanced HAE sensors could provide valuable insight into how rotational events may impact position-specific neurometabolic changes - these events have been suggested to cause more significant shear damage to tissue compared to linear events [184].

4. MRS INVESTIGATION IN A COHORT OF MIDDLE SCHOOL AMERICAN FOOTBALL PLAYERS

4.1 Introduction to TBI in Youth (12-14 years) Football Athletes

With the increasing awareness of sports-related concussions in professional players, and the negative impacts on long-term brain health, attention has been placed on the safety of youth football. An epidemiological study conducted by Zhang et al. (2016) found a staggering 143% increase in concussion incidence in patients aged 10-14 years [185]. Additionally, it has been estimated that 300,000 to 3,800,000 mild TBIs occur annually in contact sport athletes aged 14-19 [186]. Daniel et al. (2013) reported greater HAEs during games versus practices, especially HAEs greater than 80g, in players aged 12-14 years [187]. In a study comparing concussion rates in different youth groups, players in sixth and seventh grade were reported more likely to experience a concussion compared to younger players [188] Another study confirmed significant changes in cerebral blood flow in youth athletes (aged 11-15 years) who experienced a sports-related concussion, in addition to poorer ImPACT neurocognitive test scores and reaction time [189]. Other studies have discovered larger symptom counts in those with a history of concussion [190, 191], as well as poorer performance on verbal memory [191]. Unfortunately, there is limited evidence of the long-term impacts of mild TBI in youth contact athletes. However, some studies suggest that symptoms of post-concussive syndrome persist for longer periods of time in this age group [192].

Taken together, youth concussions rates are on the rise, neurocognitive and neurophysiological dysfunctions have been observed, but the long-term effects remain largely unknown. Furthermore, this particular age group (12-14 years) is undergoing significant brain development, especially in the DLPFC which is the last brain

region to reach maturity, and is critically important for executive functions, working memory, and decision making. Therefore, it is critical to further investigate neurophysiological changes in these youth athletes. This body of work presents changes in neurometabolic concentrations in youth football athletes (ages 12-14 years) between the commencement and conclusion of the football season. Magnetic resonance spectroscopy and head-mounted sensors were used to quantify changes in brain metabolites and head acceleration events (HAEs), respectively. This is the *first* report of neurometabolic changes linked with collision-sport participation in this age group.

4.2 Methods

4.2.1 Participants

Twelve male, middle school football athletes participated in this study (ages: 12-14 years, mean = 12.7). Subjects were recruited from a local middle school and imaged twice, once before commencement of contact practice and once at the end of the season. Subjects were further classified based on their position (1 = linemen, 2 = non-linemen, $n_{linemen}$= 5; $n_{nonlinemen}$= 7). 16.7% (2/12) of subjects reported a history of concussion (HoC).

4.2.2 Imaging Timecourse

Subjects were imaged twice over the course of the football season: once prior to contact practice (*Pre*) and once at the commencement of the season (*Post*).

4.2.3 HAE Monitoring

Head acceleration events (HAEs) were monitored for each subject at all practices and games using the X2 Patch Biosystems Sensor (X2 Biosystems; Seattle, WA). The sensor was attached behind the ear using an adhesive patch which was applied after cleansing the area with an alcohol prep pad. After each practice and game, data from

the sensors were downloaded to the Head Impact Moniorting System software (X2 Biosystems; Seattle, WA). The software reported Peak Linear Acceleration (PLA) and Peak Rotational Acceleration (PRA) for each HAE (>10g) and HAEs <20g were discarded [164]. Due to limitations of the gyroscope, PRA was not included in any statistical analyses.

4.2.4 MRS Protocol

All data were collected at Purdue University MRI Facility (West Lafayette, IN). A 3 T GE Signa HDx (Waukesha, WI) was used in combination with a 16-channel brain array coil (Nova Medical; Wilmington, MA). Data were collected using a single voxel PRESS sequence (TE = 30 ms, TR = 1500 ms; averages = 128, FOV = 30 cm^3). For accurate registration and segmentation, a high-resolution T_1 scan was conducted with a 3D SPGR sequence (TE = 1.976 ms, TR = 5.7 ms, averages = 128, with 1 mm isotropic resolution). PRESS voxels were placed in the DLPFC and M1 as shown in Bari et al. (2018) and according to Section 3.2.4 [47]. Correct voxel placement at *Post* was improved by using the reconstructed voxel images from *Pre*. Any sessions where voxel placement in *Post* overlapped with less that 30% of the voxel in *Pre* were discarded.

4.2.5 MRS Post-Processing

Post-processing and spectral quantification followed methods as outlined in Section 3.2.5. This resulted in nine DLPFC subjects and eight M1 subjects.

4.2.6 HAE Post-Processing

Various HAE value were calculated from PLA and hits counts: total hits ($tHits$), cumulative PLA ($cPLA$), average PLA ($aPLA$), maximum PLA ($mPLA$), total hits greater than 40g ($tHits_{40g}$), total hits greater that 60g ($tHits_{60g}$), and total hits greater

than 80g ($tHits_{80g}$). Total Hits ($tHits$), $tHits_{30g}$ $tHits_{40g}$, $tHits_{60g}$, and $tHits_{80g}$ were calculated by counting the total number of hits at the designated threshold (20g, 30g, 40g, 60g, or 80g) for the i^th player.

$$tHits = \sum_{k=1}^{N_{post}} Hits_{k,i} \tag{4.1}$$

$$tHits_{40g} = \sum_{k=1}^{N_{post}} Hits_{k,i,40g} \tag{4.2}$$

$$tHits_{60g} = \sum_{k=1}^{N_{post}} Hits_{k,i,60g} \tag{4.3}$$

$$tHits_{80g} = \sum_{k=1}^{N_{post}} Hits_{k,i,80g} \tag{4.4}$$

Cumulative PLA was calculating by summing all PLA events for the i^th player between *Pre* and *Post*.

$$cPLA = \sum_{k=1}^{N_{post}} PLA_{k,i} \tag{4.5}$$

Average PLA was determined using equation 4.6:

$$aPLA = \frac{cPLA}{tHits} \tag{4.6}$$

Max PLA was determined by selecting the largest PLA sustained between *Pre* and *Post*.

4.2.7 Statistical Analysis

All statistical analyses were conducted in STATA [167]. Because there were instances of missing metabolite data points, multiple imputations were conducted and the means of 50 imputations were reported [168]. Combining the imputed values with preexisting data resulted in 12 DLPFC subjects and 11 M1 subjects. All data were

normally (Shapiro Wilks test) and equally distributed (Bartlett's test) [169,170]. No significant differences across age were observed at *Pre* (ANOVA; p-value >0.05).

Next, session-dependent changes in DLPFC and M1 metabolites were investigated using standard t-test between *Pre* and *Post*. Values reported with p-values less than 0.05 were deemed statistically significant.

Position-dependent effects were also analyzed using t-test. Both position-dependent metabolite changes and position-dependent variations in HAEs were investigated using t-test. Values reported with p-values less than 0.05 were considered statistically significant. If values were statistically significant, they were further analyzed using linear regression to determine associations between metabolites, HAEs, and position. To conduct the linear regression, metabolites were normalized using the following equation:

$$NormalizedMetabolite = \frac{\Delta Metabolite_{pre-post}}{[Metabolite]_{pre}} \tag{4.7}$$

Normalized metabolites were then regressed against hits variables to determine significant associations between changes in metabolic concentrations and HAEs *(tHits, cPLA, aPLA, mPLA,* $tHits_{40g}$*,* $tHits_{60g}$, and $tHits_{80g}$). Cooks Difference was used to determine the significance of potential outliers on the regression models. Using this method, no outliers were shown to significantly affect the outcome of the regressions (Cooks D <5). Therefore, no values were removed for regression analysis.

Next, the concentrations of metabolites in the middle school cohort were compared to those in the high school cohort. This analysis was conducted using the Wilcoxon Ranksum test at *Pre* and *Post*, independently [173]. Differences between *Pre* and *Post* for middle school and high school athletes were also reported.

Lastly, metabolite values in high school controls were compared with middle school and high school athletes, independently, using the Wilcoxon Ranksum test. Each session, *Pre* and *Post*, were analyzed separately. High school controls were imaged during a previous study season but the MRS protocol and MRI model were identical. In addition, these controls were age- and gender-matched, non-collision sport athletes.

4.3 Results

The presented analyses yielded statistically significant changes in DLPFC and M1 metabolites in middle school football athletes. There were also significant differences in correlations between tCr and mPLA, and Glx and aPLA which were position-specific. Significant differences between DLPFC and M1 metabolites in high school and middle school athletes were also unveiled. The remaining section will detail these results.

4.3.1 Changes in DLPFC and M1 Metabolites

DLPFC Metabolites by Position

Inositol significantly decreased in DLPFC between *Pre* and *Post* imaging sessions (p-value = 0.043) (Figure 4.1). When analyzed by position, this observation was only significant in linemen (p-value = 0.0379). While tCr was not significantly different, when divided by position (linemen vs. non-linemen), linemen expressed a significantly lower level of tCr at *Post* (Figure 4.2).

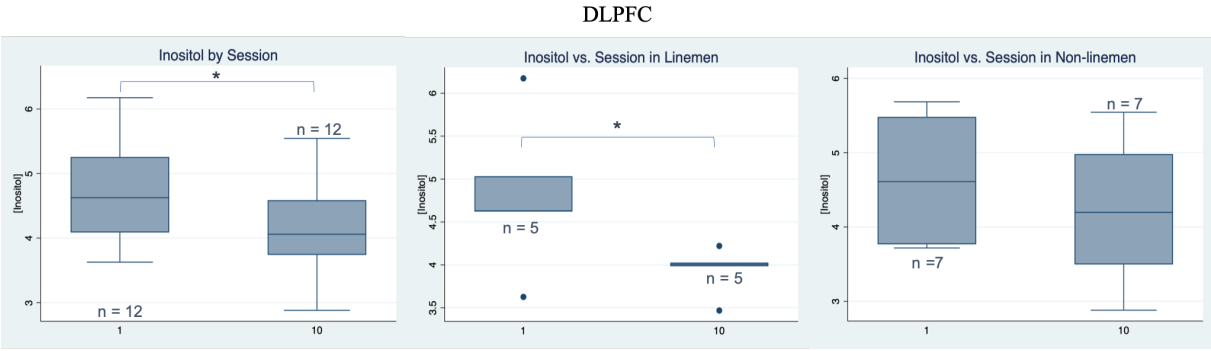

Fig. 4.1. Inositol was significantly lower at *Post* versus *Pre* in middle school football players (* p-value <0.05).

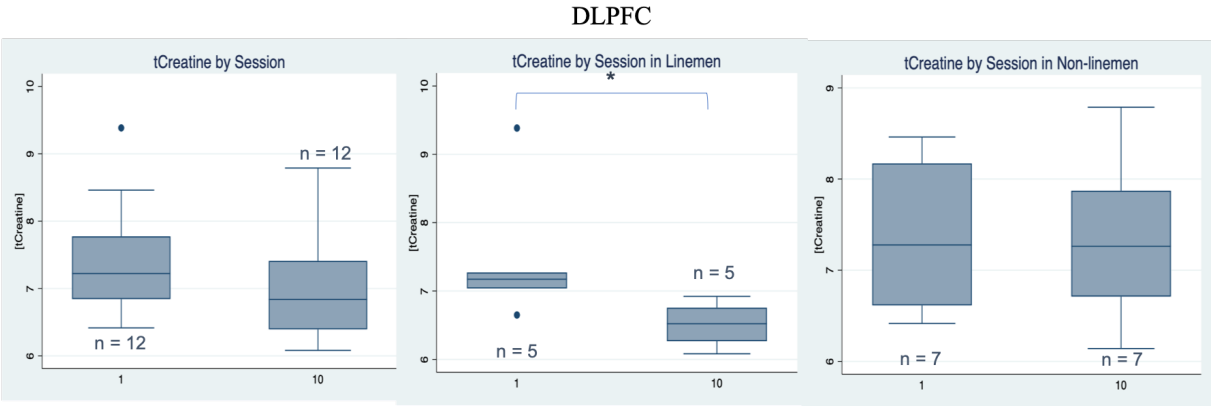

Fig. 4.2. Creatine was lower at *Post*-season imaging compard to *Pre*. This observation was only significant in linemen (* p-value <0.05).

4.3.2 M1 Metabolites by Position

N-acetyl aspartate (NAA) significantly decreased in M1 between sessions *Pre* and *Post* (p-value = 0.030) (Figure 4.2). When analyzed by position, tNAA was significantly lower in non-linemen (p-value = 0.0139).

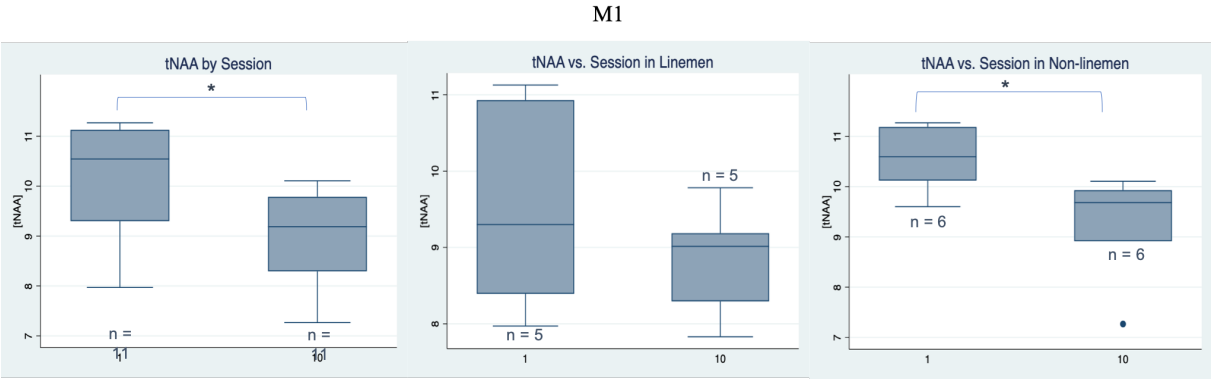

Fig. 4.3. tNAA was significantly lower at *Post* versus *Pre* in middle school linemen (* p-value <0.05).

In addition, M1 tCho was significantly lower in linemen compared to non-linemen (p-value = 0.0156) (Figure 4.4).

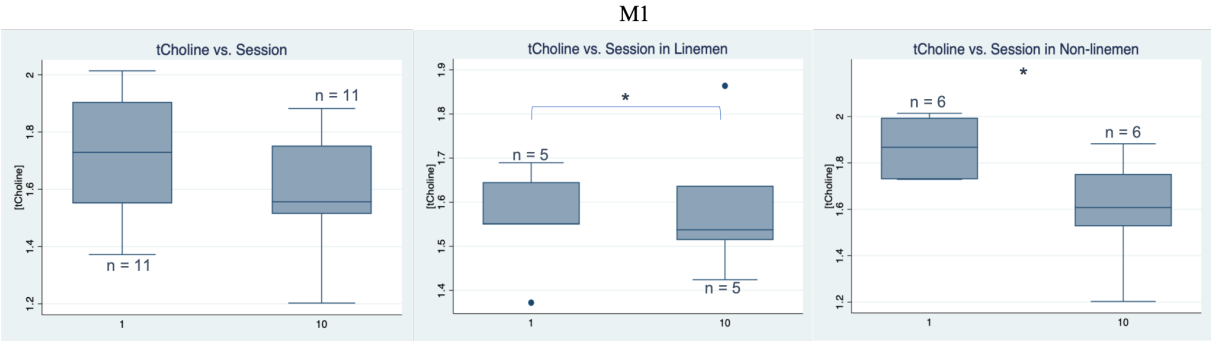

Fig. 4.4. tCholine was significantly lower in linemen compared to non-linemen; no overall trend was observed when both positions were included (* p-value <0.05).

4.3.3 Interactions between Metabolites, HAEs, and Position

While there were no significant changes in HAEs by position, there *were* significant interactions between metabolites and HAEs by position. Coefficients are reported using standardized metabolites and HAE values to relay the true unit change. In DLPFC, normalized tCr significantly increased with increasing mPLA in non-linemen (coefficient = 1.980, p = 0.013) (Figure 4.5). This trend was only observed when positions were analyzed separately (i.e. there was no overall trend when both positions were included in the analysis). In M1, normalized Glx decreased with increasing mean PLA (coefficient = -0.6922, p = 0.013) (Figure 4.6). Analyzing by position, this trend was observed significant in linemen (coefficient = -0.8024, p = 0.038); however, a non-significant negative trend in non-linemen was also observed (coefficient = -0.5743, p = 0.286) (Figure 4.6).

DLPFC

Metabolite	Variable	Position	Trend	Coefficient	*p*-Value
$\Delta tCr/tCr_{pre}$	Max PLA	Linemen	Increase	0.4754	0.741
$\Delta tCr/tCr_{pre}$	Max PLA	Non-linemen	Increase	1.980	0.013

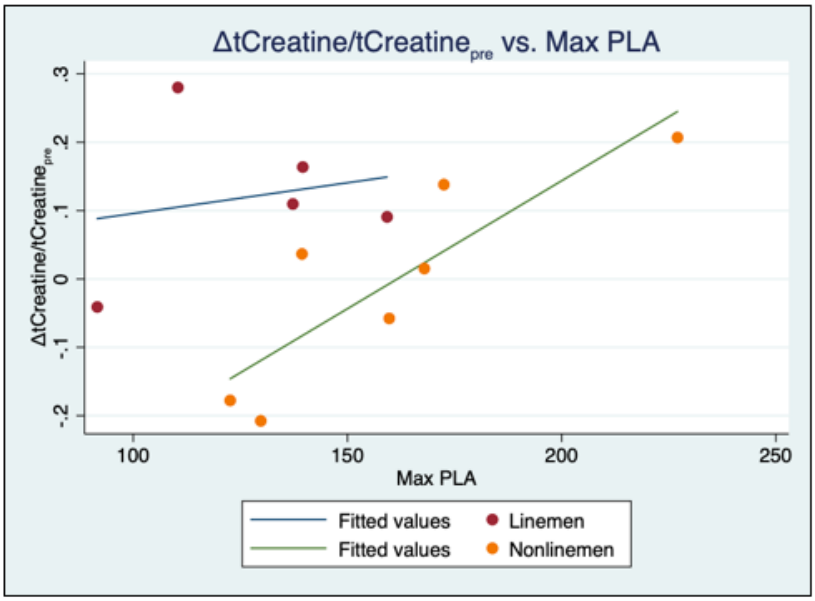

Fig. 4.5. Regression analysis of normalized DLPFC tCr with max PLA. tCr increased with increasing mPLA.

M1

Metabolite	Variable	Position	Trend	Coefficient	*p*-Value
$\Delta Glx/Glx_{pre}$	Mean PLA	Overall	Decrease	-0.6922	**0.013**
$\Delta Glx/Glx_{pre}$	Mean PLA	Linemen	Decrease	-0.8024	**0.038**
$\Delta Glx/Glx_{pre}$	Mean PLA	Non-linemen	Decrease	-0.5743	0.286

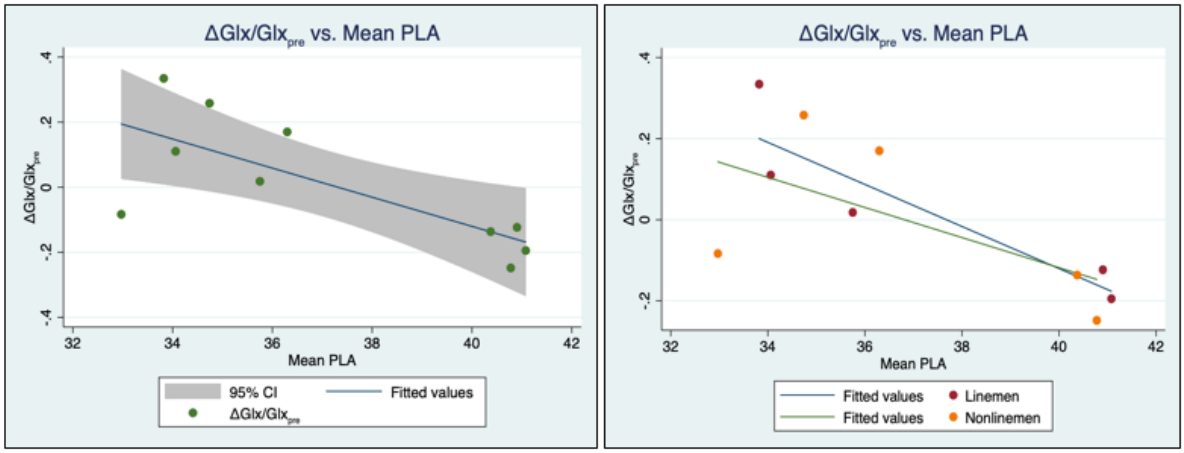

Fig. 4.6. Regression analysis of normalized M1 Glx with mean PLA (aPLA). Glx decreased with increasing aPLA. This observation was significant in linemen.

Thresholding *tHits* at 40g, 60g, and 80g also yielded significant associations with normalized Glx (Figure 4.7). Thresholding at 30g did not yield significant associations (p-value = 0.1159). Coefficients and p-values are displayed in figure 4.7. Specifically, Glx decreased with increasing number of hits exceeding 40g, 60g, and 80g. Analyzing these trends by position, it was observed that linemen exhibited the significant decreases in Glx (Figure 4.8).

Metabolite	Variable	Trend	Coefficient	*p*-Value
$\Delta Glx/Glx_{pre}$	$tHits_{40g}$	Decrease	-0.6059	**0.043**
$\Delta Glx/Glx_{pre}$	$tHits_{60g}$	Decrease	-0.6524	**0.0233**
$\Delta Glx/Glx_{pre}$	$tHits_{80g}$	Decrease	-0.6548	**0.0263**

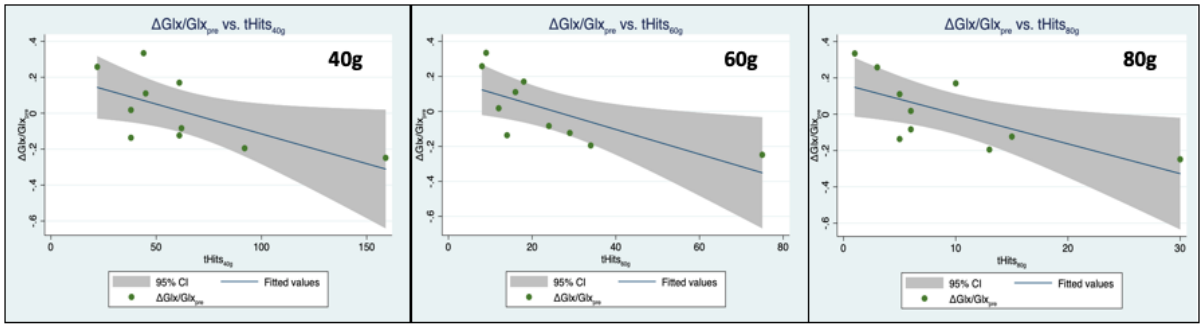

Fig. 4.7. Regression analysis of normalized Glx in M1 with total hits thresholded at 40g, 60g, and 80g. Glx signficantly decreased with increasing hits at all thresholds.

Metabolite	Variable	Position	Trend	Coefficient	*p*-Value
$\Delta Glx/Glx_{pre}$	$tHits_{60g}$	Linemen	Decrease	-1.602	**0.043**
$\Delta Glx/Glx_{pre}$	$tHits_{60g}$	Non-linemen	Decrease	-0.5273	0.183
$\Delta Glx/Glx_{pre}$	$tHits_{80g}$	Linemen	Decrease	-1.335	**0.019**
$\Delta Glx/Glx_{pre}$	$tHits_{80g}$	Non-linemen	Decrease	-0.4698	0.277

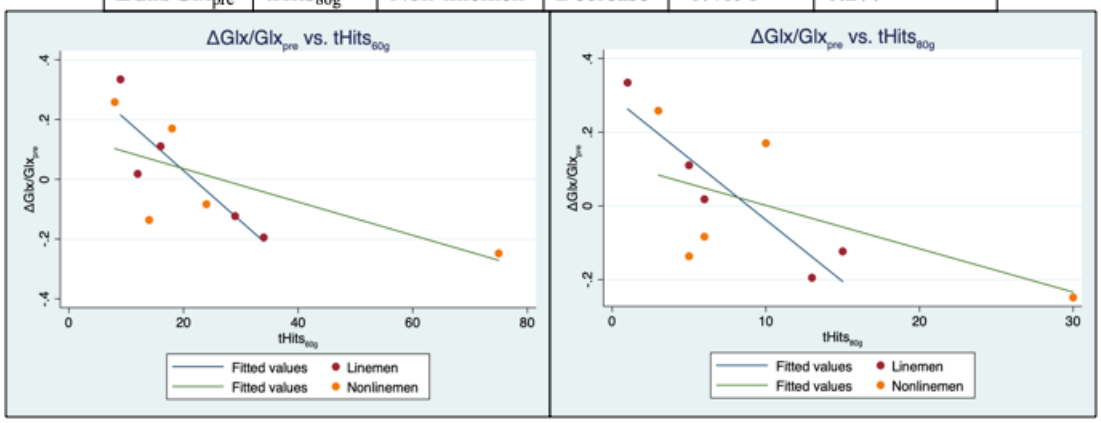

Fig. 4.8. Regression analysis of normalized Glx in M1 against position-specific thresholded hits. Linemen exhibited significant associations between tHits and Glx.

4.3.4 Metabolite Comparison in Middle School vs. High School Football Athletes

Comparisons across level-of-play revealed significant differences between middle school (MSA) and high school (HSA) football athletes between *Pre* and *Post*. These are novel findings which have not yet been reported. In DLPFC, significant differences in tNAA and tCr were observed between MSAs and HSAs at *Pre* and *Post* imaging sessions (Figure 4.8). Specifically, tNAA and tCr were elevated in HSAs compared to MSAs. tNAA was higher at *Pre* (p-value = 0.0029) and *Post* (p-value = 0.0080) in HSAs. tCr was higher at *Pre* (p-value = 0.-381) and *Post* (p-value = 0.-176) in HSAs. Furthermore, tCho was significantly higher in HSAs at *Pre* (p-value = 0.0241).

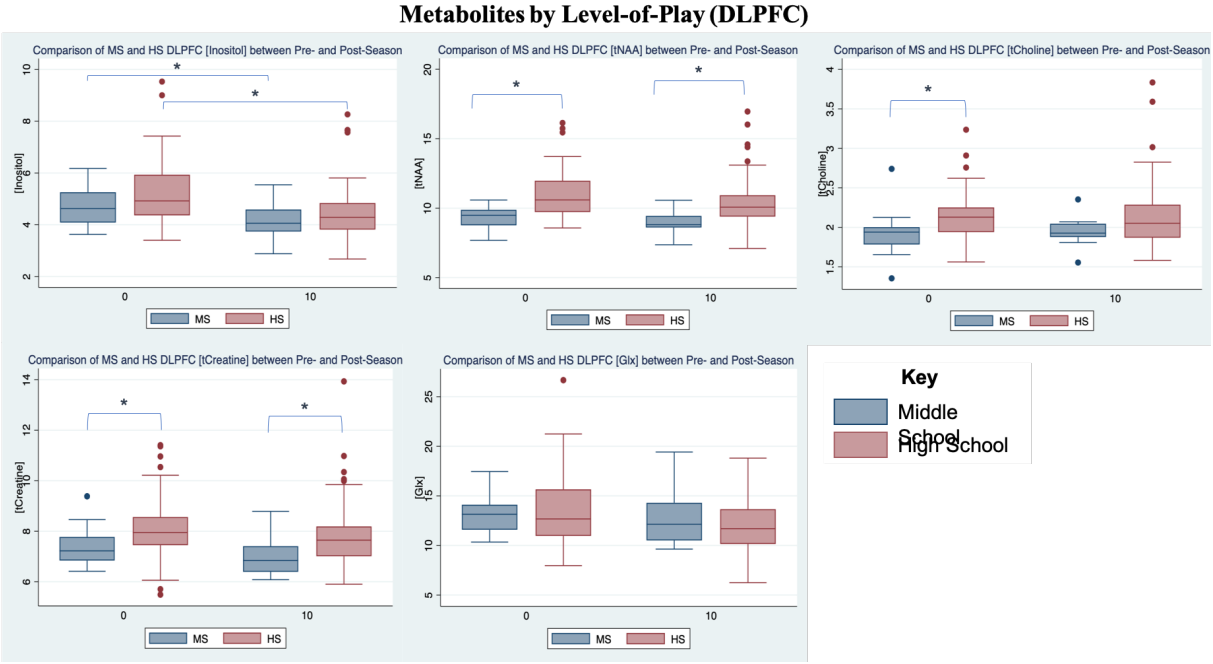

Fig. 4.9. High school athletes exhibited higher levels of tNAA and tCr in DLPFC at both *Pre* and *Post* imaging sessions. tCho was also elevated in high school athletes at *Pre* (Wilcoxon p <0.05).

In M1, significant differences in Ins and tCr were observed between HSAs and MSAs at *Pre* and *Post* imaging sessions (Figure 4.9). Ins was higher in HSAs at *Pre* (p-value = 0.0005) and *Post* (p-value = 0.0080). tCr was also higher at *Pre* (p-value = 0.0167) and *Post* (p-value = 0.0116) in HSAs. In addition, tCho was significantly higher in HSAs at *Pre* (p-value = 0.0273).

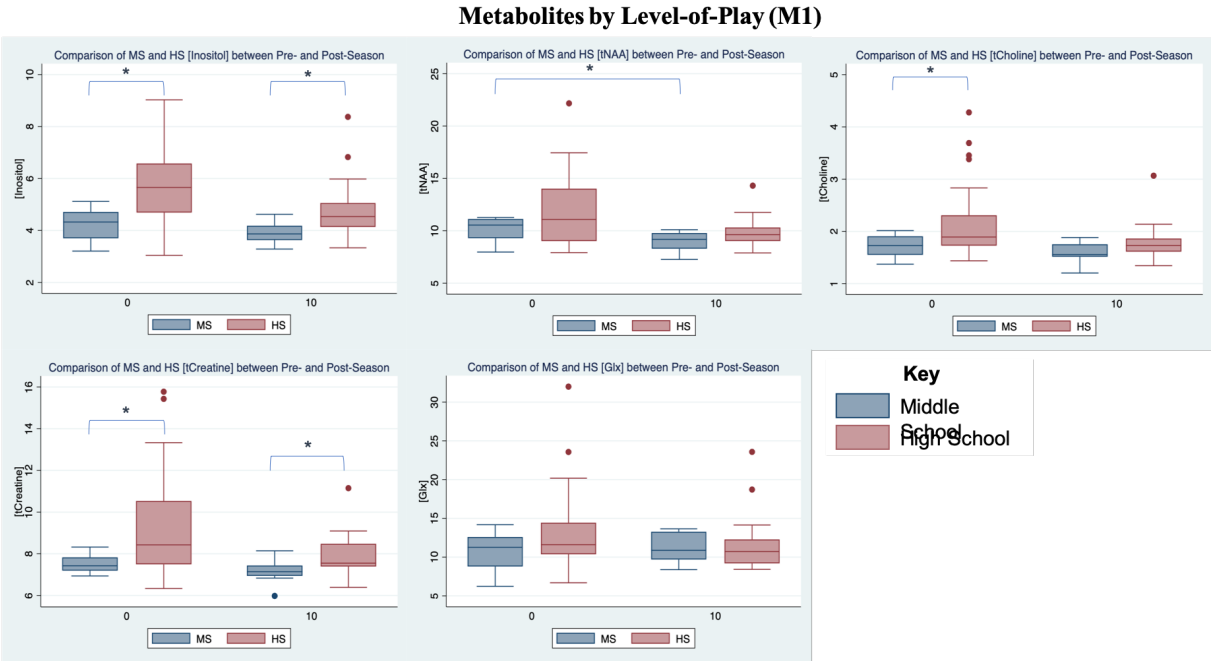

Fig. 4.10. High school athletes exhibited higher levels of Ins and tCr in M1 at both *Pre* and *Post* imaging sessions (Wilcoxon p <0.05)

4.3.5 Metabolite Comparisons Between High School Controls and Middle School and High School Athletes

To better understand the ranges of metabolic changes in these athletes, values were compared against high school controls. It was hypothesized that MSAs would have values consistent with high school controls and HSAs would have elevated metabolite levels. HSAs had significantly higher metabolite levels compared to controls in the

DLPFC. Specifically, Ins, tCho, and tCr were higher that control levels at *Pre* and *Post* and tNAA and Glx were higher at *Pre*. MSAs had significantly higher levels of Ins and Glx compared to controls at *Pre*, however, these were not age-matched controls. In M1, tCr was significantly higher in HSAs at *Pre* and *Post* and Ins, tNAA, and tCho were significantly higher at *Pre*. MSAs showed no significant changes in M1 metabolites compared to controls. Figure 4.11 summarizes the observations.

Control vs. HS M1

Metabolite	Session	p-Value
Ins	Pre	**0.0022**
Ins	Post	0.3268
tNAA	Pre	**0.0241**
tNAA	Post	0.0528
tCho	Pre	**0.0033**
tCho	Post	0.7499
tCr	Pre	**0.0018**
tCr	Post	**0.0094**
Glx	Pre	0.0591
Glx	Post	0.9414

Control vs. HS DLPFC

Metabolite	Session	p-Value
Ins	Pre	**0.0000**
Ins	Post	**0.0089**
tNAA	Pre	**0.0256**
tNAA	Post	0.1255
tCho	Pre	**0.0010**
tCho	Post	**0.0043**
tCr	Pre	**0.0017**
tCr	Post	**0.0153**
Glx	Pre	**0.0173**
Glx	Post	0.6666

Control vs. MS M1

Metabolite	Session	p-Value
Ins	Pre	0.9563
Ins	Post	0.208
tNAA	Pre	0.1253
tNAA	Post	0.5841
tCho	Pre	0.4434
tCho	Post	0.352
tCr	Pre	0.4115
tCr	Post	0.352
Glx	Pre	0.9563
Glx	Post	0.9128

Control vs. MS DLPFC

Metabolite	Session	p-Value
Ins	Pre	**0.0075**
Ins	Post	0.1108
tNAA	Pre	0.1649
tNAA	Post	0.1985
tCho	Pre	0.6807
tCho	Post	0.1985
tCr	Pre	0.5715
tCr	Post	0.5371
Glx	Pre	**0.0034**
Glx	Post	0.4105

Fig. 4.11. Comparison of MSAs and HSAs with high school controls. Bolded p-values are significant (<0.05).

These data are further displayed in box-plot form (Figures 4.12 and 4.13).

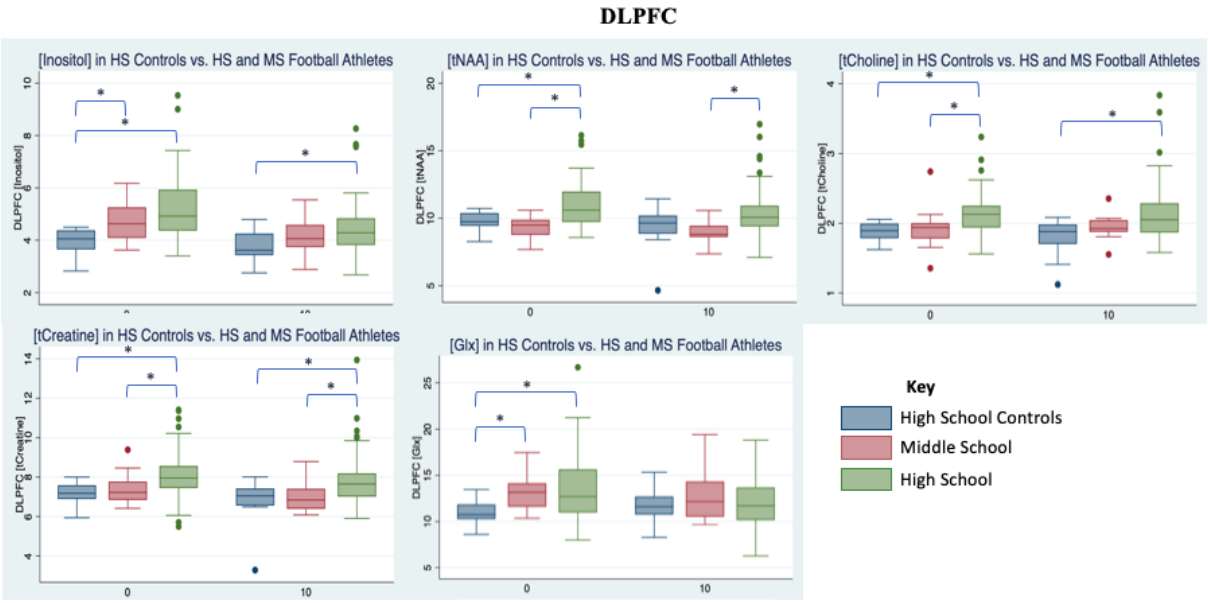

Fig. 4.12. DLPFC metabolite comparison of HSAs and MSAs with high school athletes (* p-value <0.05).

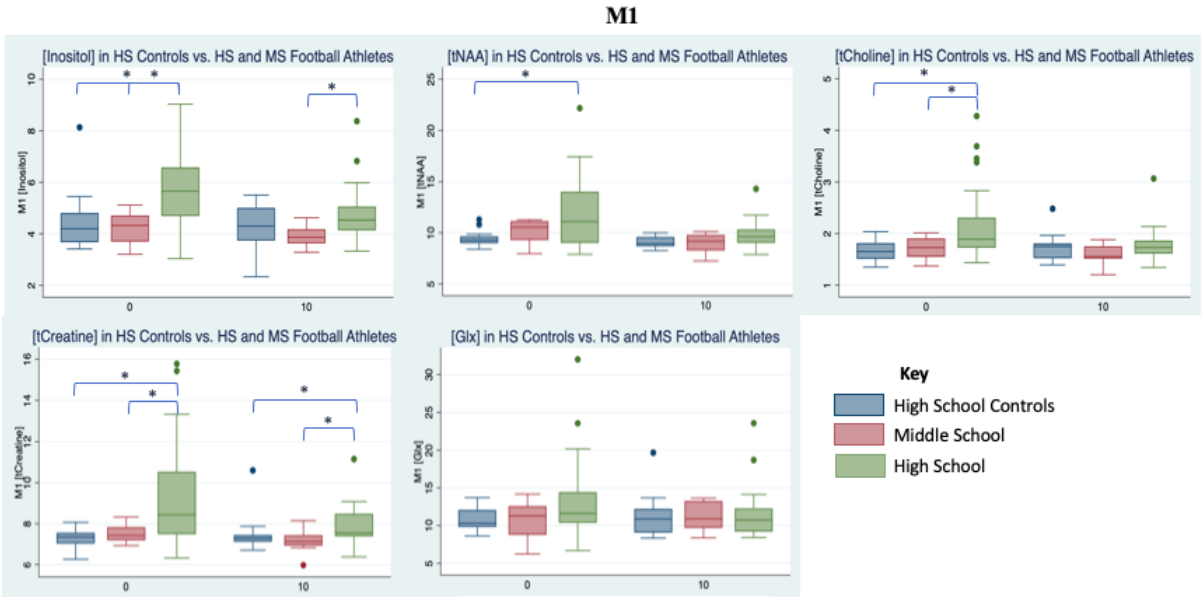

Fig. 4.13. M1 metabolite comparison of HSAs and MSAs with high school athletes (* p-value <0.05).

4.4 Discussion

Given recent reports regarding the damaging effects of American football on brain health, there are concerns surrounding youth participation in contact football. Neurometabolic changes in middle school football athletes have not yet been reported in the literature. Here, we report significant changes in inositol, tNAA, choline, and creatine, as well as significant associations between metabolites and HAEs by position in middle school athletes following a season of football participation. In addition, metabolites were significantly higher in high school athletes compared to middle school athletes and high school controls.

4.4.1 Neurometabolic Changes

Decreased inositol was also reported in the DLPFC of high school athletes (Section 3.4.1) and may be a reflective of an energy crisis and localized swelling. Moreover, tNAA was also decreased in high school athletes (Section 3.4.2) and has been reported in youths with persistent post-concussive syndrome [193]. This metabolite typically decreases following TBI and may be reflective of axonal swelling, energy depletion, and dysfunctional waste removal. Interestingly, when subjects were partitioned by position, Ins and tCr in the DLPFC were significantly lower in linemen versus non-linemen. This observation could, in part, be explained by poor tackling skills. These young players are novice to linemen tackling style and may compensate for lack of strength by more frequently using their head as a weapon. However, the sample size in the linemen cohort was small (n = 5) and a larger sample size would be necessary to better understand this observation. Conversely, tNAA and tCho in M1 were significantly lower in non-linemen - consistent with high school changes. While cPLA was not significantly higher in non-linemen (likely due to small sample size), a trend towards high cPLA in non-linemen ("2") can be observed (Figure 4.14). Linemen ("1") have small variation in magnitude of PLA sustained over the course of

a season. Again, the accumulation of fewer, but higher, magnitude hits in non-linemen could lead to the observed decreases in tNAA and tCho.

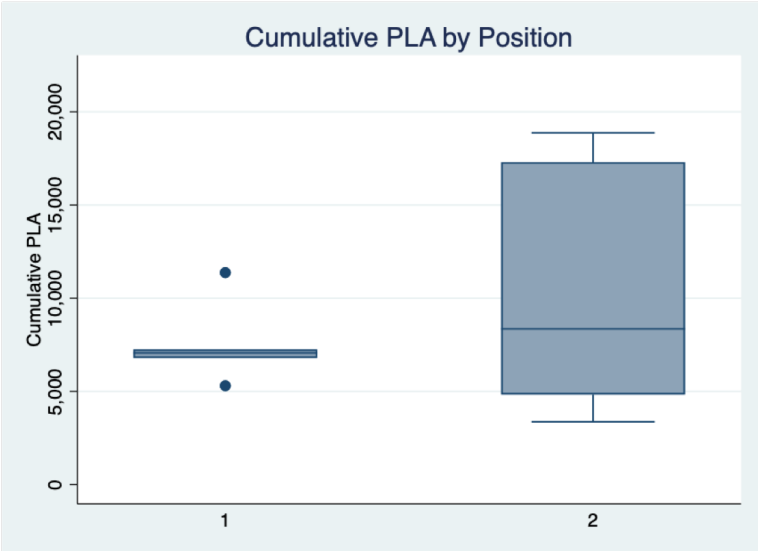

Fig. 4.14. Differences in cPLA by position in middle school athletes (1 = linemen; 2 = non-linemen; $n_{linemen} = 5$; $n_{non-linemen} = 7$).

4.4.2 Interactions Between Metabolite, HAEs, and Position

Regression analysis of metabolites against HAEs by position revealed significant associations between DLPFC tCr and mPLA in non-linemen. Specifically, tCr increased with increasing max PLA. This is an inter sting observation and again, could be due to small sample size. However, another explanation may be related to repair mechanisms. If one large hit event occurs, the brain may require additional ATP (i.e. energy) to repair the damage. This could potentially explain the increase in tCr. However, the exact date and time of the maximum hit event was not evaluated - this could offer more insight into a potential timeline of a tCr response to injury.

Second, M1 Glx significantly decreased with increasing aPLA, $tHits_{40g}$, $tHits_{60g}$, and $tHits_{80g}$ (Figures 4.5-4.8). This trend was observed when both positions were included in the analysis; however, when analyzed by position, only linemen showed

significant associations. These observations are somewhat opposite of what was observed in high school athletes (i.e. decreasing metabolites with increasing HAEs in *non-linemen*). Again, the significant findings in linemen could be a result of poor tackle form and the use of the head as a weapon. As the players gain more experience, their form improves. This may explain why significant associations between HAEs and neurometabolites in high school linemen were not observed. Additionally, 50g has been reported as the threshold in high school football athletes observed to correlated with significant changes in brain homeostasis [47, 194]. However, in middle school athletes, a threshold of 40g was significantly associated with changes in Glx. It could be that the threshold required to elicit observable damage in middle school athletes is lower than for high school athletes. In general, decreased Glx may be indicative of impaired neurotransmission and glutathione synthesis [154].

4.4.3 Differences Between Middle School and High School Athletes

Analysis of middle school (MSAs) versus high school (HSAs) football athletes uncovered interesting differences in metabolite levels between the levels of play.

In DLPFC, HS athletes exhibited higher levels of tNAA and tCr at *Pre* and *Post*. tCho was also elevated at *Pre*-season. These metabolites have been reported to increase with increasing age [195–198]. However, increases in tNAA seem to plateau by age 10, tCr reaches maturity by age four in grey matter regions, and tCho plateaus by the age of one [195, 199]. It could then be concluded that higher concentrations of metabolites in high school football athletes may be abnormal. Yet, MRS studies on neurometabolic profiles are limited and only certain brain regions have been investigated. Given that the DLPFC is the last brain region to fully develop, it is quite possible that this region has higher levels of metabolites in high schoolers. It has been reported that the DLPFC does not reach maturity in males until the age of 21 [200]. Until this point, the DLPFC is undergoing significant synaptic pruning and myelination, as certain pathways are strengthening [201]. Higher levels of tNAA,

tCho, and Ins may be reflective of an increased demand for myelin synthesis in this particular brain regions. However, significant research must be conducted to further understand these observations.

In M1, HSAs exhibited higher Ins and tCr at *Pre* and *Post*. tCho was also elevated at *Pre*. *Myo*-inositol, an astrocytic osmolyte, reaches mature levels by years 2-3 [199]. Inositol was significantly lower in HSAs at session *In1*, *In2*, and *Post1* (Figure 3.4), but was still significantly higher than MSA levels at both *Pre* and *Post*. Similar to DLPFC observations, tCr and tCho were also higher. Again, these metabolites (Ins, tCho, tCr) should reach mature levels no later than the age of four. Higher levels of these metabolites in HSAs might be indicative of 1) normal changes during development or 2) accumulated injury or compensatory mechanisms. While the DLPFC is still undergoing significant reorganization during high school years, M1 should be more robust as it is the primary motor region responsible for movement, coordination, and dexterity. However, research does suggest that this region is also critically important for motor learning and memory. One reason for higher observed Ins and tCho in high school M1 may be reflective of motor learning and memory for football-related tasks. However, this is unlikely given that these metabolites decrease during the season. Second, the observed elevation could be the result of accumulated damage and neuroplasticity. Following cumulative and repetitive damage, the brain may compensate by increasing metabolite levels [181]. This could explain why these metabolites are elevated in high school football athletes at *Pre*. By elevating metabolite levels before exposure to damaging HAEs, metabolites may not fall to critical levels. In fact, elevated levels of Ins and Glx in the DLPFC were also seen in MSAs *Pre* only. On average, this cohort of MSAs had 2.6 years of prior tackle experience. Therefore, even a few years of experience may initiate these compensatory mechanisms.

4.5 Conclusion

The above study presents the first report of MRS changes in middle school athletes. Ins and tCr in DLPFC were significantly lower in MSAs at the *Post* season imaging and changes in these metabolites were specific to linemen. tNAA and tCho in M1 were also lower at *Post* and changes in these metabolites were specific to non-linemen. Additionally, tCr significantly increased with increased mPLA and Glx exhibited significant negative associations with aPLA, tHits_{40g}, tHits_{60g}, and tHits_{80g}. Lastly, Ins, tNAA, tCho, tCr, and Glx were significantly higher in HSAs compared to MSAs. These findings could be indicative of significant neurophysiological compensation in HSAs. Taken together, particular attention should be focused on youth collision-sport athletes as 1) this age group may be more susceptible to neurometabolic changes, and 2) effects of persistently elevated metabolite levels are unknown.

4.6 Limitations and Future Work

A major limitation of this study was sample size. Only 12 DLPFC subjects and 11 M1 subjects were included in statistical analyses. Future work should be completed with larger sample sizes. In addition, it is critically important to understand any long-term effects of HAEs and concussion in youth athletes. Therefore, significant research should be completed to address the physiological, psychological, and cognitive impacts of youth football participation.

5. SUMMARY AND FUTURE WORK

The presented work highlights various applications of the MRS methodology to understand advanced physiological phenomena related to traumatic brain injury. Below is a summary of each investigation and an outline of corresponding future research.

5.1 Novel Biomarker Investigation

Current procedures used to diagnose TBI are mostly qualitative in nature, therefore making it difficult to predict patient outcomes. This problem warrants the investigation of quantitative biomarkers of TBI that can predict neurological outcomes. Acrolein is a toxic reactive oxygen species that is both a product and promoter of oxidative stress. It has been show to increase following TBI, substantiating its potential as a TBI biomarker. Acrolein was first investigated using NMR and found to have long T_1 and T_2 relaxation times - not uncommon of small aldehydes. Accordingly, TR was adjusted in later MRS protocols and acrolein was deemed quantifiable at 1 M, 100 mM, and 10 mM concentrations in water and whole-brain phantoms. This provides sufficient evidence that acrolein may be quantifiable *in vivo*, but further investigation is required to 1) quantify acrolein in tissue, 2) correlate injury severity with relative acrolein concentration, using controlled closed-head impact animal models, and 3) understand the predictive power of acrolein on neurological outcomes. Based on extensive future work, this method could ultimately be applied to localize injury severity, thereby specializing patient treatment plans and improving patient-specific outcomes.

5.2 MRS Investigation of Position-Specific Effects on Neurometabolic Changes in High School and Middle School Athletes

The incidence of sports-related concussion is increasing, especially in youth athletes. This could be attributed, in part, to heightened awareness of symptoms; however, many studies suggest a lack of symptom reporting in this population. MRS can provide valuable information regarding disruptions in neurometabolic homeostasis. Even so, MRI examinations are expensive and therefore do not provide a means for frequent collision-sport athletic check-ups. Instead, less expensive and quantitative methods should be used to predict possible TBI sequelae - such as head acceleration monitors. However, these methods must first be validated against quantifiable measures of brain dysfunction - such as spectroscopic data. Fifty-five high school and 12 middle school football athletes were imaged over the course of a football season. Head acceleration events (HAEs) were also monitored at every practice and game. Significant changes in brain metabolites were found in both populations, with the majority of changes occurring in the primary motor cortex. HAEs were significantly associated with decreases in some of the observed metabolites, suggesting cumulative hits are predictive of greater neurometabolic changes. Position-effects were also evaluated between linemen and non-linemen. In high school athletes, linemen showed a higher number of HAEs, but non-linemen experienced larger accelerations. Neurometabolic changes were significantly associated with position type. When comparing middle school and high school athletes, metabolites (Ins, tNAA, tCho, and tCr) were found to be significantly higher in high school athletes. This could reflect more severe metabolic dysfunction in middle school athletes. Taken together, significant neurometabolic changes were observed in both high school and middle school athletes. These changes can be partially be explained by position and HAEs.

Previous work also supports these findings [44,47] and emphasizes the importance of improving prevention, diagnosis, and treatment of sports-related concussion in youth athletes. However, limitations exist and future work must be completed to

fully understand the specific mechanisms on position-specific injury. Next, it will be important to increase the sample size of the middle school cohort. In addition, steps should be made to move away from using MRI as a diagnostic tool for sports-related concussion. Instead, focus should be put on quantitative and inexpensive methods (i.e. sensors and sideline tests) that can accurately predict neuropathology, using neuroimaging as a gold standard for initial validation.

5.3 Closing Remarks

In close, MRI is a powerful tool that can be used to evaluate a wide range of research questions. The presented work focused on the application of MRS to better understand physiological phenomena noninvasively, specifically related to traumatic brain injuries. Future work should focus on furthering the goals of each project, respectively, in hopes of improving outcomes in collision sport athletes.

REFERENCES

[1] J. L. Larmor, "On the Theory of Magnetic Influence on Spectra; and On the Radiation from Moving Ions," *Philosophical Magazine*, vol. 44, no. 271, pp. 503–512, 1897.

[2] F. Bloch, "Nuclear Induction," *Physical Review*, vol. 70, pp. 460–474, 1946.

[3] M. Goldman, "Formal Theory of Spin-Lattice Relaxation," *Journal of Magnetic Resonance*, vol. 149, pp. 160–187, 2001. [Online]. Available: https://www.ncbi.nlm.nih.gov/pubmed/11318616

[4] D. G. Nishimura, *Principles of Magnetic Resonance Imaging*, 1st ed. Stanford, 2016.

[5] W. Proctor and F. Yu, "The Dependence of a Nuclear Magnetic Resonance Frequency upon Chemical Compound," *Physical Review*, vol. 77, p. 717, 1950.

[6] R. K. Harris, E. D. Becker, S. M. Cabral De Menezes, R. Goodfellow, and P. Granger, "NMR Nomenclature: Nuclear Spin Properties and Conventions for Chemical Shifts (IUPAC Recommendations 2001)," Tech. Rep., 2002.

[7] P. Lauterbur, "Image Formation by Induced Local Interactions: Examples Emplying Nuclear Magnetic Resonance," *Nature*, vol. 242, pp. 190–191, 1973.

[8] S. Tobo-Hidalgo, "Theory of Gradient Coil Design Methods for Magnetic Reonance Imaging," *Concepts in Magnetic Resonance Part A*, vol. 36A, pp. 223–242, 2001.

[9] R. Hashemi, W. Bradley, and C. Lisanti, *MRI: The Basics*, L. W. a. Wilkins, Ed., 2010.

[10] R. Hendrick, *Glossary of MR Terms*, 5th ed. Reston, VA: American College of Radioloy, 2005.

[11] J. M. Tognarelli, M. Dawood, M. I. F. Shariff, V. P. B. Grover, M. M. E. Crossey, I. J. Cox, S. D. Taylor-Robinson, and M. J. W. McPhail, "Magnetic Resonance Spectroscopy: Principles and Techniques: Lessons for Clinicians." *Journal of Clinical and Experimental Hepatology*, vol. 5, no. 4, pp. 320–8, 12 2015.

[12] P. A. Bottomley, "Spatial Localization in NMR Spectroscopy in Vivo," *Annals of the New York Academy of Sciences*, vol. 508, no. 1, pp. 333–348, 1987.

[13] P. Bottomley, "4480228 Selective volume method for performing localized NMR spectroscopy," *Magnetic Resonance Imaging*, vol. 3, no. 1, pp. iv–v, 1985.

[14] J. Cooley and J. Tukey, "An Algorithm for the Machine Calculation of Complex Fourier Series," *Mathetmatics of Computation*, vol. 19, pp. 297–301, 1965.

[15] T. Gallagher, A. Nemeth, and L. Hacein-Bey, "An Introduction to the Fourier Transform: Relationship to MRI," *AJR American Journal of Roentgenology*, vol. 190, pp. 1396–1405, 2008.

[16] J. R. Alger, "Quantitative proton magnetic resonance spectroscopy and spectroscopic imaging of the brain: a didactic review." *Topics in magnetic resonance imaging : TMRI*, vol. 21, no. 2, pp. 115–28, 4 2010.

[17] L. Xin and I. Tkáč, "A practical guide to in vivo proton magnetic resonance spectroscopy at high magnetic fields," *Analytical Biochemistry*, vol. 529, pp. 30–39, 7 2017.

[18] Z. Tong, T. Yamaki, K. Harada, and K. Houkin, "In vivo quantification of the metabolites in normal brain and brain tumors by proton MR spectroscopy using water as an internal standard," *Magnetic Resonance Imaging*, vol. 22, no. 7, pp. 1017–1024, 9 2004.

[19] P. Barker, B. Soher, S. Blackband, J. Chatham, V. Mathews, and N. Bryan, "Quantitation of Proton NMR Spectra of the Human Brain Using Tissue Water as an Internal Concentration Reference," *NMR in Biomedicine*, vol. 6, pp. 89–94, 1993. [Online]. Available: http://mriquestions.com/uploads/3/4/5/7/34572113/barker_water_reference_quantification.pdf

[20] C. Gasparovic, T. Song, D. Devier, H. J. Bockholt, A. Caprihan, P. G. Mullins, S. Posse, R. E. Jung, and L. A. Morrison, "Use of Tissue Water as a Concentration Reference for Proton Spectroscopic Imaging," *Magnetic Resonance in Medicine*, vol. 55, pp. 1219–1226, 2006.

[21] E. Dhamala, I. Abdelkefi, M. Nguyen, T. J. Hennessy, H. Nadeau, and J. Near, "Validation of in vivo MRS measures of metabolite concentrations in the human brain," *NMR in Biomedicine*, vol. 32, no. 3, p. e4058, 3 2019.

[22] L. Minati, D. Aquino, M. G. Bruzzone, and A. Erbetta, "Quantitation of normal metabolite concentrations in six brain regions by in-vivo 1 H-MR spectroscopy," *Journal of Medical Physics / Association of Medical Physicists of India J Med Phys*, vol. 35, no. 3, pp. 154–163, 2010.

[23] M. Weiger, D. Moskau, R. Kerssebaum, and W. Hull, "Gradient Shimming: Principles and Practical Aspects," Bruker Biospin, Tech. Rep., 2005.

[24] R. Gruetter, "Automatic, Localized in Vivo Adjustment of all First- and Second-Order Shim Coil," *Magnetic Resonance in Medicine*, vol. 29, pp. 804–811, 1993.

[25] B. H. H Mitchell, T. S. Hamilton, R. Steggerda, H. W. Bean, and A. Husbandry, "The Chemical Composition of the Adult Human Body and its Bearing on the Biochemistry of Growth," *Journal of Biological Chemsitry*, no. 158, pp. 625–637, 1945.

[26] Y. Rathi, L. Ning, O. Michailovich, H. Liao, B. Gagoski, P. Grant, M. Shenton, R. Stern, C.-F. Westin, and A. Lin, "Maximum entropy estimation of Glutamate and Glutamine in MR spectroscopic imaging," *Medical image computing and computer-assisted intervention*, vol. 17, no. 2, pp. 749–756, 2014.

[27] R. A. De Graaf and K. Nicolay, "Adiabatic RF Pulses: Applications to In Vivo NMR," *Concepts in Magnetic Resonance*, vol. 9, pp. 247–268, 1997.

[28] A. Haase, J. Frahm, W. Hanicke, and D. Matthaei, "'H NMR chemical shift selective (CHESS) imaging," Tech. Rep. 4, 1985.

[29] I. Tkáč and R. Gruetter, "Methodology of H NMR Spectroscopy of the Human Brain at Very High Magnetic Fields." *Applied magnetic resonance*, vol. 29, no. 1, pp. 139–157, 3 2005.

[30] J. Felmlee, "Spatial Presaturation: A Method for Suppressing Flow Artifacts and Improving Depiction of Vascular Anatomy In MR Imaging'," *Radiology*, vol. 164, pp. 559–564, 1987.

[31] E. Kaldoudi, S. Williams, G. Barker, and P. Tofts, "A Chemical Shift Selective Inversion Recovery Sequence for Fat-Suppressed MRI: Theory and Experimental Validation," *Magnetic Resonance Imaging*, vol. 11, pp. 341–355, 1993.

[32] S. R. Dager, N. M. Corrigan, T. L. Richards, and S. Posse, "Research applications of magnetic resonance spectroscopy to investigate psychiatric disorders." *Topics in magnetic resonance imaging : TMRI*, vol. 19, no. 2, pp. 81–96, 4 2008.

[33] A. Horská and P. B. Barker, "Imaging of brain tumors: MR spectroscopy and metabolic imaging." *Neuroimaging clinics of North America*, vol. 20, no. 3, pp. 293–310, 8 2010.

[34] J. M. Soares, P. Marques, V. Alves, and N. Sousa, "A hitchhiker's guide to diffusion tensor imaging." *Frontiers in neuroscience*, vol. 7, p. 31, 2013.

[35] V. Baliyan, C. J. Das, R. Sharma, and A. K. Gupta, "Diffusion weighted imaging: Technique and applications." *World journal of radiology*, vol. 8, no. 9, pp. 785–798, 9 2016.

[36] P. Agarwal and I. D. Rupenthal, "Injectable implants for the sustained release of protein and peptide drugs," *Drug Discovery Today*, vol. 18, no. 7-8, pp. 337–349, 4 2013.

[37] R. L. Dunn, J. P. English, D. R. Cowsar, and D. P. Vanderbilt, "Biodegradable in-situ forming implants and methods of producing the same," 11 1999. [Online]. Available: https://patents.google.com/patent/US5990194A/en

[38] E. O. Stejskal and J. E. Tanner, "Spin Diffusion Measurements: Spin Echoes in the Presence of a TimeDependent Field Gradient," *The Journal of Chemical Physics*, vol. 42, no. 1, pp. 288–292, 1 1965.

[39] E. Hahn, "Spin Echoes," *Physical Review*, vol. 80, no. 4, pp. 580–594, 1950.

[40] R. G. Brewer and E. L. Hahn, "Atomic Memory," *Scientific America*, vol. 251, no. 6, pp. 50–57, 1984.

[41] D. Le Bihan, E. Breton, D. Lallemand, P. Grenier, E. Cabanis, and M. Laval-Jeantet, "MR Imaging of Intravoxel Incoherent Motions: Application to Diffusion and Perfusion in Neurologic Disorders'," *Radiology*, vol. 161, pp. 401–407, 1986.

[42] P. Hagmann, L. Jonasson, P. Maeder, J.-P. Thiran, V. J. Wedeen, and R. Meuli, "Understanding Diffusion MR Imaging Techniques: From Scalar Diffusion-weighted Imaging to Diffusion Tensor Imaging and Beyond," *RadioGraphics*, vol. 26, no. 1, pp. S205–S223, 10 2006.

[43] S. Ashwal, B. Holshouser, K. Tong, T. Serna, R. Osterdock, M. Gross, and D. Kido, "Proton Spectroscopy Detected Myoinositol in Children with Traumatic Brain Injury," *Pediatric Research*, vol. 56, no. 4, pp. 630–638, 10 2004.

[44] V. N. Poole ab, K. Abbas, T. E. Shenk, E. L. Breedlove, K. M. Breedlove, M. E. Robinson, L. J. Leverenz, E. A. Nauman abd, T. M. Talavage ac, U. Dydak fg, V. N. Poole, E. A. Nauman, and T. M. Talavage, "Developmental Neuropsychology MR Spectroscopic Evidence of Brain Injury in the Non-Diagnosed Collision Sport Athlete," *Developmental Neuropsychology*, vol. 39, no. 6, pp. 459–473, 2014.

[45] J. R. Moffett, P. Arun, P. S. Ariyannur, and A. M. A. Namboodiri, "N-Acetylaspartate reductions in brain injury: impact on post-injury neuroenergetics, lipid synthesis, and protein acetylation," *Frontiers in Neuroenergetics*, vol. 5, p. 11, 12 2013.

[46] R. Vagnozzi, S. Signoretti, L. Cristofori, F. Alessandrini, R. Floris, E. Isgrò, A. Ria, S. Marziale, G. Zoccatelli, B. Tavazzi, F. D. Bolgia, R. Sorge, S. P. Broglio, T. K. Mcintosh, and G. Lazzarino, "Assessment of metabolic brain damage and recovery following mild traumatic brain injury: a multicentre, proton magnetic resonance spectroscopic study in concussed patients," *Brain*, vol. 133, no. 11, pp. 3232–3242, 2010.

[47] S. Bari, D. O. Svaldi, I. Jang, T. E. Shenk, V. N. Poole, T. Lee, U. Dydak, J. V. Rispoli, E. A. Nauman, and T. M. Talavage, "Dependence on subconcussive impacts of brain metabolism in collision sport athletes: an MR spectroscopic study," *Brain Imaging and Behavior*, vol. 13, no. 3, pp. 735–749, 6 2019.

[48] R. Shi, T. Rickett, and W. Sun, "Acrolein-mediated injury in nervous system trauma and diseases," *Molecular Nutrition and Food Research*, vol. 55, no. 9, pp. 1320–1331, 2011.

[49] M. Cruz-Haces, J. Tang, G. Acosta, J. Fernandez, and R. Shi, "Pathological correlations between traumatic brain injury and chronic neurodegenerative diseases," *Translational Neurodegeneration*, vol. 6, no. 1, p. 20, 12 2017.

[50] M. K. Walls, N. Race, L. Zheng, S. Vega-alvarez, G. Acosta, J. Park, and R. Shi, "Structural and biochemical abnormalities in the absence of acute deficits in mild primary blast-induced head trauma," *Journal of neurosurgery*, vol. 124, no. 3, pp. 675–686, 2016.

[51] CDC, "Report to Congress on Traumatic Brain Injury In the United States: Epidemiology and Rehabilitation," National Center for Injury Prevention and Control; Division of Unintentional Injury Prevention, Atlanta, GA, Tech. Rep., 2015. [Online]. Available: https://www.cdc.gov/traumaticbraininjury/pdf/TBI_Report_to_Congress_Epi_and_Rehab-a.pdf

[52] M. Clark and K. Guskiewicz, *Sport-Related Traumatic Brain Injury*. CRC Press/Taylor and Francis Group, 2016. [Online]. Available: http://www.ncbi.nlm.nih.gov/pubmed/26583180

[53] M. E. O'Neil, K. Carlson, D. Storzbach, L. Brenner, M. Freeman, A. Quiñones, M. Motu'apuaka, M. Ensley, and D. Kansagara, "Complications of Mild Traumatic Brain Injury in Veterans and Military Personnel: A Systematic Review." Washington (DC): Department of Veterans Affairs (US), 2013, ch. Appendix C. [Online]. Available: https://www.ncbi.nlm.nih.gov/books/NBK189784/

[54] C. A. Taylor, J. M. Bell, M. J. Breiding, and L. Xu, "Traumatic Brain InjuryRelated Emergency Department Visits, Hospitalizations, and Deaths United States, 2007 and 2013," *MMWR. Surveillance Summaries*, vol. 66, no. 9, pp. 1–16, 2017.

[55] M. Faul and V. Coronado, "Epidemiology of traumatic brain injury," *Handbook of Clinical Neurology*, vol. 127, pp. 3–13, 1 2015.

[56] M. D. Budde, A. Shah, M. McCrea, W. E. Cullinan, F. A. Pintar, and B. D. Stemper, "Primary blast traumatic brain injury in the rat: relating diffusion tensor imaging and behavior." *Frontiers in Neurology*, vol. 4, no. 154, pp. 1–12, 2013.

[57] T. W. McAllister, "Neurobiological consequences of traumatic brain injury." *Dialogues n Clinical Neuroscience*, vol. 13, no. 3, pp. 287–300, 2011.

[58] J. Rey, V. Rosenfeld, A. C. Mcfarlane, P. Bragge, R. A. Armonda, J. B. Grimes, G. Rey, and S. Ling, "Blast-related traumatic brain injury," *The Lancet Neurology*, vol. 12, no. 9, pp. 882–893, 2013.

[59] D. Nizamutdinov and L. A. Shapiro, "Overview of Traumatic Brain Injury: An Immunological Context." *Brain sciences*, vol. 7, no. 1, 1 2017.

[60] E. D. Hall, "The Contributing Role of Lipid Peroxidation and Protein Oxidation in the Course of CNS Injury Neurodegeneration and Neuroprotection: An Overview," in *Brain Neurotrauma*, F. Kobeissy, Ed. Boca Raton (FL): CRC Press/Taylor & Francis, 2015, ch. 6: Molecul. [Online]. Available: http://www.ncbi.nlm.nih.gov/pubmed/26269884

[61] B. Halliwell, "Reactive Oxygen Species and the Central Nervous System," *Journal of Neurochemistry*, vol. 59, no. 5, pp. 1609–1623, 11 1992.

[62] R. Shi, J. Page, and M. Tully, "Molecular mechanisms of acrolein-mediated myelin destruction in CNS trauma and disease," *Free Radical Research*, vol. 49, no. 7, pp. 888–895, 2015.

[63] J. D. Corrigan and F. M. Hammond, "Traumatic Brain Injury as a Chronic Health Condition," *Archives of Physical Medicine and Rehabilitation*, vol. 94, no. 6, pp. 1199–1201, 6 2013.

[64] R. E. A. Green, "Editorial: Brain Injury as a Neurodegenerative Disorder," *Frontiers in Human Neuroscience*, vol. 9, p. 615, 1 2016.

[65] V. E. Johnson, W. Stewart, and D. H. Smith, "Widespread Tau and Amyloid-Beta Pathology Many Years After a Single Traumatic Brain Injury in Humans," *Brain Pathology*, vol. 22, no. 2, pp. 142–149, 3 2012.

[66] P. M. Washington, S. Villapol, and M. P. Burns, "Polypathology and dementia after brain trauma: Does brain injury trigger distinct neurodegenerative diseases, or should they be classified together as traumatic encephalopathy?" *Experimental Neurology*, vol. 275, no. 3, pp. 381–388, 2016.

[67] R. C. Gardner and K. Yaffe, "Epidemiology of mild traumatic brain injury and neurodegenerative disease," *Molecular and Cellular Neuroscience*, vol. 66, no. B, pp. 75–80, 2015.

[68] D. H. Daneshvar, L. E. Goldstein, P. T. Kiernan, T. D. Stein, and A. C. McKee, "Post-traumatic neurodegeneration and chronic traumatic encephalopathy," pp. 81–90, 2015.

[69] S.-T. Yang, I.-T. Hsiao, C.-J. Hsieh, Y.-H. Chiang, T.-C. Yen, W.-T. Chiu, K.-J. Lin, and C.-J. Hu, "Accumulation of amyloid in cognitive impairment after mild traumatic brain injury," *Journal of the Neurological Sciences*, vol. 349, no. 1-2, pp. 99–104, 2 2015.

[70] H. M. Bramlett and W. D. Dietrich, "Long-Term Consequences of Traumatic Brain Injury: Current Status of Potential Mechanisms of Injury and Neurological Outcomes." *Journal of neurotrauma*, vol. 32, no. 23, pp. 1834–48, 12 2015.

[71] T. C. Lye and E. A. Shores, "Traumatic brain injury as a risk factor for Alzheimer's disease: a review." *Neuropsychology review*, vol. 10, no. 2, pp. 115–29, 6 2000.

[72] S. Deb, I. Lyons, and C. Koutzoukis, "Neurobehavioural symptoms one year after a head injury," *British Journal of Psychiatry*, vol. 174, no. 4, pp. 360–365, 4 1999.

[73] L. E. Collins-Praino and F. Corrigan, "Does neuroinflammation drive the relationship between tau hyperphosphorylation and dementia development following traumatic brain injury?" *Brain Behav Immun*, vol. 60, pp. 369–382, 2017.

[74] K. R. Walker and G. Tesco, "Molecular mechanisms of cognitive dysfunction following traumatic brain injury." *Frontiers in Aging Neuroscience*, vol. 5, no. 29, pp. 1–25, 2013.

[75] D. P. Ghilarducci and R. S. Tjeerdema, "Fate and effects of acrolein." *Reviews of environmental contamination and toxicology*, vol. 144, pp. 95–146, 1995.

[76] T. J. Athersuch, H. Keun, H. Tang, and J. K. Nicholson, "Quantitative urinalysis of the mercapturic acid conjugates of allyl formate using high-resolution NMR spectroscopy," *Journal of Pharmaceutical and Biomedical Analysis*, vol. 40, pp. 410–416, 2006.

[77] A. Moghe, S. Ghare, B. Lamoreau, M. Mohammad, S. Barve, C. McClain, and S. Joshi-Barve, "Molecular mechanisms of acrolein toxicity: relevance to human disease." *Toxicological sciences : an official journal of the Society of Toxicology*, vol. 143, no. 2, pp. 242–55, 2 2015.

[78] J. Luo, K. Uchida, and R. Shi, "Accumulation of acrolein-protein adducts after traumatic spinal cord injury," *Neurochemical Research*, vol. 30, no. 3, pp. 291–295, 2005.

[79] J. F. Stevens and C. S. Maier, "Acrolein: Sources, metabolism, and biomolecular interactions relevant to human health and disease," *Molecular Nutrition and Food Research*, vol. 52, no. 1, pp. 7–25, 2008.

[80] H. Esterbauer, R. J. Schaur, and H. Zollner, "Chemistry and biochemistry of 4-hydroxynonenal, malonaldehyde and related aldehydes," *Free Radical Biology and Medicine*, vol. 11, no. 1, pp. 81–128, 1 1991.

[81] L. M. Kaminskas, S. M. Pyke, and P. C. Burcham, "Reactivity of hydrazinophthalazine drugs with the lipid peroxidation products acrolein and crotonaldehyde," *Organic & Biomolecular Chemistry*, vol. 2, no. 18, p. 2578, 9 2004.

[82] K. Hamann, G. Nehrt, H. Ouyang, B. Duerstock, and R. Shi, "Hydralazine inhibits compression and acrolein-mediated injuries in ex vivo spinal cord," *Journal of Neurochemistry*, vol. 104, no. 3, pp. 708–718, 2008.

[83] P. L. Wood, M. A. Khan, J. R. Moskal, K. G. Todd, V. A. Tanay, and G. Baker, "Aldehyde load in ischemiareperfusion brain injury: Neuroprotection by neutralization of reactive aldehydes with phenelzine," *Brain Research*, vol. 1122, no. 1, pp. 184–190, 11 2006.

[84] J. Vicente, E. Fuster-Garcia, S. Tortajada, J. M. García-Gómez, N. Davies, K. Natarajan, M. Wilson, R. G. Grundy, P. Wesseling, D. Monleón, B. Celda, M. Robles, and A. C. Peet, "Accurate classification of childhood brain tumours by in vivo1H MRS A multi-centre study," *European Journal of Cancer*, vol. 49, no. 3, pp. 658–667, 2 2013.

[85] S. Ulmer, M. Backens, and F. J. Ahlhelm, "Basic Principles and Clinical Applications of Magnetic Resonance Spectroscopy in Neuroradiology," *Journal of Computer Assisted Tomography*, vol. 40, no. 1, pp. 1–13, 2015.

[86] T. L. Richards, "Proton MR Spectroscopy in Multiple Sclerosis: Value in Establishing Diagnosis, Monitoring Progression, and Evaluating Therapy," *American Journal of Roentgenology*, vol. 57, no. 5, pp. 1073–1078, 1991.

[87] H. Zhu and P. B. Barker, "MR spectroscopy and spectroscopic imaging of the brain." *Methods in molecular biology*, vol. 711, pp. 203–26, 2011.

[88] M. Desseilles, T. Dang-Vu, M. Schabus, V. Sterpenich, P. Maquet, and S. Schwartz, "Neuroimaging insights into the pathophysiology of sleep disorders." *Sleep*, vol. 31, no. 6, pp. 777–94, 6 2008.

[89] D. W. Simon, M. J. McGeachy, H. Bayr, R. S. B. Clark, D. J. Loane, and P. M. Kochanek, "The far-reaching scope of neuroinflammation after traumatic brain injury," *Nature Publishing Group*, vol. 13, no. 3, pp. 171–1911, 2017.

[90] A. Dennis, A. G. Thomas, N. B. Rawlings, J. Near, T. E. Nichols, S. Clare, H. Johansen-Berg, and C. J. Stagg, "An Ultra-High Field Magnetic Resonance Spectroscopy Study of Post Exercise Lactate, Glutamate and Glutamine Change in the Human Brain." *Frontiers in physiology*, vol. 6, no. 351, pp. 1–11, 2015.

[91] E. D. Hall, J. A. Wang, J. M. Bosken, and I. N. Singh, "Lipid peroxidation in brain or spinal cord mitochondria after injury," *Journal of Bioenergetics and Biomembranes*, vol. 48, no. 2, pp. 169–174, 2016.

[92] C. Shao, K. N. Roberts, W. R. Markesbery, S. W. Scheff, and M. A. Lovell, "Oxidative stress in head trauma in aging," *Free Radical Biology and Medicine*, vol. 41, no. 1, pp. 77–85, 2006.

[93] U. EPA ORD NCEA Integrated Risk Information System, "Toxicological Review of Acrolein (CAS No. 107-02-8) (PDF)," Tech. Rep., 2003. [Online]. Available: http://www.epa.gov/iris.

[94] M. A. Ansari, K. N. Roberts, and S. W. Scheff, "Oxidative stress and modification of synaptic proteins in hippocampus after traumatic brain injury." *Free radical biology & medicine*, vol. 45, no. 4, pp. 443–52, 8 2008.

[95] K. Hamann, A. Durkes, H. Ouyang, K. Uchida, A. Pond, and R. Shi, "Critical role of acrolein in secondary injury following ex vivo spinal cord trauma," *Journal of Neurochemistry*, vol. 107, no. 3, pp. 712–721, 2008.

[96] L. Zheng, J. Park, M. Walls, M. Tully, A. Jannasch, B. Cooper, and R. Shi, "Determination of Urine 3-HPMA, a Stable Acrolein Metabolite in a Rat Model of Spinal Cord Injury," *Journal of Neurotrauma*, vol. 30, no. 15, pp. 1334–1341, 2013.

[97] M. Tully, J. Tang, L. Zheng, G. Acosta, R. Tian, L. Hayward, N. Race, D. Mattson, and R. Shi, "Systemic Acrolein Elevations in Mice With Experimental Autoimmune Encephalomyelitis and Patients With Multiple Sclerosis." *Frontiers in neurology*, vol. 9, no. 420, 2018.

[98] D. V. Agoston, A. Shutes-David, and E. R. Peskind, "Brain Injury Biofluid biomarkers of traumatic brain injury," *Brain Injury*, vol. 31, no. 9, pp. 1195–1203, 2017.

[99] K. Kawata, C. Y. Liu, S. F. Merkel, S. H. Ramirez, R. T. Tierney, and D. Langford, "Blood biomarkers for brain injury: What are we measuring?" *Neuroscience and biobehavioral reviews*, vol. 68, pp. 460–473, 2016.

[100] TMIC, "Human Metabolome Database: 1H NMR Spectrum (HMDB41822)," 2014. [Online]. Available: http://www.hmdb.ca/spectra/nmr_one_d/2100

[101] W. Y. Chen, J. Zhang, S. Ghare, S. Barve, C. Mcclain, and S. Joshi-Barve, "Acrolein Is a Pathogenic Mediator of Alcoholic Liver Disease and the Scavenger Hydralazine Is Protective in Mice," *Cellular and Molecular Gastroenterology and Hepatology*, vol. 2, no. 5, pp. 685–700, 2016.

[102] M. R. Willcott, "MestRe Nova," *Journal of the American Chemical Society*, vol. 131, no. 36, p. 13180, 9 2009.

[103] R. Freeman and H. D. W. Hill, "Measurement of Spin Relaxation in Complex Systems The," *The Journal of Chemical Physics*, vol. 51, p. 3367, 1969.

[104] S. K. Vaish, A. Singh, A. K. Singh, and N. K. Mehrotra, "Study of NMR spin lattice relaxation of several aldehydes," Tech. Rep., 2005.

[105] F. Guenneau, P. Mutzenhardt, D. Grandclaude, and D. Canet, "Measurement of Longitudinal and Rotating Frame Relaxation Times through Fully J-Decoupled Homonuclear Spectra," *Journal of Magnetic Resonance*, vol. 140, no. 1, pp. 250–258, 9 1999.

[106] H. J. Reich, "Structure Determination Using NMR," in *Chemistry 605*. University of Wisconsin - Madison, 2017, ch. 8.1 Relaxa, pp. 1–13. [Online]. Available: https://www.chem.wisc.edu/areas/reich/nmr/notes-8-tech-1-relax.pdf

[107] N. Bloembergen, E. M. Purcell, and R. V. Pound, "Relaxation Effects in Nuclear Magnetic Resonance Absorption," *Physical Review*, vol. 73, no. 7, pp. 679–712, 4 1948.

[108] M. G. Stovell, J.-L. Yan, A. Sleigh, M. O. Mada, T. A. Carpenter, P. J. A. Hutchinson, and K. L. H. Carpenter, "Assessing Metabolism and Injury in Acute Human Traumatic Brain Injury with Magnetic Resonance Spectroscopy: Current and Future Applications." *Frontiers in neurology*, vol. 8, no. 426, 2017.

[109] C. Gasparovic, H. Chen, and P. G. Mullins, "Errors in Proton-MRS estimates of brain metabolite concentrations caused by failing to take into account tissue-specific signal relaxation," *NMR in Biomedicine*, vol. 31, no. 6, p. e3914, 6 2018.

[110] M. Wilson, O. Andronesi, M. G. Hospital, P. B. Barker, R. Bartha, A. Bizzi, N. Unit, P. J. Bolan, K. M. Brindle, I.-y. Choi, H. Brain, K. City, C. Cudalbu, U. Dydak, W. Lafayette, U. E. Emir, W. Lafayette, R. G. Gonzalez, M. G. Hospital, S. Gruber, R. Gruetter, R. K. Gupta, A. Heerschap, A. Henning, H. P. Hetherington, P. S. Huppi, R. E. Hurd, S. Radiological, K. Kantarci, M. Clinic, R. A. Kauppinen, D. W. J. Klomp, and R. Kreis, "A Methodological Consensus on Clinical Proton MR Spectroscopy of the Brain : Review and Recommendations," *Magnetic Resonance in Medicine*, vol. 82, no. 2, pp. 527–550, 2019.

[111] S. W. Provencher, "Automatic quantitation of localizedin vivo1H spectra with LCModel," *NMR in Biomedicine*, vol. 14, no. 4, pp. 260–264, 6 2001.

[112] K. G. Harmon, J. A. Drezner, M. Gammons, K. M. Guskiewicz, M. Halstead, S. A. Herring, J. S. Kutcher, A. Pana, M. Putukian, and W. O. Roberts, "American Medical Society for Sports Medicine position statement: concussion in sport," *British Journal of Sports Medicine*, vol. 47, no. 1, pp. 15–26, 2013.

[113] K. Sarmiento, K. E. Thomas, J. Daugherty, D. Waltzman, J. K. Haarbauer-Krupa, A. B. Peterson, T. Haileyesus, and M. J. Breiding, "Emergency Department Visits for Sports- and Recreation-Related Traumatic Brain Injuries Among Children United States, 20102016," *MMWR. Morbidity and Mortality Weekly Report*, vol. 68, no. 10, pp. 237–242, 3 2019.

[114] K. L. O'Connor, M. M. Baker, S. L. Dalton, T. P. Dompier, S. P. Broglio, and Z. Y. Kerr, "Epidemiology of Sport-Related Concussions in High School Athletes: National Athletic Treatment, Injury and Outcomes Network (NATION), 20112012 Through 20132014," *Journal of Athletic Training*, vol. 52, no. 3, pp. 175–185, 3 2017.

[115] "2014-15 High School Athletics Participation Survey," National Federation of State High School Associations, Tech. Rep., 2015. [Online]. Available: http://www.nfhs.org/ParticipationStatics/PDF/2014-15_Participation_Survey_Results.pdf

[116] M. Mccrea, T. Hammeke, G. Olsen, P. Leo, and K. Guskiewicz, "Unreported Concussion in High School Football Players Implications for Prevention," *Clinical Journal of Sport Medicine*, vol. 14, no. 1, pp. 13–17, 2004.

[117] T. B. Meier, B. J. Brummel, R. Singh, C. J. Nerio, D. W. Polanski, and P. S. Bellgowan, "The underreporting of self-reported symptoms following sports-related concussion," *Journal of Science and Medicine in Sport*, vol. 18, no. 5, pp. 507–511, 9 2015. [Online]. Available: http://linkinghub.elsevier.com/retrieve/pii/S1440244014001340

[118] E. Kroshus, B. Garnett, M. Hawrilenko, C. M. Baugh, and J. P. Calzo, "Concussion under-reporting and pressure from coaches, teammates, fans, and parents." *Social science & medicine*, vol. 134, pp. 66–75, 6 2015.

[119] M. Putukian, "Clinical Evaluation of the Concussed Athlete: A View From the Sideline." *Journal of athletic training*, vol. 52, no. 3, pp. 236–244, 3 2017.

[120] T. M. Talavage, E. A. Nauman, E. L. Breedlove, U. Yoruk, A. E. Dye, K. Morigaki, H. Feuer, and L. J. Leverenz, "Functionally-Detected Cognitive Impairment in High School Football Players Without Clinically- Diagnosed Concussion," *Journal of Neurotrauma*, vol. 31, no. 4, pp. 327–338, 2014.

[121] A. L. P. Julian E. Bailes, E. N. Bennet I. Omalu, and and Thomas Talavage, "Role of subconcussion in repetitive mild traumatic brain injury," *Journal of neurosurgery*, vol. 119, no. 5, pp. 1235–1245, 2013.

[122] H. L. Parker, "Traumatic Encephalopathy ('Punch Drunk') of Professional Pugilists." *The Journal of neurology and psychopathology*, vol. 15, no. 57, pp. 20–8, 7 1934.

[123] R. J. Castellani and G. Perry, "Dementia Pugilistica Revisited." *Journal of Alzheimer's disease*, vol. 60, no. 4, pp. 1209–1221, 2017.

[124] B. Omalu, S. DeKosky, R. Minster, M. Kamboh, R. Hamilton, and C. Wecht, "Chronic Traumatic Encephalopathy in a National Football League Player," *Neurosurgery*, vol. 57, no. 1, pp. 128–133, 2005.

[125] A. C. McKee, R. C. Cantu, C. J. Nowinski, E. T. Hedley-Whyte, B. E. Gavett, A. E. Budson, V. E. Santini, H.-S. Lee, C. A. Kubilus, and R. A. Stern, "Chronic Traumatic Encephalopathy in Athletes: Progressive Tauopathy After Repetitive Head Injury," *Journal of Neuropathology & Experimental Neurology*, vol. 68, no. 7, 2009.

[126] A. C. McKee, T. D. Stein, C. J. Nowinski, R. A. Stern, D. H. Daneshvar, V. E. Alvarez, H. S. Lee, G. Hall, S. M. Wojtowicz, C. M. Baugh, D. O. Riley, C. A. Kubilus, K. A. Cormier, M. A. Jacobs, B. R. Martin, C. R. Abraham, T. Ikezu, R. R. Reichard, B. L. Wolozin, A. E. Budson, L. E. Goldstein, N. W. Kowall, and R. C. Cantu, "The spectrum of disease in chronic traumatic encephalopathy," *Brain*, vol. 136, no. 1, 2013.

[127] A. C. Mckee and D. H. Daneshvar, "The neuropathology of traumatic brain injury," *Handbook of Clinical Neurology*, vol. 127, 2015.

[128] A. C. McKee, M. L. Alosco, and B. R. Huber, "Repetitive Head Impacts and Chronic Traumatic Encephalopathy," pp. 529–535, 2016.

[129] M. Saulle, B. D. Greenwald, M. Saulle, and B. D. Greenwald, "Chronic Traumatic Encephalopathy: A Review," *Rehabilitation Research and Practice*, vol. 2012, pp. 1–9, 2012.

[130] B. Omalu, J. Bailes, R. L. Hamilton, M. I. Kamboh, J. Hammers, M. Case, and R. Fitzsimmons, "Emerging Histomorphologic Phenotypes of Chronic Traumatic Encephalopathy in American Athletes," *Neurosurgery*, vol. 69, no. 1, pp. 173–183, 7 2011.

[131] S. P. Broglio, J. J. Sosnoff, S. Shin, X. He, C. Alcaraz, and J. Zimmerman, "Head impacts during high school football: a biomechanical assessment." *Journal of athletic training*, vol. 44, no. 4, pp. 342–9, 2009.

[132] S. P. Broglio, J. T. Eckner, D. Martini, J. J. Sosnoff, J. S. Kutcher, and C. Randolph, "Cumulative head impact burden in high school football." *Journal of neurotrauma*, vol. 28, no. 10, pp. 2069–78, 10 2011. [Online]. Available: http://www.ncbi.nlm.nih.gov/pubmed/21787201http://www.pubmedcentral.nih.gov/articlerender.fcgi?artid=PMC4346237

[133] J. L. Graner, H. S. Levin, T. M. Talavage, E. A. Nauman, and L. J. Leverenz, "the role of Medical imaging in the recharacterization of Mild traumatic Brain injury Using youth sports as a Laboratory," *Frontiers in neurology*, vol. 6, no. 273, 2016.

[134] B. Cummiskey, D. Schiffmiller, T. M. Talavage, L. Leverenz, J. J. Meyer, D. Adams, and E. A. Nauman, "Reliability and accuracy of helmet-mounted and head-mounted devices used to measure head accelerations," *Journal of Sports Engineering and Technology*, vol. 231, no. 2, pp. 1–10, 8 2016.

[135] D. B. Camarillo, P. B. Shull, J. Mattson, R. Shultz, and D. Garza, "An instrumented mouthguard for measuring linear and angular head impact kinematics in American football." *Annals of biomedical engineering*, vol. 41, no. 9, pp. 1939–49, 9 2013.

[136] J. G. Beckwith, R. M. Greenwald, J. J. Chu, J. J. Crisco, S. Rowson, S. M. Duma, S. P. Broglio, T. W. McAllister, K. M. Guskiewicz, J. P. Mihalik, S. Anderson, B. Schnebel, P. G. Brolinson, and M. W. Collins, "Head impact exposure sustained by football players on days of diagnosed concussion." *Medicine and science in sports and exercise*, vol. 45, no. 4, pp. 737–46, 4 2013.

[137] M. Haris, K. Cai, A. Singh, H. Hariharan, and R. Reddy, "In vivo mapping of brain myo-inositol." *NeuroImage*, vol. 54, no. 3, pp. 2079–85, 2 2011.

[138] A. P. Lin, H. J. Liao, S. K. Merugumala, S. P. Prabhu, W. P. Meehan, and B. D. Ross, "Metabolic imaging of mild traumatic brain injury," *Brain Imaging and Behavior*, vol. 6, no. 2, pp. 208–223, 6 2012.

[139] B. L. Miller, R. A. Moats, T. Shonk, T. Ernst, S. Woolley, and B. D. Ross, "Alzheimer disease: depiction of increased cerebral myo-inositol with proton MR spectroscopy." *Radiology*, vol. 187, no. 2, pp. 433–7, 5 1993.

[140] P. Kapeller, S. Ropele, C. Enzinger, T. Lahousen, S. Strasser-Fuchs, R. Schmidt, and F. Fazekas, "Discrimination of white matter lesions and multiple sclerosis plaques by short echo quantitative 1Hmagnetic resonance spectroscopy," *Journal of Neurology*, vol. 252, no. 10, pp. 1229–1234, 10 2005.

[141] J. R. Moffett, B. Ross, P. Arun, C. N. Madhavarao, and A. M. A. Namboodiri, "N-Acetylaspartate in the CNS: from neurodiagnostics to neurobiology." *Progress in neurobiology*, vol. 81, no. 2, pp. 89–131, 2 2007.

[142] E. Danielson and B. Ross, *Magnetic Resonance Spectroscopy Diagnosis of Neurological Diseases*, 1st ed. New York: CRC Press/Taylor and Francis Group, 1999.

[143] M. H. Baslow, "N-acetylaspartate in the vertebrate brain: metabolism and function." *Neurochemical research*, vol. 28, no. 6, pp. 941–53, 6 2003.

[144] S. Signoretti, A. Marmarou, B. Tavazzi, G. Lazzarino, A. Beaumont, and R. Vagnozzi, "N-Acetylaspartate Reduction as a Measure of Injury Severity and Mitochondrial Dysfunction Following Diffuse Traumatic Brain Injury," *Journal of Neurotrauma*, vol. 18, no. 10, pp. 977–991, 10 2001.

[145] L. M. Sanders and S. H. Zeisel, "Choline: Dietary Requirements and Role in Brain Development." *Nutrition today*, vol. 42, no. 4, pp. 181–186, 2007.

[146] P. T. Francis, "The interplay of neurotransmitters in Alzheimer's disease." *CNS spectrums*, vol. 10, no. 11 Suppl 18, pp. 6–9, 11 2005.

[147] J. Jia, J. Jia, W. Zhou, M. Xu, C. Chu, X. Yan, and Y. Sun, "Differential acetylcholine and choline concentrations in the cerebrospinal fluid of patients with Alzheimer's disease and vascular dementia." *Chinese medical journal*, vol. 117, no. 8, pp. 1161–4, 8 2004.

[148] S. Marino, E. Zei, M. Battaglini, C. Vittori, A. Buscalferri, P. Bramanti, A. Federico, and N. De Stefano, "Acute metabolic brain changes following traumatic brain injury and their relevance to clinical severity and outcome." *Journal of neurology, neurosurgery, and psychiatry*, vol. 78, no. 5, pp. 501–507, 5 2007.

[149] I. K. Koerte, A. P. Lin, M. Muehlmann, S. Merugumala, H. Liao, T. Starr, D. Kaufmann, M. Mayinger, D. Steffinger, B. Fisch, S. Karch, F. Heinen, B. Ertl-Wagner, M. Reiser, R. A. Stern, R. Zafonte, and M. E. Shenton, "Altered Neurochemistry in Former Professional Soccer Players without a History of Concussion." *Journal of neurotrauma*, vol. 32, no. 17, pp. 1287–93, 9 2015.

[150] W. M. Brooks, S. D. Friedman, and C. Gasparovic, "Magnetic Resonance Spectroscopy in Traumatic Brain Injury," *Journal of Head Trauma Rehabilitation*, vol. 16, no. 2, pp. 149–164, 1986.

[151] R. H. Andres, A. D. Ducray, U. Schlattner, T. Wallimann, and H. R. Widmer, "Functions and effects of creatine in the central nervous system," *Brain Research Bulletin*, vol. 76, no. 4, pp. 329–343, 7 2008.

[152] C. Gasparovic, R. Yeo, M. Mannell, J. Ling, R. Elgie, J. Phillips, D. Doezema, and A. R. Mayer, "Neurometabolite Concentrations in Gray and White Matter in Mild Traumatic Brain Injury: An 1 HMagnetic Resonance Spectroscopy Study." [Online]. Available: https://www.liebertpub.com/doi/pdf/10.1089/neu.2009.0896

[153] P. G. Sullivan, J. D. Geiger, M. P. Mattson, and S. W. Scheff, "Dietary supplement creatine protects against traumatic brain injury," *Annals of Neurology*, vol. 48, no. 5, pp. 723–729, 11 2000.

[154] H. Tapiero, G. Mathé, P. Couvreur, and K. D. Tew, "II. Glutamine and glutamate." *Biomedicine & pharmacotherapy = Biomedecine & pharmacotherapie*, vol. 56, no. 9, pp. 446–57, 11 2002.

[155] L. G. Kaiser, N. Schuff, N. Cashdollar, and M. W. Weiner, "Age-related glutamate and glutamine concentration changes in normal human brain: 1H MR spectroscopy study at 4 T," *Neurobiology of aging*, vol. 26, no. 5, p. 665, 5 2005.

[156] A. K. Barbey, M. Koenigs, and J. Grafman, "Dorsolateral prefrontal contributions to human working memory," *Cortex*, vol. 49, no. 5, pp. 1195–1205, 5 2013.

[157] A. K. Barbey, R. Colom, and J. Grafman, "Dorsolateral prefrontal contributions to human intelligence." *Neuropsychologia*, vol. 51, no. 7, pp. 1361–9, 6 2013.

[158] N. Steinbeis, B. C. Bernhardt, and T. Singer, "Impulse Control and Underlying Functions of the Left DLPFC Mediate Age-Related and Age-Independent Individual Differences in Strategic Social Behavior," *Neuron*, vol. 73, no. 5, pp. 1040–1051, 3 2012.

[159] J. N. Sanes and J. P. Donoghue, "Plasticity and Primary Motor Cortex," *Annual Review of Neuroscience*, vol. 23, no. 1, pp. 393–415, 3 2000.

[160] M. Jeong, Y. Kim, J. Kim, D. D. Ferrante, P. P. Mitra, P. Osten, and D. Kim, "Comparative three-dimensional connectome map of motor cortical projections in the mouse brain," *Scientific Reports*, vol. 6, no. 1, p. 20072, 4 2016.

[161] W. Block, J. Karitzky, F. Träber, C. Pohl, E. Keller, R. R. Mundegar, R. Lamerichs, H. Rink, F. Ries, H. H. Schild, and F. Jerusalem, "Proton Magnetic Resonance Spectroscopy of the Primary Motor Cortex in Patients With Motor Neuron Disease," *Archives of Neurology*, vol. 55, no. 7, p. 931, 7 1998.

[162] C. Annweiler, O. Beauchet, R. Bartha, J. L. Wells, M. J. Borrie, V. Hachinski, and M. Montero-Odasso, "Motor cortex and gait in mild cognitive impairment: a magnetic resonance spectroscopy and volumetric imaging study," *Brain*, vol. 136, no. 3, pp. 859–871, 3 2013.

[163] L. C. Henry, S. Tremblay, Y. Boulanger, D. Ellemberg, and M. Lassonde, "Neurometabolic Changes in the Acute Phase after Sports Concussions Correlate with Symptom Severity," *Journal of Neurotrauma*, vol. 27, no. 1, pp. 65–76, 1 2010.

[164] E. McCuen, D. Svaldi, K. Breedlove, N. Kraz, B. Cummiskey, E. L. Breedlove, J. Traver, K. F. Desmond, R. E. Hannemann, E. Zanath, A. Guerra, L. Leverenz, T. M. Talavage, and E. A. Nauman, "Collegiate women's soccer players suffer greater cumulative head impacts than their high school counterparts," *Journal of Biomechanics*, vol. 48, no. 13, pp. 3720–3723, 10 2015.

[165] M. Wilson, G. Reynolds, R. A. Kauppinen, T. N. Arvanitis, and A. C. Peet, "A constrained least-squares approach to the automated quantitation of in vivo 1 H magnetic resonance spectroscopy data," *Magnetic Resonance in Medicine*, vol. 65, no. 1, pp. 1–12, 1 2011.

[166] R. W. Cox, "AFNI: software for analysis and visualization of functional magnetic resonance neuroimages." *Computers and biomedical research, an international journal*, vol. 29, no. 3, pp. 162–73, 6 1996.

[167] StataCorp, "Stata Statistical Software: Release 15," College Station, TX, 2017.

[168] W. Eddings and Y. Marchenko, "Diagnostics for Multiple Imputation in Stata," *Stata Journal*, vol. 12, pp. 353–367, 2012.

[169] S. Shapiro and M. Wilks, "An Analysis of Variance Test for Normality," *Biometrika*, vol. 52, pp. 591–611, 1965.

[170] M. Barltett, "Properties of Sufficiency and Statistical Tests," *Proceedings of the Royal Society Series A*, vol. 160, pp. 268–282, 1937.

[171] W. Kruskal and W. Wallis, "Use of Ranks in One-Criterion Variance Analysis," *Journal of the American Statistical Association*, vol. 47, pp. 583–621, 1952.

[172] C. Bonferroni, "Teoria Statistica Delle Classi e Calcolo Delle Probabilitia," *R Istituto Superiore di Scienze Economiche e Commerciali di Firenze*, vol. 8, pp. 3–62, 1936.

[173] H. Mann, "On a Test of Whether one of Two Random Varaibles is Stochastically Larger than the Other," *Annals of Mathematical Statistics*, vol. 18, no. 1, pp. 50–60, 1947.

[174] Y. Benjamini and Y. Hochberg, "Controlling the False Discovery Rate: A Practical and Powerful Approach to Multiple Testing on JSTOR," *Journal of the Royal Society of Statistics Series B*, vol. 57, no. 1, pp. 298–300, 1995.

[175] D. Cook, "Detection of Influential Observations in Linear Regression," *Technometrics*, vol. 19, no. 1, pp. 15–18, 1977.

[176] B.-y. Choe, T.-S. Suh, K.-H. Choi, K.-S. Shinn, C.-K. Park, and J.-K. Kang, "Neuronal dysfunction in patients with closed head injury evaluated," *Investigative radiology*, vol. 30, no. 8, pp. 502–506, 1995.

[177] L. Xu, J. V. Nguyen, M. Lehar, A. Menon, E. Rha, J. Arena, J. Ryu, N. Marsh-Armstrong, C. R. Marmarou, and V. E. Koliatsos, "Repetitive mild traumatic brain injury with impact acceleration in the mouse: Multifocal axonopathy, neuroinflammation, and neurodegeneration in the visual system," *Experimental Neurology*, vol. 275, 2016.

[178] M. U. Schuhmann, D. Stiller, M. Skardelly, J. Bernarding, P. M. Klinge, A. Samii, M. Samii, and T. Brinker, "Metabolic Changes in the Vicinity of Brain Contusions: A Proton Magnetic Resonance Spectroscopy and Histology Study," *Journal of Neurotrauma*, vol. 20, no. 8, pp. 725–743, 8 2003.

[179] G. Manley, A. J. Gardner, K. J. Schneider, K. M. Guskiewicz, J. Bailes, R. C. Cantu, R. J. Castellani, M. Turner, B. D. Jordan, C. Randolph, J. Dvořák, K. A. Hayden, C. H. Tator, G. Manley, G. Aj, and S. Kj, "A systematic review of potential long-term effects of sport-related concussion," *British Journal of Sports Medicine*, vol. 51, no. 12, pp. 969–977, 2017.

[180] T. McAllister and M. McCrea, "Long-Term Cognitive and Neuropsychiatric Consequences of Repetitive Concussion and Head-Impact Exposure," *Journal of athletic training*, vol. 52, no. 3, pp. 309–317, 2017.

[181] Y. Sophie Su, A. Veeravagu, and G. Grant, *Neuroplasticity after Traumatic Brain Injury*. CRC Press/Taylor and Francis Group, 2016. [Online]. Available: http://www.ncbi.nlm.nih.gov/pubmed/26583189

[182] B. Kolb, R. Mychasiuk, P. Williams, and R. Gibb, "Brain plasticity and recovery from early cortical injury," *Developmental Medicine & Child Neurology*, vol. 53, no. s4, pp. 4–8, 9 2011.

[183] S. T. Carmichael, "Plasticity of Cortical Projections after Stroke," *The Neuroscientist*, vol. 9, no. 1, pp. 64–75, 2 2003.

[184] D. F. Meaney, B. Morrison, and C. Dale Bass, "The mechanics of traumatic brain injury: a review of what we know and what we need to know for reducing its societal burden." *Journal of biomechanical engineering*, vol. 136, no. 2, p. 021008, 2 2014.

[185] A. L. Zhang, D. C. Sing, C. M. Rugg, B. T. Feeley, and C. Senter, "The Rise of Concussions in the Adolescent Population." *Orthopaedic journal of sports medicine*, vol. 4, no. 8, p. 2325967116662458, 8 2016.

[186] D. E. Kimbler, M. Murphy, and K. M. Dhandapani, "Concussion and the adolescent athlete." *The Journal of neuroscience nursing : journal of the American Association of Neuroscience Nurses*, vol. 43, no. 6, pp. 286–90, 12 2011.

[187] R. W. Daniel, S. Rowson, and S. M. Duma, "Head Impact Exposure in Youth Football: Middle School Ages 1214 Years," *Journal of Biomechanical Engineering*, vol. 136, no. 9, p. 094501, 7 2014.

[188] A. R. Peterson, A. J. Kruse, S. M. Meester, T. S. Olson, B. N. Riedle, T. G. Slayman, T. J. Domeyer, J. E. Cavanaugh, and M. K. Smoot, "Youth Football Injuries: A Prospective Cohort." *Orthopaedic journal of sports medicine*, vol. 5, no. 2, p. 2325967116686784, 2 2017.

[189] T. A. Maugans, C. Farley, M. Altaye, J. Leach, and K. M. Cecil, "Pediatric sports-related concussion produces cerebral blood flow alterations." *Pediatrics*, vol. 129, no. 1, pp. 28–37, 1 2012.

[190] B. L. Brooks, C. D. McKay, M. Mrazik, K. M. Barlow, W. H. Meeuwisse, and C. A. Emery, "Subjective, but not objective, lingering effects of multiple past concussions in adolescents." *Journal of neurotrauma*, vol. 30, no. 17, pp. 1469–75, 9 2013.

[191] R. Mannix, G. L. Iverson, B. Maxwell, J. E. Atkins, R. Zafonte, and P. D. Berkner, "Multiple prior concussions are associated with symptoms in high school athletes." *Annals of clinical and translational neurology*, vol. 1, no. 6, pp. 433–8, 6 2014.

[192] A. M. Karlin, "Concussion in the Pediatric and Adolescent Population: Different Population, Different Concerns," *PM&R*, vol. 3, no. 10S2, pp. S369–S379, 10 2011.

[193] B. L. Bartnik-Olson, B. Holshouser, H. Wang, M. Grube, K. Tong, V. Wong, and S. Ashwal, "Impaired Neurovascular Unit Function Contributes to Persistent Symptoms after Concussion: A Pilot Study," *Journal of Neurotrauma*, vol. 31, no. 17, pp. 1497–1506, 9 2014.

[194] K. Abbas, T. E. Shenk, V. N. Poole, E. L. Breedlove, L. J. Leverenz, E. A. Nauman, T. M. Talavage, and M. E. Robinson, "Alteration of Default Mode Network in High School Football Athletes Due to Repetitive Subconcussive Mild Traumatic Brain Injury: A Resting-State Functional Magnetic Resonance Imaging Study," *Brain Connectivity*, vol. 5, no. 2, pp. 91–101, 3 2015.

[195] P. J. W. Pouwels, K. Brockmann, B. Kruse, B. Wilken, M. Wick, F. Hanefeld, and J. Frahm, "Regional Age Dependence of Human Brain Metabolites from Infancy to Adulthood as Detected by Quantitative Localized Proton MRS," *Pediatric Research*, vol. 46, no. 4, p. 474, 10 1999.

[196] A. Pfefferbaum, E. Adalsteinsson, D. Spielman, E. V. Sullivan, and K. O. Lim, "In vivo spectroscopic quantification of theN-acetyl moiety, creatine, and choline from large volumes of brain gray and white matter: Effects of normal aging," *Magnetic Resonance in Medicine*, vol. 41, no. 2, pp. 276–284, 2 1999.

[197] R. Kreis, T. Ernst, and B. D. Ross, "Development of the human brain:In vivo quantification of metabolite and water content with proton magnetic resonance spectroscopy," *Magnetic Resonance in Medicine*, vol. 30, no. 4, pp. 424–437, 10 1993.

[198] S. Blüml and A. Panigrahy, *Magnetic Resonance Spectroscopy: Basics*, 2013.

[199] S. Blüml, "Metabolites of Proton Magnetic Resonance Spectroscopy and Normal Age-Dependent Changes," pp. 25–38, 2013. [Online]. Available: https://link.springer.com/chapter/10.1007%2F978-1-4419-5864-8_3

[200] M. C. Uytun, "Development Period of Prefrontal Cortex," in *Prefrontal Cortex*. InTechOpen, 10 2018, pp. 3–22. [Online]. Available: http://www.intechopen.com/books/prefrontal-cortex/development-period-of-prefrontal-cortex

[201] S. B. Johnson, R. W. Blum, and J. N. Giedd, "Adolescent maturity and the brain: the promise and pitfalls of neuroscience research in adolescent health policy." *The Journal of adolescent health : official publication of the Society for Adolescent Medicine*, vol. 45, no. 3, pp. 216–21, 9 2009.

[202] M. Brown and J. Bussell, "Medication Adherence: WHO Cares?" *Mayo Clinical Proceedings*, vol. 86, no. 4, pp. 304–314, 2011.

[203] J. Beena and J. Jose, "Patient medication adherence: measures in daily practice." *Oman medical journal*, vol. 26, no. 3, pp. 155–9, 5 2011.

[204] L. Solorio and A. A. Exner, "Effect of the Subcutaneous Environment on Phase-Sensitive in Situ-Forming Implant Drug Release, Degradation, and Microstructure," *Journal of Pharmaceutical Sciences*, vol. 104, no. 12, pp. 4322–4328, 2015. [Online]. Available: http://dx.doi.org/10.1002/jps.24673

[205] L. Solorio, A. M. Olear, J. I. Hamilton, R. B. Patel, A. C. Beiswenger, J. E. Wallace, H. Zhou, and A. A. Exner, "Noninvasive characterization of the effect of varying PLGA molecular weight blends on In Situ forming implant behavior using ultrasound imaging," *Theranostics*, vol. 2, no. 11, pp. 1064–1077, 2012.

[206] L. Solorio, B. M. Babin, R. B. Patel, J. Mach, N. Azar, and A. A. Exner, "Noninvasive characterization of in situ forming implants using diagnostic ultrasound," *Journal of Controlled Release*, vol. 143, no. 2, pp. 183–190, 4 2010.

[207] R. B. Patel, L. Solorio, H. Wu, T. Krupka, and A. A. Exner, "Effect of injection site on in situ implant formation and drug release in vivo." *Journal of controlled release*, vol. 147, no. 3, pp. 350–8, 11 2010.

[208] M. D. Krebs, K. A. Sutter, A. S. P. Lin, R. E. Guldberg, and E. Alsberg, "Injectable poly(lactic-co-glycolic) acid scaffolds with in situ pore formation for tissue engineering." *Acta biomaterialia*, vol. 5, no. 8, pp. 2847–59, 10 2009.

A. ANALYZING DIFFUSIVITY PROFILES OF *IN SITU* FORMING IMPLANTS USING DIFFUSION-WEIGHTED IMAGING

A.1 Introduction to *In Situ* Forming Implants

Medication effectiveness relies on patient adherence to a given treatment regimen. Often, patients do not adhere to the temporal guidelines set by their physicians and treatments therefore remain less effective. Up to 50% of patients do not take their medications at their effective doses [202, 203]. This can lead to a host of problems including medication waste, disease progression, reduced treatment efficacy, increased hospital visits, and increased morbidity [202, 203]. Efforts are being made to combat the lack of medication adherence and improve patient outcomes via elimination of complex oral treatment regimens. *In situ* forming implants (ISFIs) are one approach [37]. ISFIs are composed of biodegradable polymers of specific molecular weight; allowing for flexibility in design. Drug is mixed with the biodegradable polymer (in liquid form) and injected into a specific tissue.

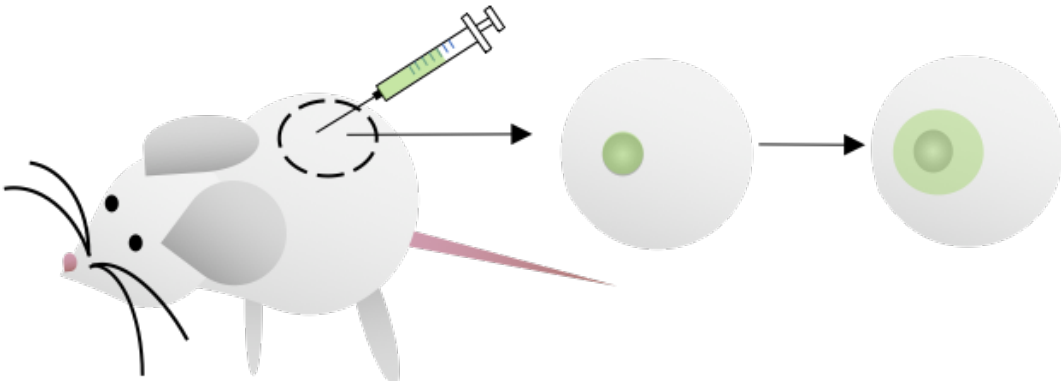

Fig. A.1. Depiction of ISFI injection and release over time.

Once the solution makes contact with the aqueous tissue environment, the polymer spontaneously forms into a small, drug-eluting sphere (Figure 5.1). Over time, drug inside the ISFI exchanges with water in the aqueous environment - thereby providing a dose of medication. ISFIs can be engineered to deliver a specific dose of medication over a desired time course (from days to weeks). The release profiles of ISFIs have been studied extensively *in vitro* and *ex vivo*; however, these results may not reflect how release is occurring *in vivo*. To better understand the release behaviors of ISFIs *in vivo*, various techniques have been attempted. One example is the use of ultrasound imaging. Ultrasound has proven useful for obtaining information on implant structure, drug characteristics, and precipitation of polymer from the ISFI [204–207]. However, there are limitations of this technique in that it can only provide structural information. Another method is micro-CT which can capture high resolution images of ISFI pore size *ex vivo* [208]. Again, this method is limited in its ability to only obtain structural information. Therefore, there exists a gap in deriving functional information regarding drug release dynamics *in vivo*.

Diffusion-weighted imaging (DWI) (as discussed in section 1.2) can be applied to study the diffusion of water in a specific ROI over time *in vivo*. Due to the inherent ability of ISFIs to exchange drug with water in the aqueous environment, is is possible to study the degree of water infiltration, or diffusivity into the ISFI, over time. This novel application of DWI has potential to characterize diffusivity *in vivo*, over time and improve ISFI design. Ultimately, this can lead to improved drug delivery and subsequent medication effectiveness, as well as improved patient outcomes by eliminating the issues associated with medication adherence. The following methods describe DWI analysis of ISFIs which were synthesized for *in vitro*, phantom (*ex vivo* and *in vivo* experiments.

A.1.1 Methods: *In Vitro* and Phantom *Ex Vivo* Experimental Design

Materials

Poly-(lactic-co-glycolic) acid (PLGA; biodegradable polymer) with molecular weights of 15 kDa (2A) and 52 kDa (4A) were obtained from Akina Inc. and Evonik Industries, respectively. N-methyl-2-pyrrolidine (NMP; buffer) was obtained from Fisher Scientific. Mock drug, fluorescein, was obtained from Acros Organics (courtesy Luis Solorio).

In Vitro Polymer Synthesis and Analysis

PLGA, NMP, and fluorescein were combined in a 39:60:1 ratio. Fluorescein and NMP were first combined. Then, PLGA was added to the dissolved into the solution.

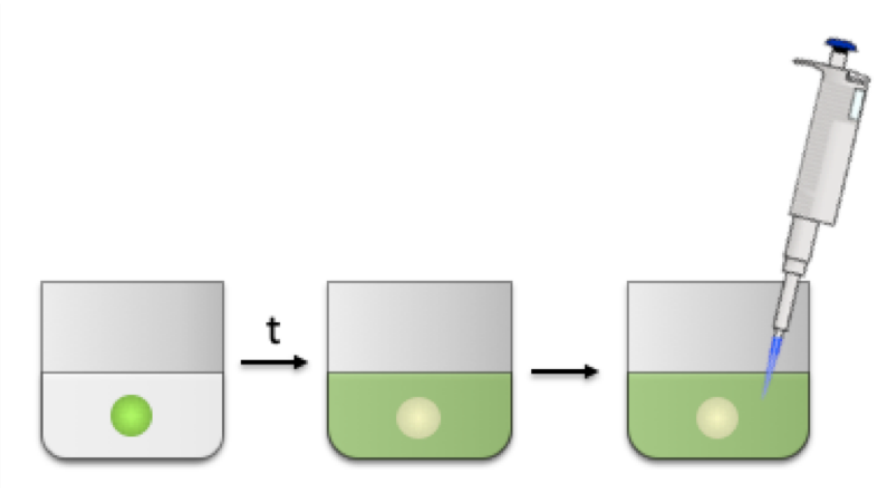

Fig. A.2. Determination of drug release *in vitro*. The bath solution was replaced following each collection. Samples were taken from the bath solution at the following time points: 0.25, 0.5, 1, 2, 4, and 6 hours; 1, 2, 3, 4, 5, 6, 7, 10, 14, 17, and 21 days.

The final solution is referred to as the ISFI solution (PLGA + NMP + fluorescein). Sixty μL of ISFI solution was pipetted into 10 mL of phosphate-buffered saline (PBS) which was continuously stirred. When the ISFI solution contacts the PBS (aqeuous

solution), a small sphere (3 mm) spontaneously forms, enveloping the mock drug which is was contained in the ISFI solution. To quantify drug release, samples were taken from the PBS bath solution between 0.25 hours and 21 days (Figure 5.2). The bath solution was replaced after each sample collection and the fluorescence of each sample was determined using a SpectraMax M5 microplate reader. Data were cumulatively summed to obtain quantification of release over time (courtesy Kelsey Hopkins).

In Vitro DWI Protocol

A 3D printed apparatus was designed to center the ISFIs in the 40 mL phantom bottle (Figure 5.3). Proper centering of the ISFI is critical for image quality.

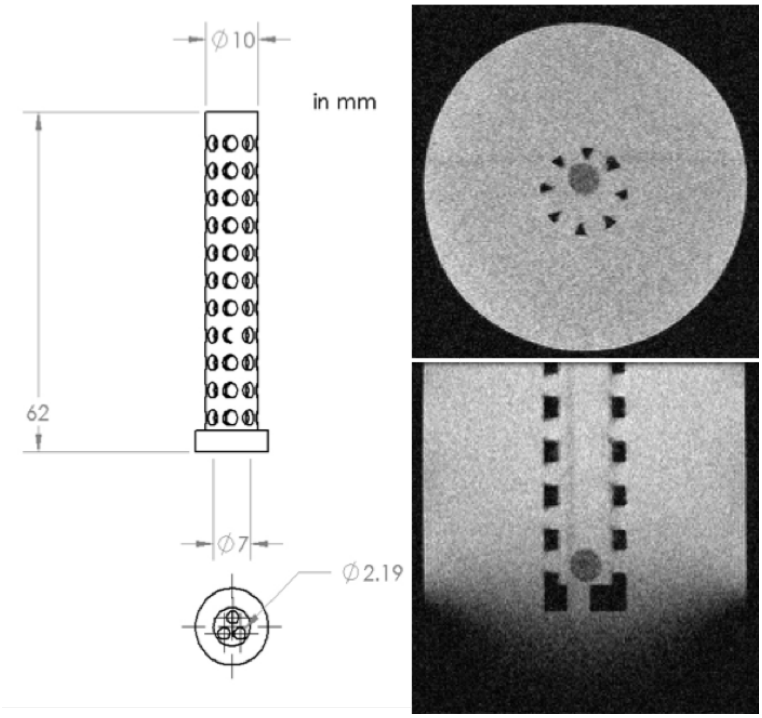

Fig. A.3. 3D printed apparatus designed to fit in a 40 mL bottle and center the ISFI. The ISFI can be seen centered of the bottle.

Imaging was conducted using a Bruker BioSpec 70/30 USR 7 T Pre-Clinical MRI system and a Bruker RF RES 300 ^{1}H 075/040 QSN TR rat head/mouse body volume coil. A standard DWI-SE was used for data collection (TE = 17.5 ms, TR = 2500 ms, FOV = 35mm^2, slice thickness = 0.80 mm, b-value = 0,1000 s/mm^2, time = 8:00 minutes). Prior to DWI-SE, localizer and multislice localizer protocols were run to achieve proper slice placement and the number of slices varied depending on the diameter of the ISFI. Imaging was conducted at time points matching the *in vitro* release experiments (0.25, 0.5, 1, 2, 4, 6, 24, 48, 72, 96, 120, 144, 168, 240, 336, 408, and 504 hours). ISFIs for each time point were synthesized and imaged in triplicate. Each time point had a corresponding set of ISFIs and no ISFI was imaged more than once.

In Vitro DWI Analysis

Following data collection, ADC was calculated for each ISFI at each time point and corresponding ADC maps were generated. Two methods were then used to determine the mean diffusivity (MD) of the ISFIs. The first was accomplished using a custom Matlab code for manual ROI selection (courtesy of Xin Li). Here, ROIs were manually selected by two researchers in triplicate. The average was taken across selections and users to determine the global MD (i.e. the MD of the entire ISFI ROI). The second method used automatic segmentation to threshold out regions with the highest diffusivity (i.e regions containing free water; MD = 2.0 mm^2/s). The resulting MD corresponded to polymer-containing portions of the ISFI. Combining both methods gives unique quantitative information regarding both global and polymer-only regions of the ISFI.

In addition to these methods, further analyses were completed to obtain supplemental functional information. First, a custom Matlab code was developed to perform a radial analysis of MD (courtesy of Xin Li). Concentric rings (1 pixel thick) were used to calculate MD from the outside region of the ISFI, inward. Due to variations

in ISFI diameter, pixel dimensions were normalized on a scale of 0 to 1 with the center defined as 0 and the outermost shell defined as 1. This method provided unique spatial information regarding ISFI MD at various radii.

In Vitro Scanning Electron Microscopy

Scanning Electron Microscopy (SEM) was conducted following each imaging session to obtain fine resolution images. ISFIs were freeze-fractured with dry ice, lyophilized, and mounted to aluminum stubs for imaging. Imaging was performed using a FEI NovaNanoSEM and a Quanta 3D FEG SEM. ImageJ was used to evaluate the microstructure of the ISFIs: shell thickness and pore diameter (courtesy Kelsey Hopkins).

A.1.2 Methods: *In Vivo* Experimental Design

Animal Preparation

All animal studies were performed following protocols approved by the Purdue Animal Care and Use Committee. Three 4-week old male C57BL/6 WT mice were bred from mice (Jackson Laboratory). ISFIs were prepared following procedures as outlined in "Polymer Synthesis and Analysis"; however, the ISFI solution was now injected into mice. Based on results from phantom experiments, only the 4A polymer was used for *in vivo* work. Mice were anesthetized with 1.5% isoflurane and an oxygen flow rate of 2 L/min. Fur was trimmed and prepped with iodine and alcohol. 100 μL of ISFI solution was loaded into a 23-gauge needle and injected subcutaneously. Two injections were made in each mouse - one above the right and left flank - equating to six ROIs.

In Vivo DWI Protocol

Based on results from phantom experiments, only a subset of time points were selected: 1, 6, 24, 72, and 120 hours post-injection. Mice were imaged at each time point and were anesthetized with 2.5% isoflurane and an oxygen flow rate of 250 mL/minute. Respiration rates were monitored using the Monitoring and Gating System from Small Animal Instrument, Inc. (SAII). Adjustments to the rate of isoflurane administration were altered to maintain a respiration rate of 60 breathes/minute. Additional precautions were taken to maintain internal body temperature (26°) and prevent eye abrasions. A Bruker BioSpec 70/30 USR 7 T Preclinical MRI system and Bruker RF RES 300 ^{1}H 075/040 QSN TR rat head/mouse body volume coil were used for *in vivo* MR imaging. A standard DWI-SE sequence was used (TE = 17.5 ms, TR = 2500 ms, FOV = 30 mm^2, slice thickness = 0.80 mm, b = 0,1000 s/mm^2, time = 8:00 minutes). Prior to DWI-SE, localizer and multislice localizer protocols were run to achieve proper slice placement. diameter of the ISFI. Again, the number of slices varied depending on the diameter of the ISFI. Respirations were triggered so image acquisition only occurred between breathes. Following imaging, mice were injected with 0.5 mL of warm saline and kept on a heating pad (37°) for optimal recovery. After the 120 hour time point, mice were euthanized using CO_2 gas, followed by cervical dislocation. ISFIs were extracted from the tissue and prepared for SEM analysis.

In Vivo DWI Analysis

DWI ADC maps were generated as described in "*In Vitro* DWI Analysis". Because *in vivo* imaging results in higher levels of noise, it was necessary to first localize the DWI ROI using the multislice localizer image. This was accomplished by overlaying the higher resolution localizer image with the lower resolution DWI ADC map. In addition, tissue constraints caused the ISFIs to disfigure; for this reason, only manual ROI selection for MD quantification was performed. ROIs were selected in triplicate

by two researchers and the resulting MDs were averaged across selections and users. Each slice was analyzed and slices where there was no visible sign of the ISFI were discluded. It was observed that the cross-sectional ISFI area, and corresponding MD, was different for each slice. For this reason, the average MD across all slices was taken and reported as the final MD value for a given ISFI.

Statistical Analysis

ANOVA with Tukey's multiple comparison correction was used to test for significantly different MDs across time points ($\alpha = 0.05$). A two-sample t-test was used to test for significant differences between ISFIs at equal time points ($\alpha = 0.05$) (courtesy Kelsey Hopkins). Sample sizes (n) were as follows:

Cumulative Release (*in vitro*): n = 5

Phantom (*ex vivo*): n = 3 (3 ISFIs/time point)

In Vivo : n = 6 (2 ISFIs/mouse)

A.1.3 Results

In Vitro Cumulative Drug Release

Cumulative drug release from *in vitro* experimentation was plotted against time (Figure 5.4). 4A and 2A ISFIs showed distinct patterns of release. 2A had a significantly slower burst release phase (0.25-24 hours) compared to 4A. Additionally, 2A had a significantly slower diffusion-facilitated release phase (24-68 hours) compared with 4A. While not significant, 2A showed markedly higher degradation-phase release (240 hours - 504 hours) versus 4A. This *in vitro* data will be used for additional analysis of *in vitro* versus *in vivo* ISFI behavior. Diffusion-facilitated release of 4A was significantly higher than that of 2A.

Release	2A	4A
Burst (%)	26.2±3.8	48.3±5.3
Diffusion (%/day)	4.3±2.6	1.8±1.6
Degradation (%/day)		2.6±0.8

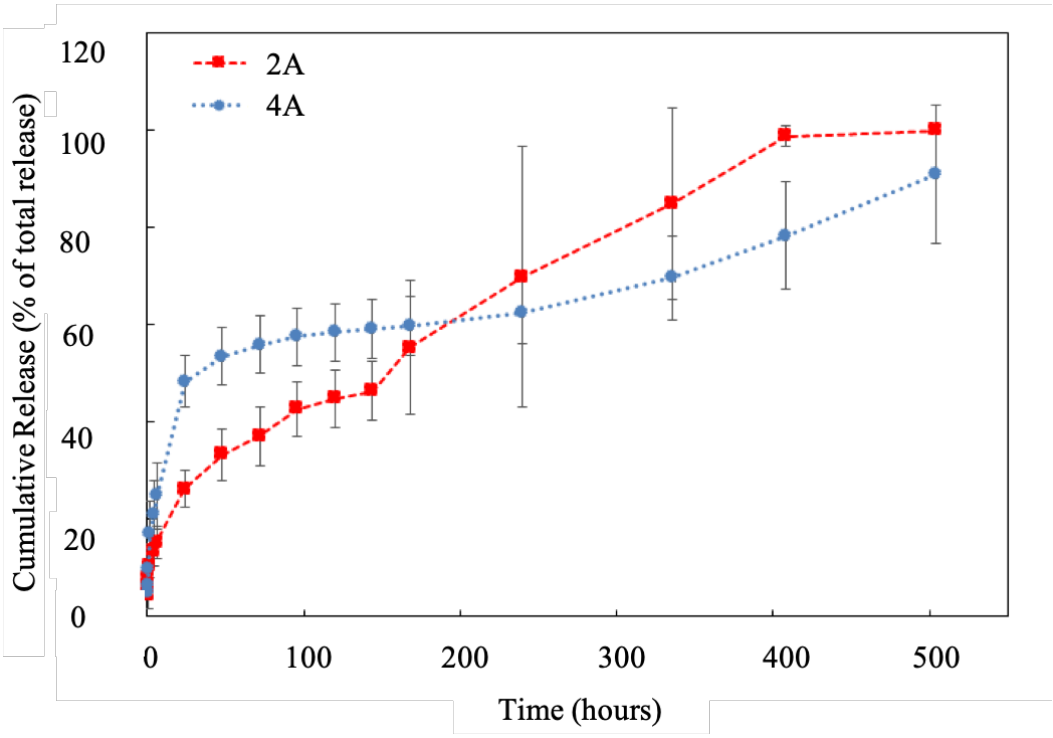

Fig. A.4. Plot of drug release over time for 2A and 4A ISFIs with corresponding burst, diffusion, and degradation release percentages. Values are reported as percentages of total release.

Phantom (*Ex Vivo*) DWI and ISFI Characterization

ADC maps were generated for each ISFI at each time point (three/time point) and one representative ISFI per time point is shown in Figure 5.5. Regions in blue indicate regions of low apparent diffusion and regions in red indicate high apparent diffusion. Spatiotemporal changes in ADC were observed for both 4A and 2A. At 24 hours, there was a marked increase in ADC for both 2A and 4A. At three days, ADC for 2A was much higher than that for 4A, suggesting a faster rate of diffusion-facilitated

release. By day 17, 2A was completely degraded and the ISFI was no longer visible. Comparatively, 4A did not degrade fully until day 21. Additionally, a distinct region of high ADC can be seen from 15 minutes to six hours for both 2A and 4A. This region is referred to as the shell of the ISFI and is the location for water-drug exchange. By 24 hours, however, this region changed dynamically. Here, the interior portion of the ISFI exhibited a much higher ADC, indicative of the burst-release phase.

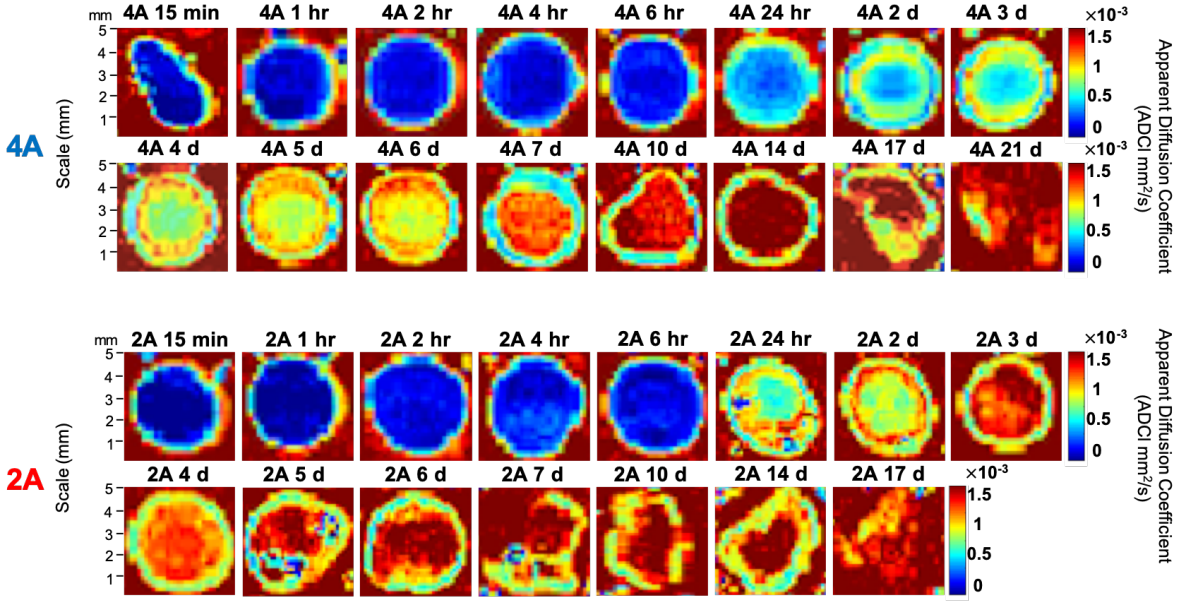

Fig. A.5. ADC maps of 4A and 2A ISFIs between 0.25 hours and 21 days post-synthesis. Regions in blue are indicative of low diffusion and regions in red are indicative of high diffusion.

The interior portion of the ISFI changed dynamically from 24 hours to 17 days post-synthesis, with increasing ADC and changes in shell diffusivity. This observation can be related to the process of continuous water-drug exchange and degrading PLGA.

Next, MD was calculated from the ADC maps and a four-parameter logistic curve was used to fit MD over time for 4A (courtesy Kelsey Hopkins). First, a comparison of global MD and polymer-only MD was completed (Figure 5.6).

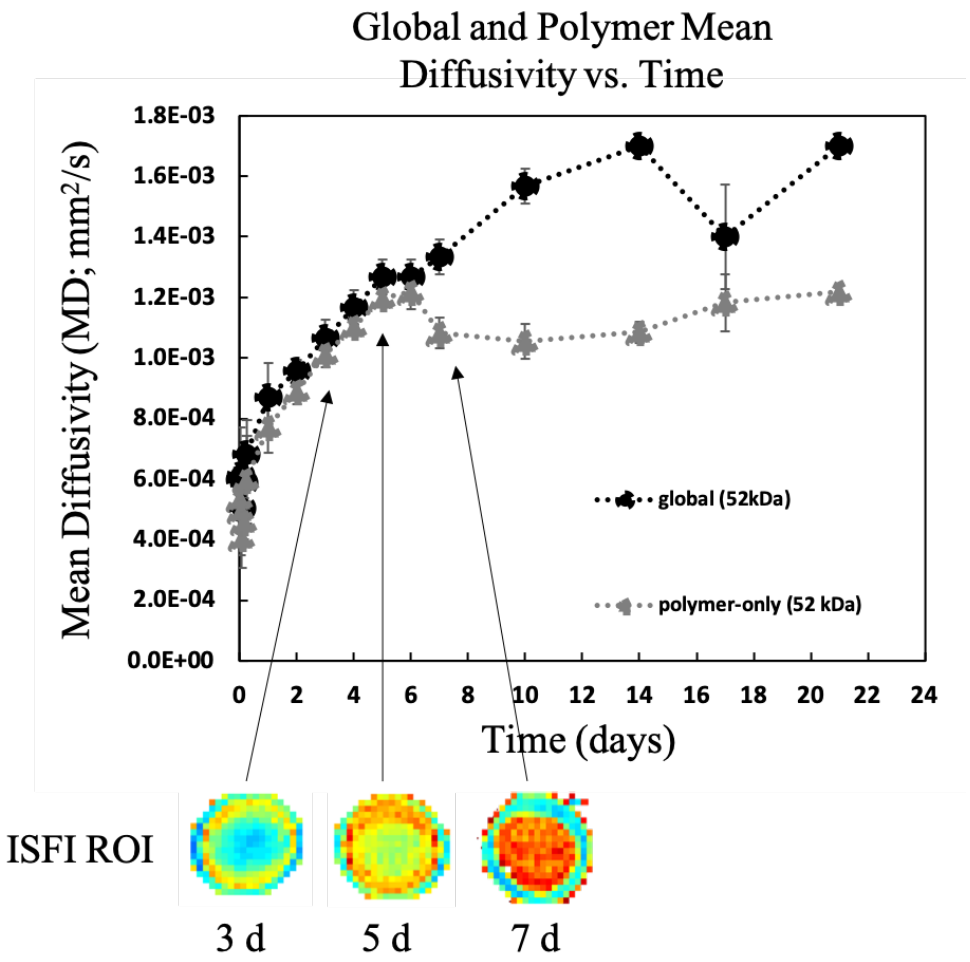

Fig. A.6. A comparison of global and polymer-only MD over time. At days 3 and 5, the MD is consistent betwen global and polymer-only analysis. At day 7, there is a divergence in MD between global and polymer-only analysis where MD is higher using the global analysis method.

From 0.25 hours to six days, global and polymer-only MD remained similar. However, by day seven, MD diverged and was higher for the the global analysis versus the polymer-only analysis. The polymer-only MD reflects ISFI regions that have low MD. As time increased, the the ISFI underwent degradation and the area with high MD increased; this is observed in the divergence in MD at day seven. At this point, the shell dominates the MD of the polymer-only region and therefore, MD remains

constant. However, the interior portion is degrading, more water enters the ISFI, and the global MD ultimately increases.

Second, shell diffusivity was compared with the interior diffusivity (Figure 5.7).

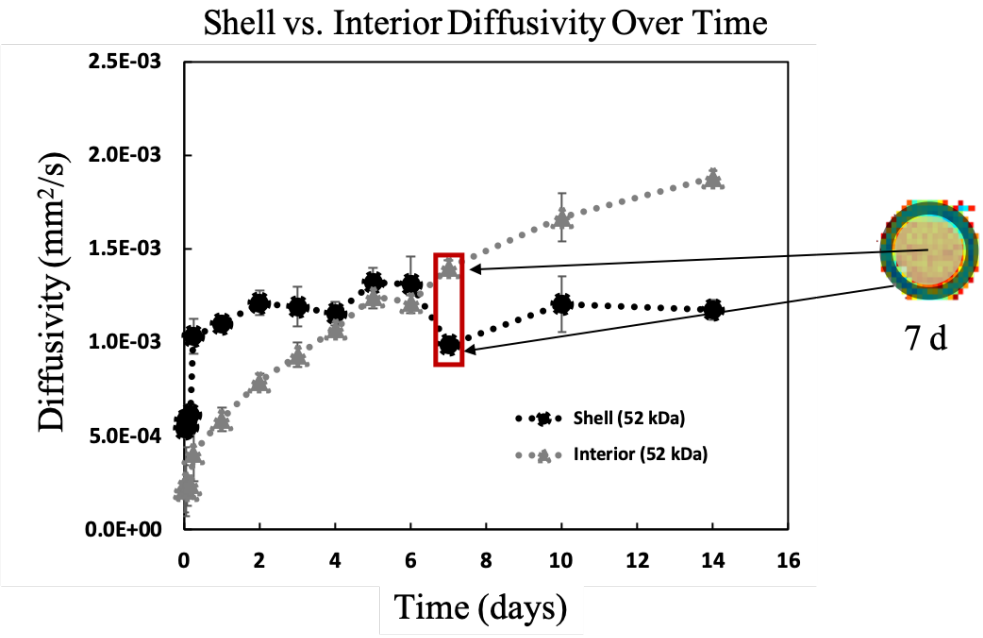

Fig. A.7. A comparison of shell and interior diffusivity over time. At day 7, the interior potion of the ISFI has a higher diffusivity versus the shell.

Here, the goal was to understand how the shell and interior portions of the ISFI change with respect to time. Initially, the shell had a phase of rapid diffusion which is indicative of the burst-release phase. After this phase, the shell maintained a steady rate of diffusivity over time, until the ISFI degraded. Contrary, the interior portion displayed a steady increase in diffusivity over time. This can be attributed to the constant exchange of drug with water and degradation of the polymer.

Thirdly, ISFIs was characterized using ring erosion. This analysis provided spatial profiles of ISFIs over time (Figure 5.8).

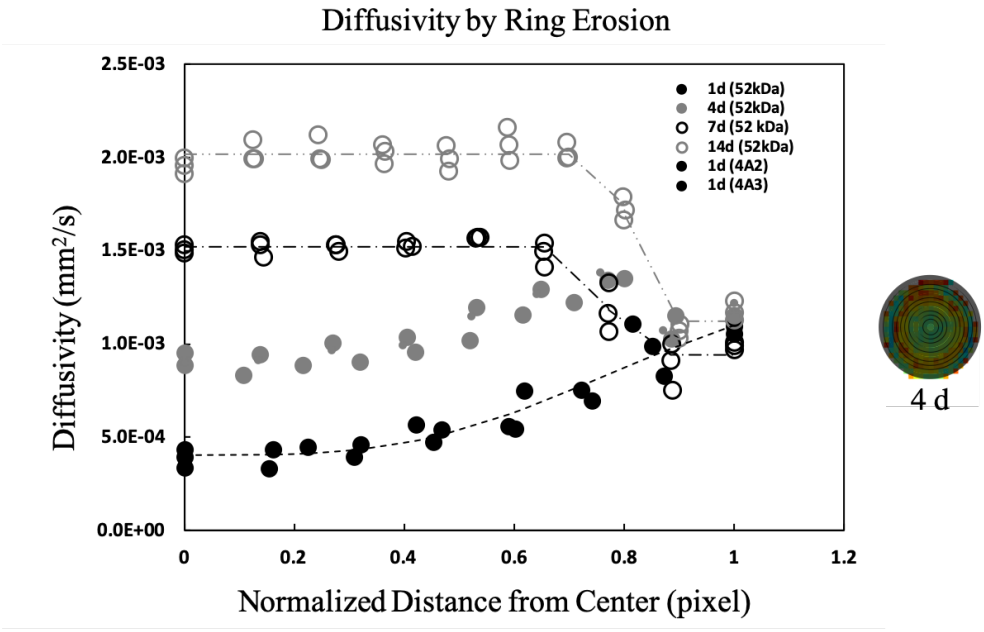

Fig. A.8. Spatial analysis of ISFIs using ring erosion. Each ring was one pixel in thickness and erosion was performed from the outside, inwards. The distance from the center to the exterior of the ISFI was normalized with the center equal to 0 and the last ring equal to 1.

In Vivo DWI and 4A ISFI Characterization

ADC maps from *in vivo* imaging were generated for each mouse; one representative image is depicted in Figure 5.9. The circled regions correspond the the ISFI ROI, located above the right and left flank. Due to tissue constraints and varying injection site, the depicted slices represent different portions of an ISFI. However, quantitative analysis was performed by averaging the MD of each slice. Over time, ADC in the ROI increased and by day 5, there were regions of high diffusion within the ISFI ROI. Although trigger was used, the observed noise is likely due to motion artifacts caused by breathing and heart beat.

MD was calculated for each slice and averaged across slices and compared with the MD calculated in phantom *ex vivo* (Figure 5.10) There were statistically significant differences between *in vivo* and *ex vivo* MD at six hours and three days. At three

hours, *ex vivo* MD was significantly higher than *in vivo* MD. At six days, *in vivo* MD was significantly higher than *ex vivo* MD. These results will be further explained in the discussion section.

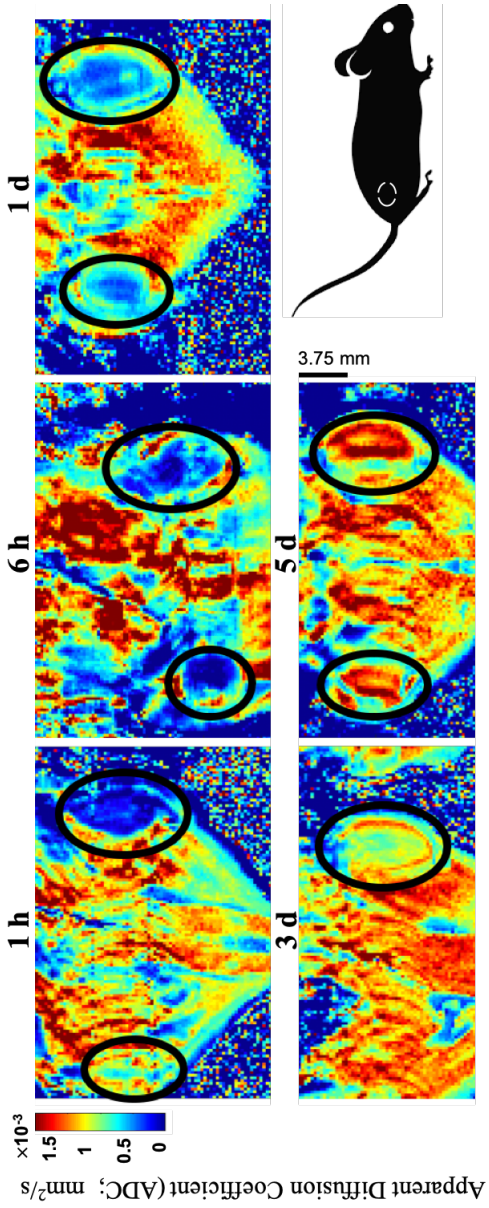

Fig. A.9. Representative ADC Maps of *in vivo* ISFIs. The circled regions represent the ISFI ROI above each flank.

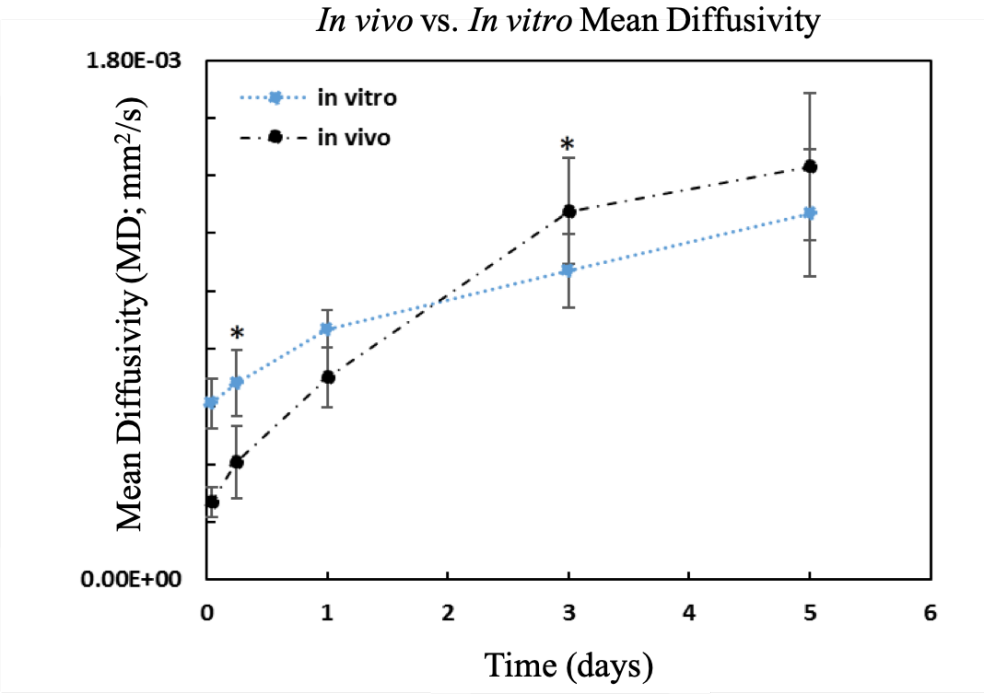

Fig. A.10. Graphical comparison of *in vivo* and phantom (*ex vivo*) MD. * represents statistically significant differences ($\alpha < 0.05$).

SEM and ADC Map Comparison

SEM images were collected to compare with ADC maps obtained from *in vivo* and *ex vivo* DWI. The high resolution of the SEM images allows for qualitative and quantitative analysis of the ISFI microstructure. Comparing these images with ADC maps could give insight into why ADC is higher, or lower, at specific times points. In addition, the microstructure of ISFIs *in vivo* and *ex vivo* can be examined (Figure 5.11). Immediately, it is evident that tissue environment had a drastic effect on the structure of the ISFIs. This is seen when comparing the *in vivo* and phantom SEM images. In phantom, the shell is nicely defined and there is a clear boundary between the shell and the interior structure. However, *in vivo*, this definition is not as clear. Specifically, it is interesting to note differences at day five. At this time point, MD

in vivo is higher than in phantom. Accordingly, the interior portion of the ISFI is markedly more porous when compared to the phantom (*ex vivo*) ISFI at day five.

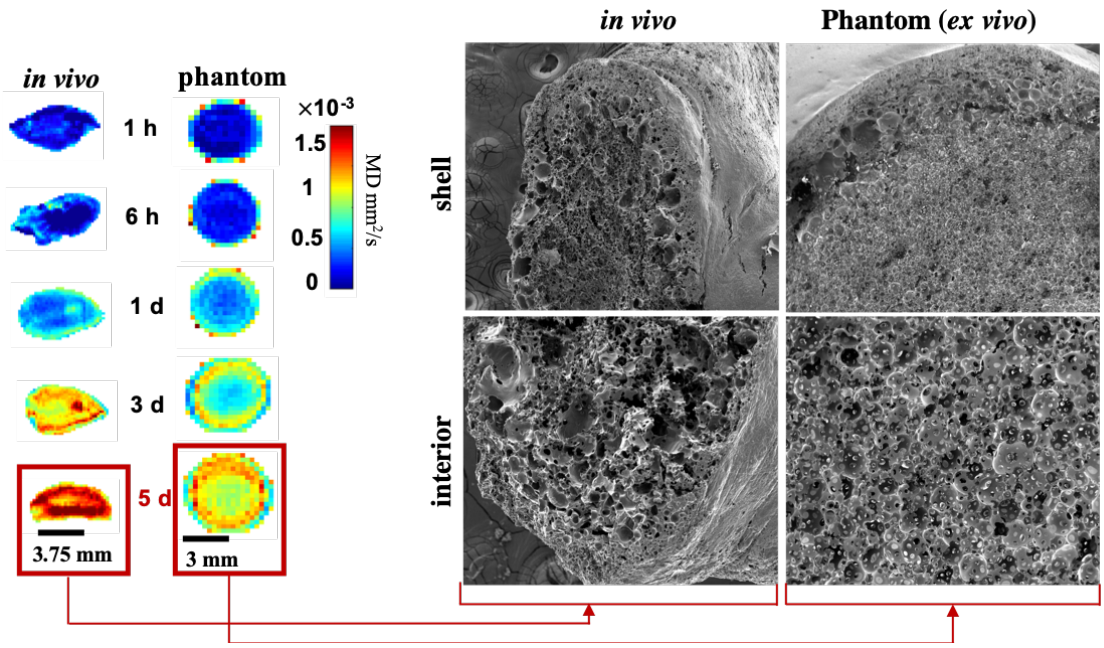

Fig. A.11. Comparison of ISFI microstructure with ADC maps *in vivo* and *ex vivo*.

A.1.4 Discussion

DWI is a noninvasive and sensitive technique shown to provide valuable insight into ISFI characteristics and diffusivity in phantom (*ex vivo* and *in vivo*). This method has potential applications in drug development and design, as well as pharmaceutical research, with the overarching goals of improving medication effectiveness, minimizing problems associated with medication adherence, and improving patient outcomes.

Work completed *in vitro* and *ex vivo* were critically important for the analysis and validation of *in vivo* data. In general, MD showed similar trends between *ex vivo* and *in vivo* analyses. This was evidenced in Figure 5.10 where the slopes of MD follow a similar trend over time. However, there were significant differences in

MD at three hours and six days. This can be attributed to 1) initial tissue-exerting pressures preventing diffusion out of ISFIs implanted *in vivo* at six hours, and 2) latter tissue-exerting pressures increasing the rate of diffusion out of *in vivo* ISFIs at day three. These observations become important in the design and engineering of ISFIs. For example, if faster initial release is desired, it may be more appropriate to use a polymer of higher molecular weight (i.e. 4A) as these polymers have been shown to release more drug than ISFIs composed of lower molecular weight polymers (Figure 5.4). The structure of the drug can also be altered so it is more, or less, easily exchanged with the aqueous environment. While this information is useful, additional analysis can be completed to provide further details on ISFI behavior.

Figures 5.6-5.8 offer novel ways to characterize ISFI diffusivity: 1) global vs. polymer-only MD, 2) shell vs. interior MD, and 3) spatial analysis using ring erosion. Analysis of ISFIs globally provides information regarding the overall behavior of the ISFI while polymer-only MD excludes regions that have undergone degradation. A comparison of these two metrics may offer insight into ISFI degradation rates. Shell MD quantification provides details on shell integrity - the higher the MD of the shell, the higher the rate of exchange. Interior MD quantification is important for the analysis of the ISFI region containing the drug and accumulated water. The higher the MD in this region, the more water has infiltrated. Finally, analysis of individual rings can be useful for detailed spatial analysis of the ISFI - that is, how is diffusion changing across the entire diameter of the ISFI. These plots can be generated to aid in ISFI design which will ultimately help to optimize drug release profiles.

A.2 Future Work

Future work must be completed analyzing these plots *in vivo*. While *in vivo* data was collected, poor image quality prevented the use of these sophisticated methods. Therefore, it is first necessary to improve the image quality. This could be accomplished using alternative DWI or DTI methods such as spiral or echo-planar

imaging. Additionally, care must be taken to eliminate noise that can result from motion artifacts. Lastly, *in vivo* work was conducted on a small sample size (n=6; 2 ISFIs/mouse). Larger sample sizes must be tested to prove significance and create robust *in vivo* ISFI characterization methods.

A.3 Conclusions

Overall, DWI is sensitive and noninvasive method which can be used to evaluate ISFI characteristics, including diffusivity, *in vivo* over time. This noninvasive investigation can improve the overall design of ISFIs, eventually leading to improved treatment efficacy and better patient outcomes.

B. SUPPLEMENTAL DATA FOR CHAPTERS THREE AND FOUR

High School Controls: DLPFC Metabolites

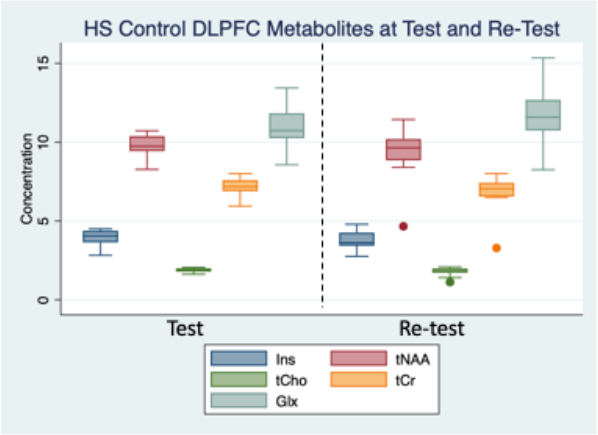

Metabolite	Session	Mean	Average of Mean
Ins	Test	3.92	3.83
Ins	Retest	3.74	
tNAA	Test	9.80	9.57
tNAA	Retest	9.34	
tCho	Test	1.87	1.83
tCho	Retest	1.80	
tCr	Test	7.12	6.98
tCr	Retest	6.86	
Glx	Test	11.01	11.30
Glx	Retest	11.60	

Fig. B.1. DLPFC metabolite data from high school controls at test and re-test imaging sessions (n = 14; mean age = 16.4). There were no significant differences in any metabolites between test and re-test (p-value >0.05).

High School Controls: M1 Metabolites

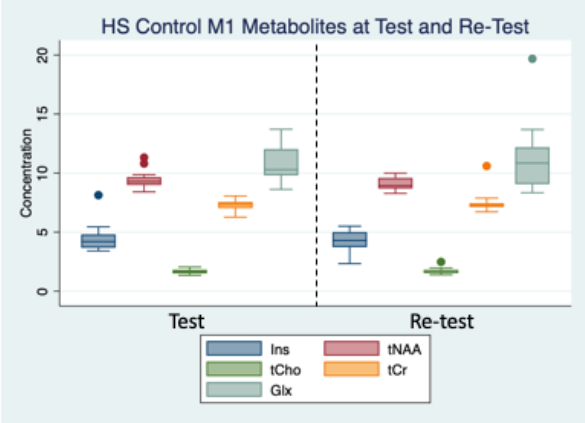

Metabolite	Session	Mean	Average of Mean
Ins	Test	4.47	4.37
Ins	Retest	4.27	
tNAA	Test	9.44	9.26
tNAA	Retest	9.08	
tCho	Test	1.68	1.70
tCho	Retest	1.73	
tCr	Test	7.29	7.39
tCr	Retest	7.50	
Glx	Test	10.80	11.07
Glx	Retest	11.33	

Fig. B.2. M1 metabolite data from high school controls at test and re-test imaging sessions (n = 14; mean age = 16.4). There were no significant differences in any metabolites between test and re-test (p-value >0.05).

Metabolite	ROI	HS, MS, C	Session	Mean	Median	Control Avg.	*P*-Value
Ins Ins	DLPFC DLPFC	C C	Test Retest	3.92 3.74		3.83	0.2322
Ins Ins	DLPFC DLPFC	MS HS	Pre Pre	4.72 5.30	4.63 4.92		0.2106
Ins Ins	DLPFC DLPFC	MS HS	Post Post	4.15 4.50	4.06 4.29		0.3357
tNAA tNAA	DLPFC DLPFC	C C	Test Retest	9.80 9.34		9.57	0.4907
tNAA tNAA	DLPFC DLPFC	MS HS	Pre Pre	9.34 10.92	9.49 10.59		**0.0019**
tNAA tNAA	DLPFC DLPFC	MS HS	Post Post	8.90 10.43	8.81 10.07		**0.0039**
tCho tCho	DLPFC DLPFC	C C	Test Retest	1.87 1.80		1.83	0.7828
tCho tCho	DLPFC DLPFC	MS HS	Pre Pre	1.92 2.14	1.94 2.13		**0.0175**
tCho tCho	DLPFC DLPFC	MS HS	Post Post	1.95 2.14	1.93 2.05		0.1112
tCr tCr	DLPFC DLPFC	C C	Test Retest	7.11 6.86		6.98	0.6459
tCr tCr	DLPFC DLPFC	MS HS	Pre Pre	7.41 8.14	7.22 7.95		**0.0323**
tCr tCr	DLPFC DLPFC	MS HS	Post Post	6.99 7.91	6.84 7.65		**0.0101**
Glx Glx	DLPFC DLPFC	C C	Test Retest	11.01 11.60		11.30	0.3827
Glx Glx	DLPFC DLPFC	MS HS	Pre Pre	13.24 13.37	13.14 12.67		0.6371
Glx Glx	DLPFC DLPFC	MS HS	Post Post	12.71 12.00	12.14 11.69		0.5635

Table B.1.
Table of DLPFC metabolite values in high school controls, high school athletes, and middle school athletes between test and re-test and *Pre* and *Post*. p-values underlined and bolded are significant (C = control; MS = middle school athlete, HS = high school athlete).

Metabolite	ROI	HS, MS, C	Session	Mean	Median	C Avg.	*P*-Value
Ins	M1	C	Test	4.47		4.37	0.7828
Ins	M1	C	Retest	4.27			
Ins	M1	MS	Pre	4.21	4.34		**0.0009**
Ins	M1	HS	Pre	5.72	5.66		
Ins	M1	MS	Post	3.92	3.87		**0.0023**
Ins	M1	HS	Post	4.69	4.55		
tNAA	M1	C	Test	9.44		9.26	0.3121
tNAA	M1	C	Retest	9.08			
tNAA	M1	MS	Pre	10.10	10.46		0.3237
tNAA	M1	HS	Pre	11.63	11.08		
tNAA	M1	MS	Post	9.06	9.19		0.1407
tNAA	M1	HS	Post	9.74	9.63		
tCho	M1	C	Test	1.68		1.70	1.000
tCho	M1	C	Retest	1.73			
tCho	M1	MS	Pre	1.73	1.73		**0.0308**
tCho	M1	HS	Pre	2.15	1.89		
tCho	M1	MS	Post	1.60	1.56		0.0738
tCho	M1	HS	Post	1.78	1.73		
tCr	M1	C	Test	7.29		7.39	0.9634
tCr	M1	C	Retest	7.50			
tCr	M1	MS	Pre	7.51	7.42		**0.0197**
tCr	M1	HS	Pre	9.16	8.43		
tCr	M1	MS	Post	7.18	7.14		**0.0075**
tCr	M1	HS	Post	7.84	7.55		
Glx	M1	C	Test	10.80		11.07	0.8183
Glx	M1	C	Retest	11.33			
Glx	M1	MS	Pre	10.73	11.26		0.1407
Glx	M1	HS	Pre	13.30	11.60		
Glx	M1	MS	Post	11.04	10.87		0.8976
Glx	M1	HS	Post	11.38	10.72		

Table B.2.

Table of M1 metabolite values in high school controls, high school athletes, and middle school athletes between test and re-test and *Pre* and *Post*. p-values underlined and bolded are significant (C = control; MS = middle school athlete, HS = high school athlete).

HS Metabolite Changes

ROI	Metabolite	Session	Mean	Std. Dev.	Median	25th %	75th %
DLPFC	Ins	Pre	5.409188	1.392114	4.95114	4.36536	6.18346
DLPFC	Ins	In1	4.757246	1.002898	**4.63067**	4.0696	5.47888
DLPFC	Ins	In2	4.654992	1.083257	**4.25451**	3.94978	5.47888
DLPFC	Ins	Post	4.494959	1.151126	**4.2872**	3.81632	4.83954
M1	Ins	Pre	5.650041	1.31913	5.62733	4.69194	6.48345
M1	Ins	In1	4.494097	0.997905	**4.6221**	3.86697	4.99289
M1	Ins	In2	4.44335	0.703919	**4.40668**	3.99435	4.83883
M1	Ins	Post	4.693453	0.993724	**4.53578**	4.13679	5.05662
M1	tCho	Pre	2.074689	0.567141	1.89199	1.7273	2.28966
M1	tCho	In1	1.667798	0.183872	**1.61443**	1.53353	1.83515
M1	tCho	In2	1.706437	0.202436	**1.66512**	1.58509	1.861
M1	tCho	Post	1.775887	0.314643	**1.7311**	1.61282	2.13716
M1	tCr	Pre	8.892548	2.137152	8.42637	7.49482	10.238
M1	tCr	In1	7.502355	0.881046	**7.22748**	6.82841	8.24799
M1	tCr	In2	7.40636	0.850413	**7.31352**	6.89723	7.84469
M1	tCr	Post	7.844264	0.866343	**7.55004**	7.38904	8.47692
M1	Glx	Pre	12.64643	3.669666	11.596	10.36	14.28
M1	Glx	In1	10.5658	2.220065	**10.5381**	9.00069	12.2073
M1	Glx	In2	10.01794	2.228213	**10.3384**	8.75873	11.1737
M1	Glx	Post	11.37994	3.094796	10.72	9.19757	12.2751

Table B.3.
Table of high school metabolite values at *Pre*, *In1*, *In2*, and *Post*. Bolded values are significantly different from *Pre* (p-value <0.05). Blue indicates DLPFC metabolites and orange indicates M1 metabolites.

MS Metabolite Changes

ROI	Metabolite	Session	Mean	Std. Dev.	Median	25%	75%
DLPFC	Ins	Pre	4.715597	0.795776	4.625825	4.087093	5.256219
DLPFC	Ins	Post	**4.154129**	0.7294882	4.059535	3.70135	4.58674
DLPFC	tNAA	Pre	9.340377	0.81729	9.486675	8.768084	9.878181
DLPFC	tNAA	Post	8.897746	0.88601	8.809239	8.608527	9.439509
DLPFC	tCho	Pre	1.923851	0.326305	1.939672	1.783395	2.002284
DLPFC	tCho	Post	1.948958	0.187909	1.92695	1.877914	2.045026
DLPFC	tCr	Pre	7.413131	0.8579336	7.222601	6.843786	7.773348
DLPFC	tCr	Post	**6.989371**	0.7881706	6.838838	6.393833	7.409105
DLPFC	Glx	Pre	13.23593	2.077253	13.14285	11.58905	14.10748
DLPFC	Glx	Post	12.71	2.893485	12.14309	10.51004	14.29785
M1	Ins	Pre	4.210697	0.5815241	4.32687	3.70236	4.41277
M1	Ins	Post	3.916433	0.3661205	3.86782	3.63202	4.18021
M1	tNAA	Pre	10.09906	1.14534	10.54524	9.30072	11.1282
M1	tNAA	Post	**9.062865**	0.9232414	9.187923	8.29514	9.786018
M1	tCho	Pre	1.728129	0.1980862	1.729088	1.550997	1.90523
M1	tCho	Post	**1.596066**	0.1960648	1.556306	1.5143	1.75329
M1	tCr	Pre	7.508852	0.4315261	7.42197	7.19123	7.82644
M1	tCr	Post	7.181242	0.5572375	7.137148	6.93966	7.43591
M1	Glx	Pre	10.72573	2.30595	11.2616	8.78801	12.5871
M1	Glx	Post	11.04125	1.758177	10.8692	9.69389	13.2665

Table B.4.
Table of middle school metabolite values at *Pre* and *Post*. Bolded values are significantly different from *Pre* (p-value <0.05). Blue indicates DLPFC metabolites and orange indicates M1 metabolites.

ΔHS Metabolite Changes

Session-Session

ROI	Metabolite	Session-Session	ΔMedian
	Ins	**Normal Range (4-8 mM)**	
DLPFC	Ins	*Pre-In1* *Pre-In2* *Pre-Post*	0.3204 0.6966 0.6639
M1	Ins	*Pre-In1* *Pre-In2* *Pre-Post*	1.0052 1.2207 1.0916
	tCho	**Normal Range (~2 mM)**	
M1	tCho	*Pre-In1* *Pre-In2* *Pre-Post*	0.2776 0.2269 0.1609
	tCr	**Normal Range (6-12 mM)**	
M1	tCr	*Pre-In1* *Pre-In2* *Pre-Post*	1.1989 1.1129 0.8763
	Glx	**Normal Range (~12 mM)**	
M1	Glx	*Pre-In1* *Pre-In2*	1.0579 1.2576

Table B.5.
Summary of the absolute differences in high school metabolite values from *Pre* to *In1*, *In2*, and *Post*. Normal brain metabolite ranges are also listed. Only significant results are reported.

ΔMS Metabolite Changes

Session-Session

ROI	Metabolite	Session-Session	ΔMean
	Ins	**Normal Range (4-8 mM)**	
DLPFC	Ins	*Pre-Post*	0.5615
	tCr	**Normal Range (6-12 mM)**	
DLPFC	tCr*	*Pre-Post*	0.4238
	tNAA	**Normal Range (6-12 mM)**	
M1	tNAA	*Pre-Post*	1.0362
	tCho	**Normal Range (~2 mM)**	
M1	tCho*	*Pre-Post*	0.1321

*only significant in linemen
** only significant in non-linemen

Table B.6.
Summary of the absolute differences in middle school metabolite values from *Pre* to *Post*. Normal brain metabolite ranges are also listed. Only significant results are reported.

ROI	Metabolite	Session	Position	Mean	Std Dev.	Median	25th %	75th %
DLPFC	Ins	Pre	2	5.55508	1.567026	5.3855	4.23509	6.34932
DLPFC	Ins	In1	2	4.678893	1.162358	4.33771	3.78221	5.80953
DLPFC	Ins	In2	2	4.558575	0.9209772	**4.24605**	3.94978	5.06099
DLPFC	Ins	Post	2	4.228942	0.9382506	**4.1455**	3.51953	4.61135
M1	Ins	Pre	1	5.413132	1.167217	5.65728	4.691942	6.376378
M1	Ins	In1	1	4.890626	1.014401	4.745363	3.909886	5.955036
M1	Ins	In2	1	4.282219	0.5313931	**4.17035**	3.991717	4.82883
M1	Ins	Post	1	4.44666	0.6094518	**4.369**	4.136793	5.056616
M1	Ins	Pre	2	5.780341	1.407166	5.592917	4.782319	6.67378
M1	Ins	In1	2	4.286391	0.9472213	**4.438123**	3.719934	4.865406
M1	Ins	In2	2	4.527987	0.7778417	**4.46434**	4.084628	4.900596
M1	Ins	Post	2	4.829189	1.144135	**4.55561**	4.127391	5.091207
M1	tCho	Pre	1	2.021613	0.323391	1.939	1.890051	2.134
M1	tCho	In1	1	1.737973	0.1412902	**1.711638**	1.617892	1.86341
M1	tCho	In2	1	1.69217	0.193882	**1.633181**	1.570128	1.858583
M1	tCho	Post	1	1.669167	0.2066734	**1.67057**	1.488797	1.79434
M1	tCho	Pre	2	2.103881	0.6710408	1.824309	1.705445	2.315111
M1	tCho	In1	2	1.63104	0.1956946	**1.579101**	1.525858	1.693274
M1	tCho	In2	2	1.71391	0.2110776	**1.676036**	1.603818	1.900062
M1	tCho	Post	2	1.834582	0.351589	1.737879	1.670353	1.981171
M1	tCr	Pre	1	8.64041	1.385011	8.744453	7.2000	9.398466
M1	tCr	In1	1	7.637344	0.177466	7.647	6.678411	8.24862
M1	tCr	In2	1	7.297673	0.707363	7.247586	6.686359	7.84295
M1	tCr	Post	1	7.423755	0.4772155	7.475	7.3125	7.742024
M1	tCr	Pre	2	9.170724	2.469223	8.313008	7.610909	10.49433
M1	tCr	In1	2	7.431647	0.7033423	**7.111369**	6.848337	8.247356
M1	tCr	In2	2	7.463292	0.9278368	**7.327103**	6.648297	7.84643
M1	tCr	Post	2	8.075544	0.9521227	7.639191	7.456576	7.639191
M1	Glx	Pre	2	12.80307	4.291344	11.60581	10.17658	13.81945
M1	Glx	In1	2	10.66313	2.031113	10.42309	9.511988	12.16507
M1	Glx	In2	2	10.13746	2.352413	**10.24048**	8.800186	11.1589
M1	Glx	Post	2	11.99482	3.616695	11.09341	9.673265	12.7002

Table B.7.

Position-specific metabolite values in high school athletes at *Pre*, *In1*, *In2*, and *Post*. Bolded results represent significant differences at each respective session compared to *Pre* (p-value <0.05). Blue represents DLPFC metabolites and orange represents M1 metabolites.

MS DLPFC Metabolites Position-wise

ROI	Metabolite	Session	Position	Mean	Median	Std. Dev.	25th %	75th %
DLPFC	Ins	Pre	1	**4.816795**	4.626719	0.9187309	4.624931	5.031802
DLPFC	Ins	Post	1	**3.941148**	4.006243	0.2805282	3.98391	4.02603
DLPFC	Ins	Pre	2	4.643312	4.610756	0.7639598	3.768289	5.480636
DLPFC	Ins	Post	2	4.306258	4.196859	0.9264711	3.496359	4.980591
DLPFC	tNAA	Pre	1	8.790998	9.019785	0.710936	8.516382	9.348695
DLPFC	tNAA	Post	1	8.882169	8.710139	0.4070912	8.643179	8.908339
DLPFC	tNAA	Pre	2	9.732791	9.847641	0.685431	9.58625	10.06588
DLPFC	tNAA	Post	2	9.063159	9.043311	1.145769	8.130657	10.3438
DLPFC	tCho	Pre	1	1.862911	1.910353	0.1484616	1.767932	1.968991
DLPFC	tCho	Post	1	1.908211	1.900072	0.0987616	1.855756	1.907418
DLPFC	tCho	Pre	2	1.972523	1.972914	0.417935	1.798858	2.126088
DLPFC	tCho	Post	2	1.978063	1.994889	0.2363475	1.924642	2.062182
DLPFC	tCr	Pre	1	**7.503393**	7.173173	1.077687	7.038072	7.272028
DLPFC	tCr	Post	1	**6.509335**	6.521657	0.3440689	6.26601	6.755641
DLPFC	tCr	Pre	2	7.348658	7.277396	0.7506753	6.613954	8.171606
DLPFC	tCr	Post	2	7.332254	7.262193	0.8548541	6.710723	7.872287
DLPFC	Glx	Pre	1	13.93824	13.8896	2.239399	12.23585	14.32537
DLPFC	Glx	Post	1	11.96942	12.10002	1.850167	11.11907	12.18615
DLPFC	Glx	Pre	2	12.73427	12.91849	1.965422	11.36364	13.4301
DLPFC	Glx	Post	2	13.23899	12.85138	3.504788	10.50474	15.90297

Table B.8.
Position-specific DLPFC metabolite values in middle school athletes at *Pre* and *Post*. Bolded results represent significant differences at *Post* compared to *Pre* (p-value <0.05).

MS M1 Metabolites Position-wise

ROI	Metabolite	Session	Position	Mean	Median	Std. Dev.	25th %	75th %
M1	Ins	Pre	1	4.020487	4.09556	0.5023111	3.70236	4.15123
M1	Ins	Post	1	3.923188	3.98169	0.4314089	3.63202	4.15123
M1	Ins	Pre	2	4.369206	4.425068	0.6388721	4.32687	4.71277
M1	Ins	Post	2	4.180545	4.25354	0.536157	3.75436	4.544653
M1	tNAA	Pre	1	9.54447	9.30072	1.439234	8.392429	10.9292
M1	tNAA	Post	1	9.183382	9.100837	1.152076	8.29514	9.78391
M1	tNAA	Pre	2	**10.56121**	10.59347	0.6345248	10.12167	11.1863
M1	tNAA	Post	2	**9.912276**	10.01822	1.074653	9.589825	10.59347
M1	tCho	Pre	1	1.561543	1.550997	0.12197	1.54949	1.64548
M1	tCho	Post	1	1.578462	1.550243	0.1396025	1.5143	1.64548
M1	tCho	Pre	2	**1.866951**	1.86737	0.1252926	1.72973	1.99453
M1	tCho	Post	2	**1.731794**	1.74103	0.2274521	1.607643	1.89379
M1	tCr	Pre	1	7.485419	7.42197	0.4118981	7.29061	7.82644
M1	tCr	Post	1	7.367389	7.334382	0.3961997	6.93966	7.80508
M1	tCr	Pre	2	7.528379	7.466457	0.4854841	7.19123	7.76306
M1	tCr	Post	2	7.326429	7.25017	0.6131638	7.026667	7.693432
M1	Glx	Pre	1	10.73759	11.2616	1.783419	9.09726	12.11278
M1	Glx	Post	1	10.44621	10.82268	1.43979	9.09726	11.2616
M1	Glx	Pre	2	10.71584	11.2542	2.844308	8.78801	12.5914
M1	Glx	Post	2	11.24789	11.3652	2.383102	9.718357	13.31595

Table B.9.
Position-specific M1 metabolite values in middle school athletes at *Pre* and *Post*. Bolded results represent significant differences at *Post* compared to *Pre* (p-value <0.05).

High School HAEs

HAE Variable	Position	Mean	Std. Dev.	95% CI
tHits	1	487.75	309.2706	343.0069, 632.4931
cPLA	1	17443.13	11494.07	12063.74, 22822.52
aPLA	1	35.34217	3.626266	33.64503, 37.03932
tHits > 50g	1	68.45	61.11807	39.84586, 97.05414
cPLA > 50g	1	4681.725	4240.979	2696.971, 6666.479
aPLA > 50g	1	68.31327	4.947406	65.99781, 70.62873
tHits	2	210.8286	112.3643	168.795, 252.8622
cPLA	2	8026.102	4706.404	6409.396, 9642.809
aPLA	2	37.62096	4.549384	36.0582, 39.18373
tHits > 50g	2	38.17143	25.46796	29.42288, 46.91998
cPLA > 50g	2	2790.495	1932.681	2126.596, 3454.394
aPLA > 50g	2	73.30924	8.803526	70.28512, 76.3336

Table B.10.
Summary table of high school head acceleration events by position.

VITA

Nicole Vike received her B.Sc. in Neurobiology with a certificate in Global Health from the University of Wisconsin-Madison in 2014. In 2015, Nicole enrolled in Purdue University's Interdisciplinary Life Sciences Ph.D. Program (PULSe) where she worked under Dr. Thomas Talavage and coordinated the Purdue Neurotrauma Group studies. She also worked collaboratively with Dr. Joseph Rispoli and Dr. Riyi Shi on other magnetic resonance imaging-related research projects. Nicole's primary interests include 1) using magnetic resonance spectroscopy to investigate neurometabolic changes in collision-sport athletes, 2) player position-specific effects on neurometabolic changes in these athletes, 3) investigation of novel TBI biomarkers, and 4) applications of diffusion-weighted imaging to characterize *in situ* forming implants.

During her first year, Nicole received the Lynn Fellowship for graduate students in interdisciplinary fields. In summer 2018, she was a summer research grant recipient through the College of Veterinary Medicine. She was also awarded travel awards from the Purdue Graduate Student Government, the International Society for Magnetic Resonance in Medicine (ISMRM), the Purdue Institute for Integrative Neuroscience, and the Women in Science Program. In addition, Nicole was awarded first and second place at the Indiana Neuroimaging Symposium and the Health and Disease Research Symposium, respectively. She also received honorable mention for the Most Outstanding Interdisciplinary Graduate Project at Purdue. Notably, she was invited for oral presentations at ISMRM 2018 and the ISMRM Ultra High-Field Workshop.

She was also very active in leadership and founded three different organizations at Purdue: 1) The Purdue University Chapter for the Society of Applied Spectroscopy,

2) the Purdue Association for Magnetic Resonance, and 3) the Advanced Degree Consulting Club at Purdue.